博士論文

Magneto-transport properties of skyrmions and chiral spin structures in MnSi

(MnSi におけるスキルミオンおよび

カイラルスピン構造の磁気輸送特性)

横内智行

Contents

Chapter 1

Introduction

1.1 Preface

If an object cannot be superposed on its mirror image by any sequence of rotation and translation, the object is chiral. The concept of chirality was first introduced in the 19th century and is a central and unifying concept in modern science [1]. In condensed matter, chiral structure is found not only in molecular structures and crystal structures but also in spin structures; chiral crystals can transmit their chirality to the magnetism via antisymmetric exchange interaction of relativistic origin, producing chiral spin structures such as a helical structure [Fig. 1.1]. For example, chiral spin structures play an important role in magnetoelectric (ME) effect, namely the mutual coupling between magnetism and electricity [2].

Recently chiral spin structures also attract intensive interest because some chiral spin structures are topologically nontrivial. Topology is one of the most important concepts in contemporary physics, characterizing the quantum Hall states, the topological insulators, and the topological superconductors, for instance [3]. In spin systems, spin structures with nontrivial topology give rise to a host of novel phenomena, furthermore offering advantage for the potential spintronics applications. One such example is a magnetic skyrmion, which has been

discovered in a chiral magnet of MnSi in 2009 [Fig. 1.1(a)]. Topological nature of skyrmion brings about various unique transport phenomena; conduction electrons passing through skyrmions acquire the real-space Berry phase, which leads to topological Hall effect [4]. In addition, the conduction electrons drive skyrmions through spin transfer torque by ultra low current density, and hence various applications of skyrmions such as skymion-based non-volatile memory devices have been proposed [4, 5].

In this Thesis, we have explored novel transport phenomena in which both chiral and topological properties of skyrmion and chiral spin structures play crucial roles. Below, we will introduce skyrmions and chiral spin structures and their transport properties.
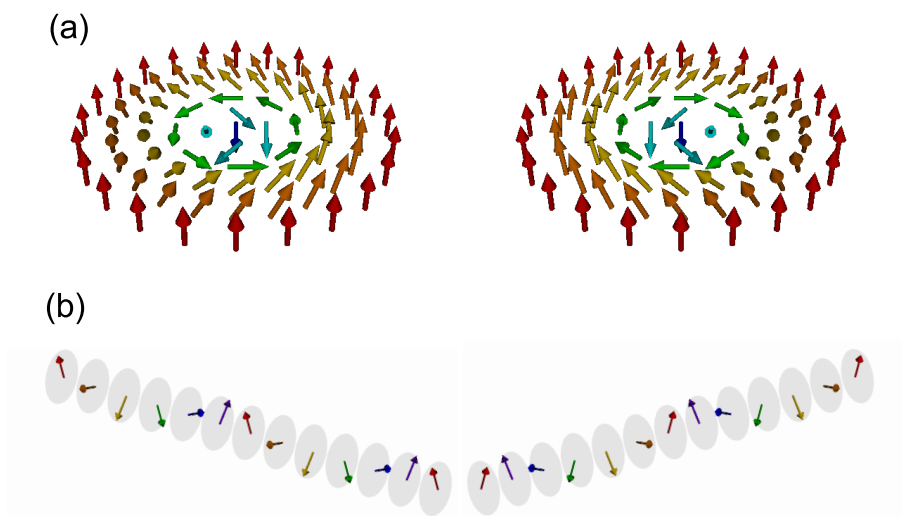
Figure 1.1: Spin structures of left- and right-handed skyrmions (a) and left- and right-handed helical orders (b).

1.2 Skyrmions and chiral spin structures

1.2.1 Skyrmions and helical structures

Basic aspects of skyrmion

Skyrmion is characterized by the nonzero topological number (skyrmion number) N_{Sk} as defined by

$$N_{\mathrm{Sk}} = \frac{1}{4\pi} \int d\boldsymbol{r}\, \boldsymbol{n} \cdot \left(\frac{\partial \boldsymbol{n}}{\partial x} \times \frac{\partial \boldsymbol{n}}{\partial y} \right), \qquad (1.1)$$

where $\boldsymbol{n} = \boldsymbol{n}/|\boldsymbol{m}|$ is an unit vector parallel to the local moment $\boldsymbol{m}$ [4]. This topological nature guarantees stability of skyrmion; skyrmion cannot continuously transform to other competing spin structures such as conical or ferrmagnetic states (i.e. topological stability). As mentioned in the next section, the topology of skyrmion also gives rise to unique transport phenomena.
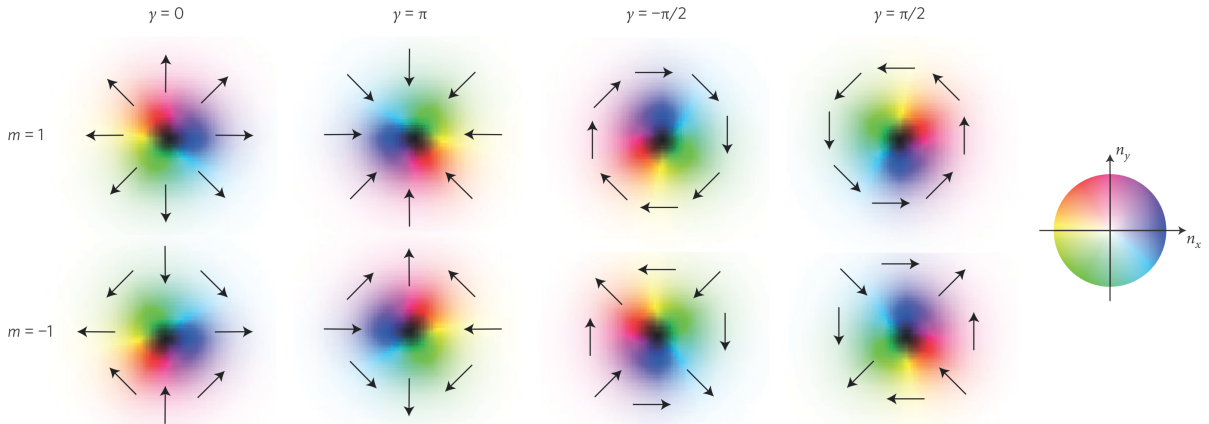
Figure 1.2: skyrmion structures with various vorticity m and helicity h. Reproduced from Ref. [4].

As shown in Fig. 1.2, there exist several types of skyrmion, which are characterized by helicity h and vorticity m, depending on the dominant mechanisms of the stabilization of skyrmion [4]. So far, four mechanisms of the stabiliza-

Magnetic phase diagram in chiral magnets hosting skyrmion share the common characteristics as shown in Fig. 1.4, which originate from three hierarchical energy scales: (1) exchange interaction (J) on the strongest scale, (2) DM interaction (D) on the intermediate scale, and (3) the weakest cubic anisotropy (K) [7]. The ground state is a helical state with a single wavevector $\boldsymbol{q}$, whose magnitude is $Q = D/J$ and the direction is determined by the cubic anisotropy. With increasing magnetic field, the helical state transforms to the conical state, in which $\boldsymbol{q}$ parallel to the magnetic field direction followed by the induced ferromagnetic state. Skyrmion form a triangular lattice (SkL) in a narrow temperature-magnetic field region just below T_c [7, 14, 15, 16] [Fig. 1.4]. The triangular lattice of skyrmion can be described by a superposition of three helical states [4, 7];

$$\boldsymbol{n} = \boldsymbol{n}_\mathrm{uniform} + A \sum_{i=1}^{3} \left[\boldsymbol{n}_{i1} \cos(\boldsymbol{Q}_i \cdot \boldsymbol{r}) + \boldsymbol{n}_{i2} \sin(\boldsymbol{Q}_i \cdot \boldsymbol{r}) \right]. \tag{1.2}$$

Here, $\boldsymbol{n}_\mathrm{uniform}$ and A are uniform magnetization induced by the external magnetic field and the magnetization of a single helix, respectively. The Q-vectors are perpendicular to magnetic field, satisfied the relation $\boldsymbol{Q}_1 + \boldsymbol{Q}_2 + \boldsymbol{Q}_3 = 0$, and $\boldsymbol{n}_{i1}$, $\boldsymbol{n}_{i2}$, and $\boldsymbol{Q}_i$ are orthogonal to each other.

Observation of skyrmions in chiral magnets

Experimentally, SkL was first observed in $B20$-type MnSi by using small angle neutron scattering (SANS)[7]. Figure 1.5 shows the experimental setup and SANS pattern with magnetic field parallel to the incident neutron beam. As shown in Fig. 1.5(b), the SANS pattern shows six fold spots, indicating formation of a triangular lattice of skyrmions.

Subsequently, the real-space observation of skyrmion lattice using Lorentz transmission microscopy (TEM) was reported in a thin plate sample of $B20$-type $Fe_{0.5}Co_{0.5}Si$, whose thickness is approximately 20 nm [Fig 1.6(a)][8]. In addition to the triangular lattice of skyrmions [Fig 1.6(a) and (c)], isolated skyrmions in the helical/ferrromagnetic background are also observed [Fig 1.6(b) and (d)],
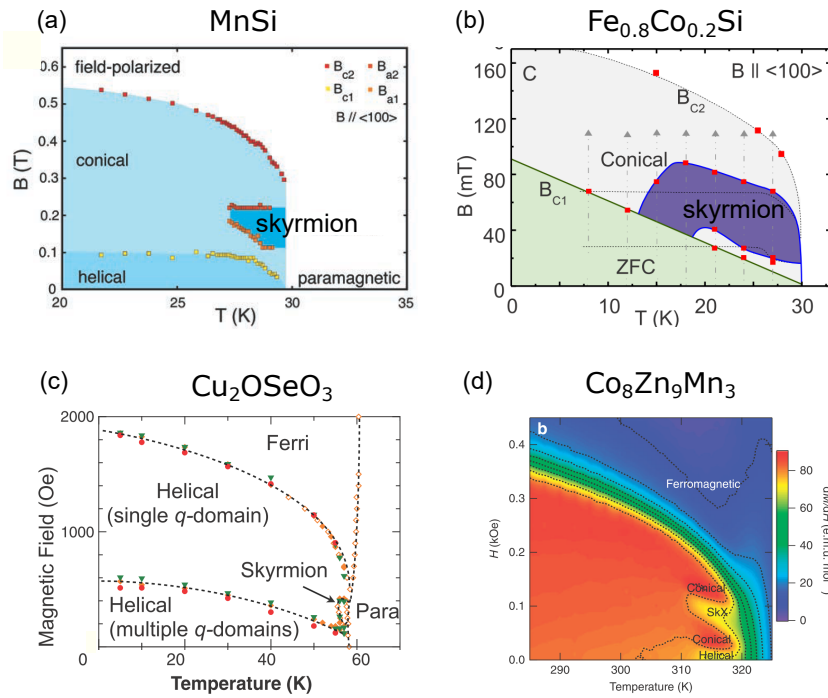
Figure 1.4: Magnetic phase diagrams of MnSi (a), $Fe_{0.8}Co_{0.2}Si$ (b), Cu_2OSeO_3 (c), and $Co_8Zn_9Mn_3$ (d). Reproduced from Ref. [7, 14, 15, 16].
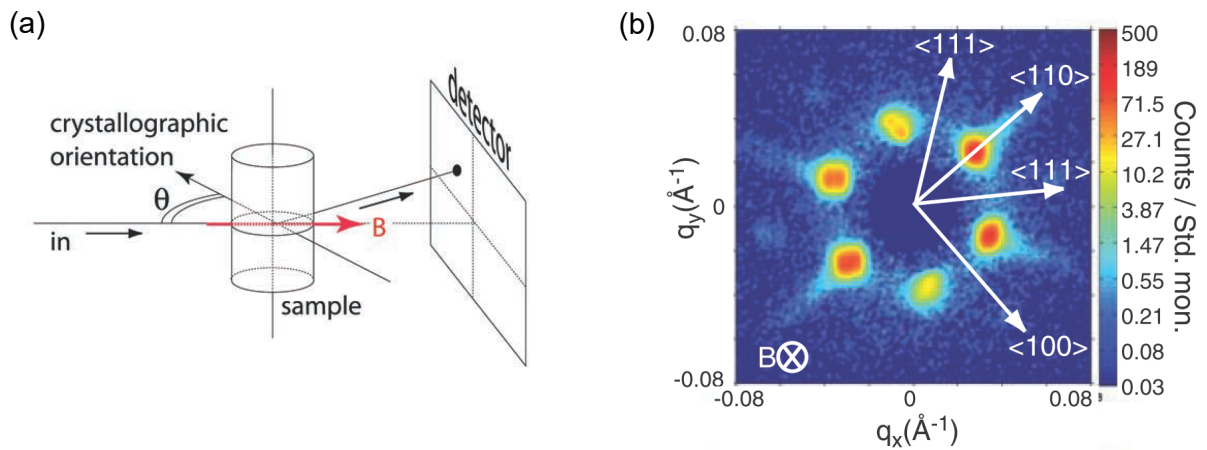
Figure 1.5: (a) Experimental setup for the small angle neutron scattering (SANS) on MnSi. (b) Sixfold SANS pattern in skyrmion phase. Reproduced from Ref. [7].

highlighting the particle nature of skyrmions. Whereas in bulk samples SkL is stabilized only in a narrow temperature-magnetic field region, skyrmions stabilized wide temperature-magnetic field region in the case of thin plate samples [Fig 1.6(e)]. Thickness (t) dependence of skyrmion phase region has been quantitatively studied in a wedgewise thinned plate of $B20$-type FeGe [17]. The temperature range of the skyrmion phase as observed by LTEM extends from T_c of 280 K to 50 K in a thin part ($t \approx 15$ nm), while it tends to shrink toward a small window just below T_c in thicker parts ($t \approx 75$ nm). The above observation indicates that the typical t value for the crossover of stability between skyrmion and conical state is around the helical period ($\lambda = 70$ nm). This is perhaps because the spins cannot form even one cycle of spiral in the case of $t \leq \lambda$, which leads to destabilization of the conical state over the skyrmion state.
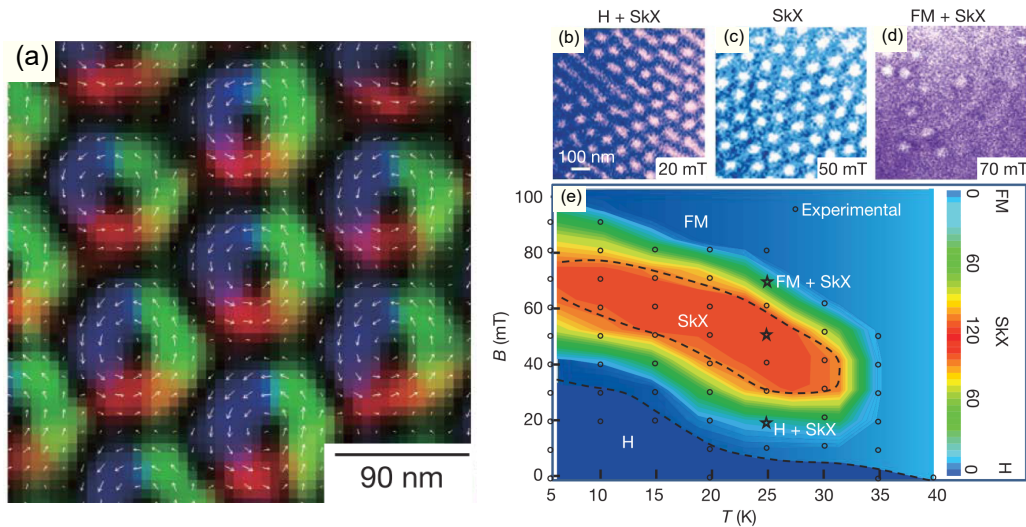
Figure 1.6: (a) Real-space observation of spin structure of skyrmions by Lorentz transmission electron microscopy (Lorentz TEM) in a thin plate $Fe_{0.5}Co_{0.5}Si$. (b)-(d) Lorentz TEM images at various magnetic field (20 mT, 50 mT, and 70 mT) (e) Phase diagram of the thin plate of $Fe_{0.5}Co_{0.5}Si$. Reproduced from Ref. [8].
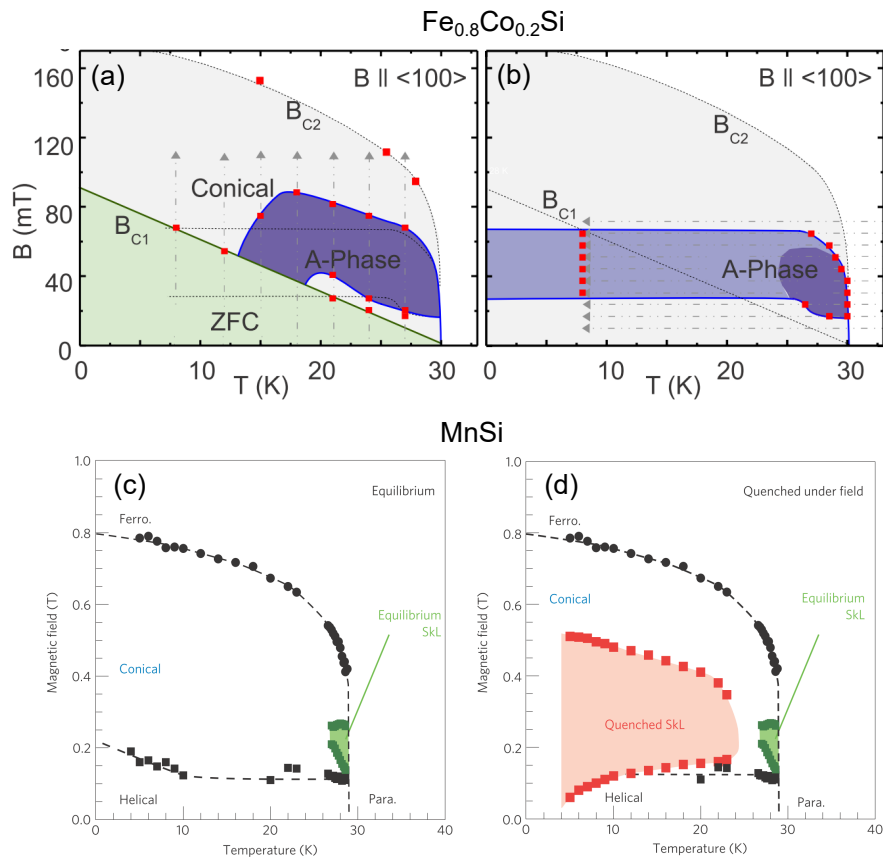
Figure 1.7: Magnetic phase diagrams of $Fe_{0.8}Co_{0.2}Si$ under thermodynamic equilibrium (a) and including the metastable skyrmion lattice crated by field cooling (FC) (b). Magnetic phase diagrams of MnSi under thermodynamic equilibrium (c) and including the metastable skyrmion lattice crated by created FC (d). Reproduced from Ref. [14, 19].

Metastability of skyrmions

Because of difference in topology between the skyrmion and the conical/helical structures, the transition between two states are first-order transition. Hence, even in bulk samples, skyrmion can exist at low temperatures as a metastable state, although an equilibrium skyrmion sate appears at a narrow temperature region just below T_c [14, 18, 19, 20]. Figure 1.7(a) is the equilibrium magnetic phase diagram of $Fe_{0.8}Co_{0.2}Si$. Skyrmion phase appears at a narrow temperature region. In contrast, in the case of a field cooling procedure passing thought the equilibrium skyrmion sate, the skyrmion exists down to the lowest temperature. [Fig 1.7(b)] [14]. Similar phase diagrams are also reported in MnSi as shown in Fig 1.7(c) and (d)[19]. Here, we note the effect of a cooling rate on the formation of a metastable skyrmion state. In general, when the cooling rate is slow enough compared with the phase-transition kinetics, the phase transition to a thermodynamically stable state occurs. In contrast, when the cooling rate exceeds the phase-transition kinetics, the phase transition is avoided and a metastable state appears. In the case of skyrmions, metastable skyrmions appear with the standard cooling rate (typically, 2×10^{-3} to 4×10^{-1} K/s) when randomly positioned atoms or pressure inhomogeneities are introduced [14, 18, 20]. In contrast, in nominally pure samples such as MnSi, metastable skymion appears only when the rapid cooling rate is performed (typically, 700 K/s) [19].

Metastable skyrmions often show the structural transition from a triangular lattice to a square lattice. In Fig 1.8, we show SANS patters of metastable triangular lattices and square lattices of skyrmions and magnetic phase diagrams in $Co_8Zn_8Mn_4$ [Fig. 1.8(a)] and MnSi [Fig. 1.8(b)] [20, 21]. In both materials, square lattices of skyrmions appear at low temperatures. This is perhaps because magnetic anisotropy from the chemical lattice, which is relatively strong at low temperatures, triggers the structural transition of skyrmion lattice.
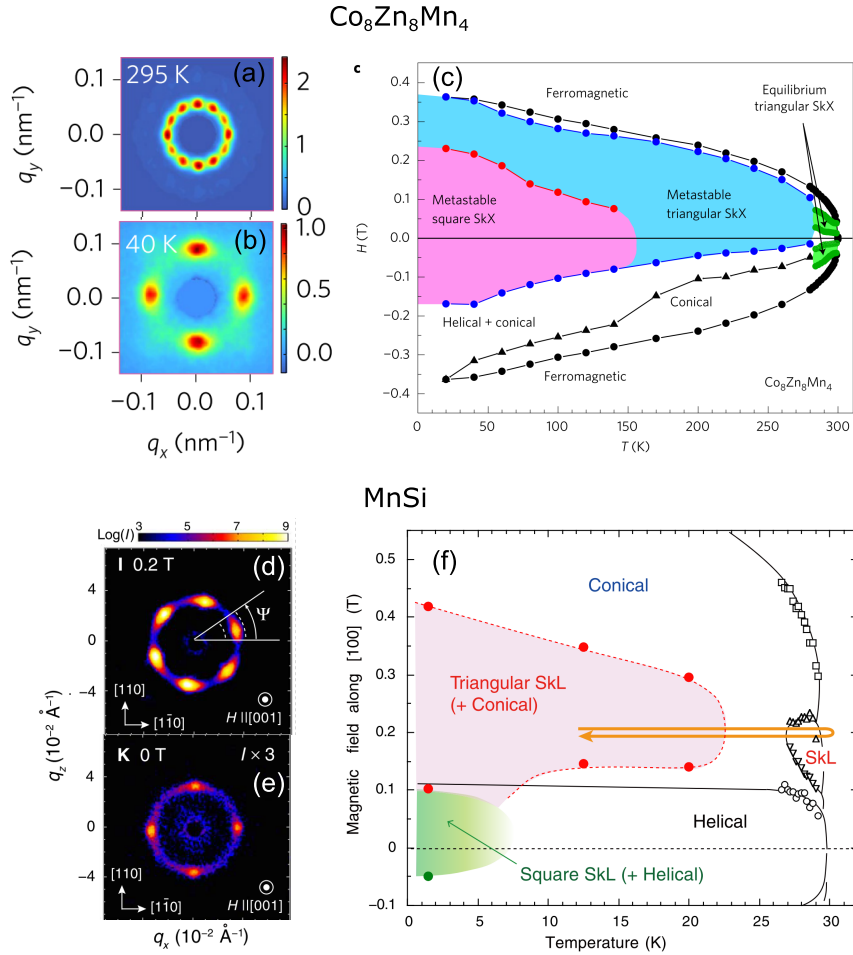
Figure 1.8: Small angle neutron scattering patters of triangular lattice of skyrmion (a) and square lattice of skyrmions (b) in $Co_8Zn_8Mn_4$. The 12 spots in Fig 1.8(a) originate from two types of domains of triangular lattice skyrmion, in which one q of three-q is aligned along [100] or [010]. (c) Magnetic phase diagram of $Co_8Zn_8Mn_4$ including the metastable skyrmion phase. Small angle neutron scattering patters of triangular lattice of skyrmion (d) and square lattice of skyrmions (e) in MnSi. (f) Magnetic phase diagram of MnSi including the metastable skyrmion phase. Reproduced from Ref [20, 21].

1.2.2 Chiral spin fluctuations

Up to this point, we have reviewed the static chiral spin structures, namely helical, conical and skyrmion structures. Next, we review dynamical chiral spin stricture.

As mentioned above, in the chiral magnets chirality of spin winding structures is determined by handedness of the corresponding lattice structures. For example, in MnSi, the long-period chiral spin structures form below the magnetic ordering temperature $T_c = 29.5$ K. However, even above T_c, where the long-range magnetic orders disappear, short-range spin correlations still survive without losing the chiral nature, which is called chiral spin fluctuations [22, 23, 24, 25].

Chirality of spin structures can be ascertained by using polarized neutron scattering. The cross-section for polarized neutron is given by [26]

$$\frac{d^2\sigma}{d\Omega d\omega} \propto \int dt e^{i\omega t} \langle \boldsymbol{S_Q} \cdot \boldsymbol{S_{-Q}}(t) \rangle + i(\boldsymbol{Q} \cdot \boldsymbol{P}) \left(\boldsymbol{Q} \cdot \int dt e^{i\omega t} \langle \boldsymbol{C}(t) \rangle \right), \qquad (1.3)$$

$$\boldsymbol{C}(t) = \boldsymbol{S_Q}(0) \times \boldsymbol{S_{-Q}}(t), \qquad (1.4)$$

where $\boldsymbol{S_Q}$, $\boldsymbol{Q}$, and $\boldsymbol{P}$ are the Fourier component of a spin structure, the scattering vector, and the polarization of the incident neutron, respectively, and $\boldsymbol{C}(t)$ represents chirality of spin structures (vector spin chirality). The second term predicts that if $\langle \boldsymbol{C}(t) \rangle$ is nonzero, there is the difference between the scattering intensities of experimental setup with $\boldsymbol{Q}$ parallel to $\boldsymbol{P}$ and $\boldsymbol{Q}$ anti-parallel to $\boldsymbol{P}$. The relation is reversed by changing the sign of either $\boldsymbol{P}$ or $\boldsymbol{C}(t)$. In Fig. 1.9 (a)-(d), we show small-angle polarized neutron scattering (SAPNS) patterns for two directions of the polarization of the incident neutron in the left-handed MnSi both above and below T_c. At $T = 28.7K < T_c$, the four Bragg spots are observed along $\langle 111 \rangle$ directions; the intensity of Bragg spots perpendicular to $\boldsymbol{P}$ are independent of the direction of $\boldsymbol{P}$, whereas the intensity of Bragg spots almost parallel to $\boldsymbol{P}$ depend on the direction of $\boldsymbol{P}$ in accord with the expected behavior in the scattering from the homochiral helical structure [Fig. 1.9 (a) and (b)] [23]. At $T = 29.1K > T_c$, the semicircular diffuse patterns oriented along $\boldsymbol{P}$ direction are observed, indicating the vector spin chirality remains even in the paramagnetic phase [Fig. 1.9 (c) and (d)]. This is further confirmed by temperature dependence

of the polarization of the scattering defined as

$$P_s = \frac{\sigma(\boldsymbol{P}) - \sigma(-\boldsymbol{P})}{\sigma(\boldsymbol{P}) + \sigma(-\boldsymbol{P})}. \tag{1.5}$$

The polarization of the scattering represents the fraction of the dominant chiral domain: $P_s = 1$ for a single chiral domain and $P_s = 0$ for a fully disordered state or equal populated chiral domains. A shown in [Fig 1.9 (e)], below T_c, the absolute value of P_s is almost one, being consistent with the formation of the homochiral helical structure. Above T_c, P_s still remains finite, and P_s is approximately 0.5 even at $T = 33$ K, which indicates short-range spin correlations still survive without losing the chiral nature.
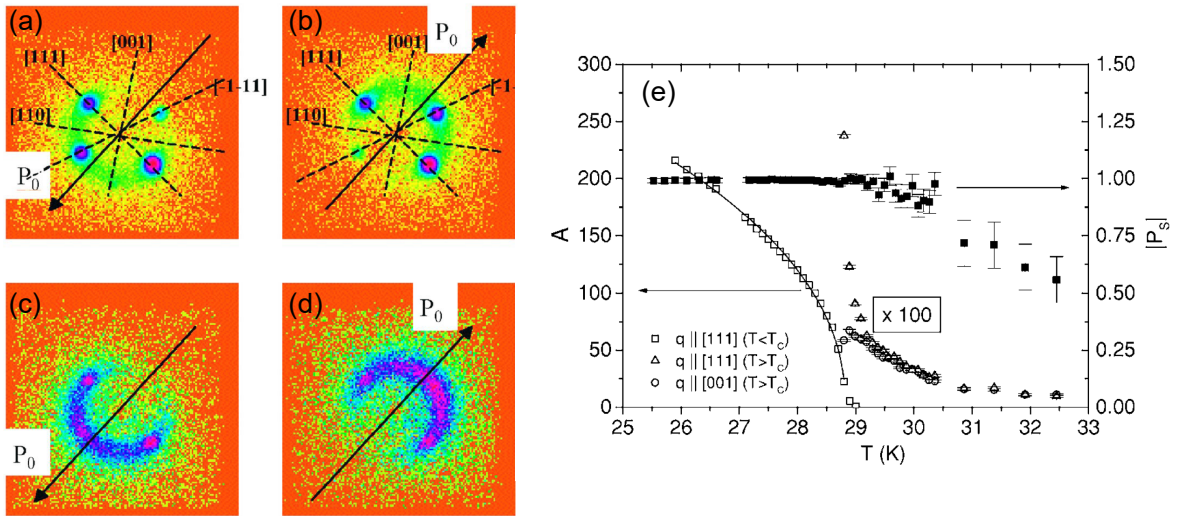
Figure 1.9: (a, b) Small angle polarized neutron scattering (SAPNS) patterns in MnSi below T_c with different polarization directions. (c, d) SAPNS patters above T_c. (e) The temperature dependence of the intensity of Bragg spots (left) and polarization of the scattering P_s (right). Reproduced from Ref [23].

1.2.3   Partial order state

In MnSi, the long-range static helical order is suppressed under pressure, and disappears at the critical pressure of $p_c = 14.6$ kbar [27, 28, 29]. Above p_c, neutron diffraction reveals the quasi-static magnetic order, called partial oder (PO) [Fig. 1.10 (a)] [27]. which fluctuates on the time scales between 10^{-10} s and 10^{-11} s [28]. In addition, in PO phase, topological Hall signal whose magnitude is almost the same as that of the triangular skyrmion lattice has been observed, which indicates that PO has the same topology as that of the skyrmions [Fig. 1.10 (b)] [29].
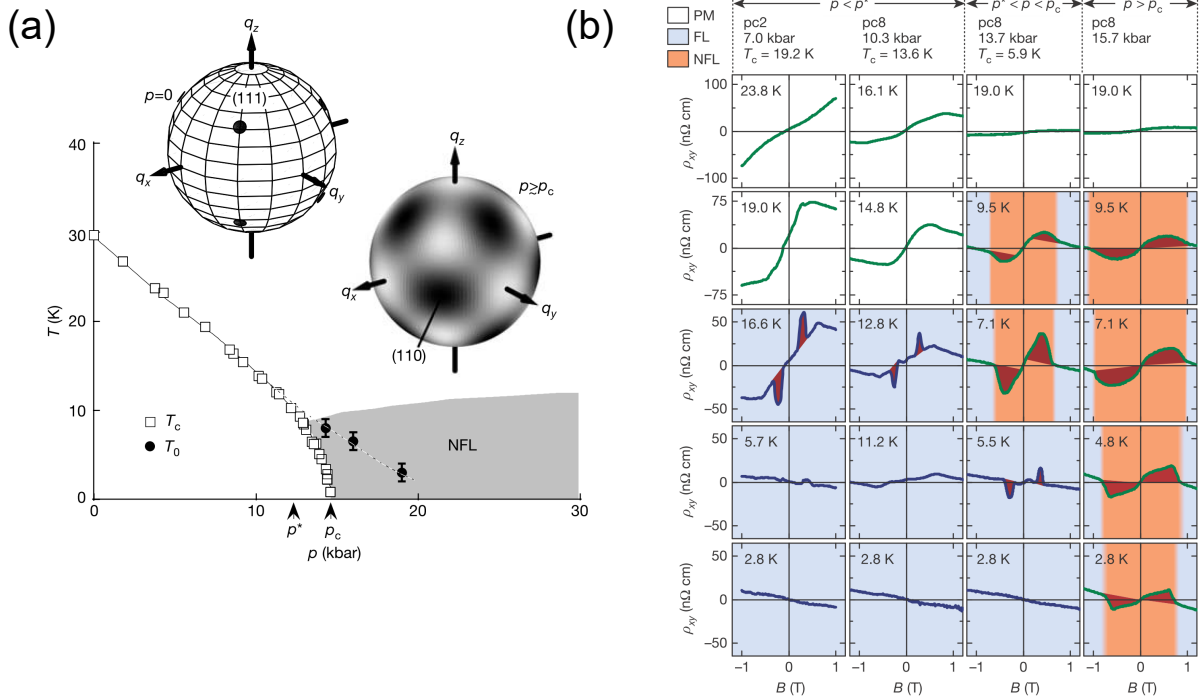
Figure 1.10:   (a) Temperature(T)-pressure(p) phase diagram of MnSi. Gray shadow shows partial order region. The insets schematically represent magnetic scattering intensity in reciprocal sphere at ambient pressure (left) and above the critical pressure (right). (b) Magnetic field dependence of Hall resistivity in MnSi at various temperatures and pressures. Orange shadows show partial order region. Reproduced from Ref [27, 29].

1.2.4   Other chiral spin structures

Chiral soliton lattice

In the monoaxial chiral magnet of $CrNb_3S_6$, ferromagnetic layers are coupled through the interlayer exchange interaction and DM interaction. Hence, long-period (48 nm) helical spin structure forms at $T_N = 127$ K [Fig. 1.11 (a)]. When the magnetic field is applied perpendicular to the helical axis, the helical state transforms to the nonlinear magnetic order called chiral soliton lattice, which consists of induced ferromagnetic domains and 360° domain walls, without inclination of the propagation direction due to the strong planar magnetic anisotropy [Fig. 1.11 (b)] [30, 31]. Formations of a magnetic structure similar to the chiral soliton lattice are also proposed in thin films of $B20$-type compounds, in which helical axis is strongly pinned by anisotropic effect due to the epitaxial strain of the thin films [101].
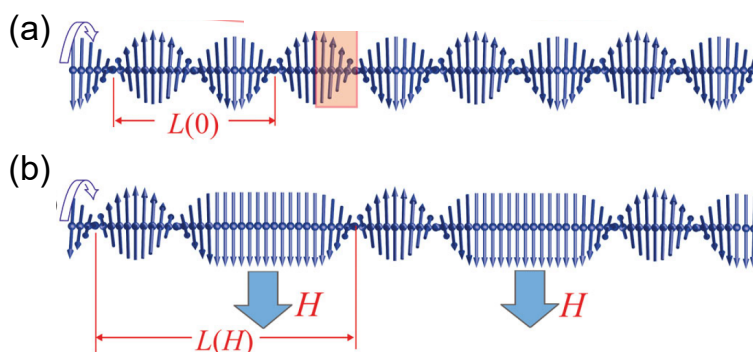
Figure 1.11: Schematic illustrations of helical structures (a) and chiral soliton lattice (b) Reproduced from Ref. [30].

Three dimensional hedgehog lattice

The triangular lattice of the skyrmion can be viewed as the superposition of the three helical structure with $\bm{q}$ vectors forming an angle of 120° within a plane

perpendicular to the magnetic field. In contrast, in B20-type MnGe three $\boldsymbol{q}$ are oriented along $\langle 100 \rangle$ axes of the underlying crystal perhaps due to the relatively strong cubic magnetic anisotropy [34, 35, 36]. The superposition of three $\boldsymbol{q}$ vectors orthogonal to each other forms a non-trivial chiral spin structure [Fig. 1.11 (a)], which contains hedgehog and anti-hedgehog spin structures as shown in Fig. 1.11 (b).
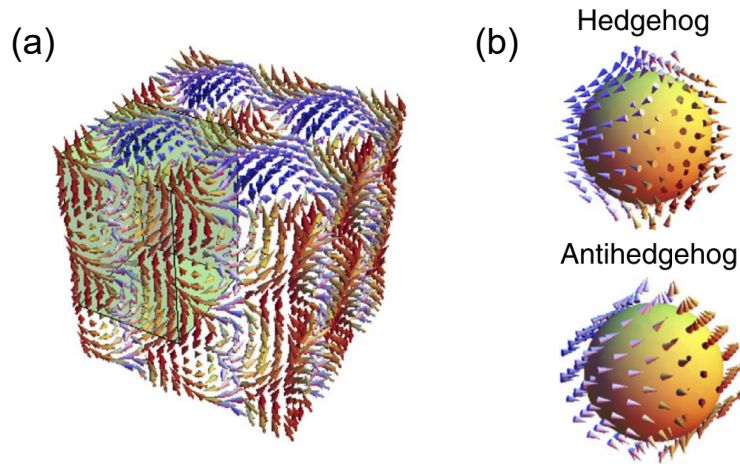
Figure 1.12: Schematic illustrations of spin structures of three dimensional hedgehog lattice (a) and hedgehog and anti hedgehog (b). Reproduced from Ref [36].

1.3 Transport properties in chiral magnets

A quantum state acquires an additional phase during the adiabatic evolution in which the quantum state confined within a portion of Hilbert space [37]. This phase is called the Berry phase, which is an fundamental concept describing topological and geometric properties of condensed matter [38]. In magnetic metals, for example, momentum-space Berry phase leads to anomalous Hall effect (AHE). In addition, conduction electrons passing through non-coplanar spin structures such as skyrmions acquire the real-space Berry phase, which leads to topological Hall

effect. In this section, we provide a brief review of transport phenomena in chiral magnets.

1.3.1 Anomalous Hall effect

Anomalous Hall effect was first reported in 1881 by E. H. Hall [39]. Currently, mainly three distinct contributions to AHE are recognized [40]: (1) the skew scattering mechanism, (2) the side jump mechanism, and (3) the intrinsic mechanism. The first and second mechanisms originate from electron scattering. Especially, the skew scattering is dominant in clean metals with the conductivity higher than $\sigma = 10^6 \Omega^{-1} \text{cm}^{-1}$. In contrast, the intrinsic mechanism originates from the band structure and is dominant in metals with $10^4 < \sigma < 10^6 \, \Omega^{-1}\text{cm}^{-1}$[41]. Here, we focus on the intrinsic mechanism because the conductivity of MnSi of the present focus is approximately $\sigma \approx 10^5 \Omega^{-1}\text{cm}^{-1}$, which is within the range of conductivity where the intrinsic mechanism is dominant.

The intrinsic mechanism was proposed by Karplus and Luttinger (KL) [42]. When an external electric field is applied, conduction electrons acquires an additional contribution to the group velocity perpendicular to the current direction, which is called anomalous velocity. The summation of anomalous velocity over the occupied states is nonzero in the case of ferromagnetic metals, inducing Hall effect. Recently, the close relationship between the anomalous velocity and the momentum-space Berry phase has been revealed, and the intrinsic mechanism has been reconstructed in terms of the momentum-space Berry phases [43, 44]. The group velocity of electron can be described as

$$\frac{d\boldsymbol{r}}{dt} = \frac{\partial \epsilon_n(\boldsymbol{k})}{\partial \boldsymbol{k}} + \boldsymbol{b}_n(\boldsymbol{k}) \times \boldsymbol{E} \tag{1.6}$$

$$\boldsymbol{b}_n(\boldsymbol{k}) = \boldsymbol{\nabla}_{\boldsymbol{k}} \times \boldsymbol{A}_n(\boldsymbol{k}) = \boldsymbol{\nabla}_{\boldsymbol{k}} \times (i\langle n|\boldsymbol{\nabla}_{\boldsymbol{k}}|n\rangle). \tag{1.7}$$

The second term is the anomalous velocity, and $\boldsymbol{A}_n(k)$ and $\boldsymbol{b}_n(\boldsymbol{k})$ are the Berry connection and the Berry curvature, respectively. The Hall conductivity is given

by

$$\sigma_{xy}^{\text{AH−int}} = \frac{e^2}{\hbar} \int \frac{d\boldsymbol{k}}{(2\pi)^d} f(\epsilon) b_n^z. \tag{1.8}$$

Anomalous Hall conductivity $\sigma_{xy}^{\text{AH−int}}$ depends only on the band structure and is independent of scattering time τ, and hence the Hall resistivity $\rho_{yx} \approx \sigma_{xy}/\sigma_{xx}^2$ is proportion to $\rho_{xx}^2 = \tau^{-2}$.

1.3.2 Topological Hall effect

The real-scape Berry phase also induces Hall effect, which is termed topological Hall effect (THE) [45, 46, 47, 48]. In principle, THE emerges in non-coplanar spin structure, in which adjacent three spins ($\boldsymbol{S}_1$, $\boldsymbol{S}_2$, and $\boldsymbol{S}_3$) produce nonzero scalar spin chirality $\boldsymbol{S}_1 \cdot (\boldsymbol{S}_2 \times \boldsymbol{S}_3)$, which corresponds to the solid angle Ω subtended by $\boldsymbol{S}_i$. A conduction electron whose spin aligned to the direction of $\boldsymbol{S}_i$ obtain a phase factor equal to the half of the solid angle Ω. (Fig. 1.13). The phase acquired by conduction electrons acts as the magnetic flux in analogy to the Aharonov-Bohm effect, and consequently leads the Hall effect. In the continuum approximation, the phase factor can be given by the flux of emergent magnetic field described as [4, 49]

$$b_z = \frac{h}{8\pi e} \boldsymbol{n} \cdot \left(\frac{\partial \boldsymbol{n}}{\partial x} \times \frac{\partial \boldsymbol{n}}{\partial y} \right). \tag{1.9}$$

Therefore, the emergent magnetic flux for a skyrmion is h/e in the strong coupling limit (see also Eq. 1.1). In a triangular lattice of skyrmions, each skyrmion with the emergent flux h/e leads to almost an uniform emergent magnetic field as following:

$$\langle b_z \rangle = \frac{\sqrt{3}}{2\lambda^2} \frac{h}{e}, \tag{1.10}$$

where $2\lambda/\sqrt{3}$ is the lattice constant of a triangular lattice of skyrmion. For example, for MnSi with $\lambda = 18$ nm $\langle b_z \rangle$ is 11 T and for FeGe with $\lambda = 70$ nm $\langle b_z \rangle$ is 0.7 T.

Because the emergent magnetic field acts like magnetic field, the topological

Hall resistivity can be described as

$$\rho_{yx}^{\text{THE}} = PR_0 b_z, \tag{1.11}$$

where R_0 is normal Hall coefficient, and $P = (n_\uparrow - n_\downarrow)/(n_\uparrow + n_\downarrow)$ is the spin polarization of conduction electrons, with $n_\uparrow$ and $n_\downarrow$ being the density of spin-up and spin-down carriers; the factor P arises because the sign of the emergent magnetic for the up-spin carriers is opposite to that for down-spin carriers.
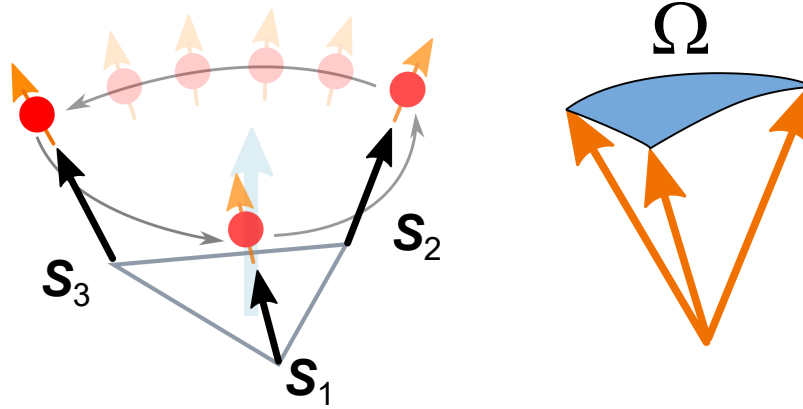
Figure 1.13: Schematic view of scalar spin chirality. Black arrows ($\boldsymbol{S}_1$, $\boldsymbol{S}_2$, and $\boldsymbol{S}_3$) represent local spins and orange arrows represent the spin of conduction electrons whose spin aligned to the direction of local spins. Ω is the solid angle subtended by $\boldsymbol{S}_i$.

Figure 1.14 is the topological Hall contributions in the equilibrium [Fig. 1.14(a)] [49] and metastable [Fig. 1.14(b)] [19] skyrmion phase of MnSi. The magnitude of ρ_{yx}^{THE} is 4.5 nΩ cm, whereas the metastable skyrmion phase at low temperatures induces one order of magnitude larger ρ_{yx}^{THE} of 35 nΩ cm. This is perhaps because spin polarization P increases at low temperatures. The large enhancements of topological Hall effect at low temperatures have also been reported for equilibrium skyrmion phases just below T_c in MnSi under pressure [18] and in

$Mn_{1-x}Fe_xSi$ [50], where T_c continuously decreases from T_c of MnSi at ambient pressure with the increase in hydrostatic pressure or Fe concentration.
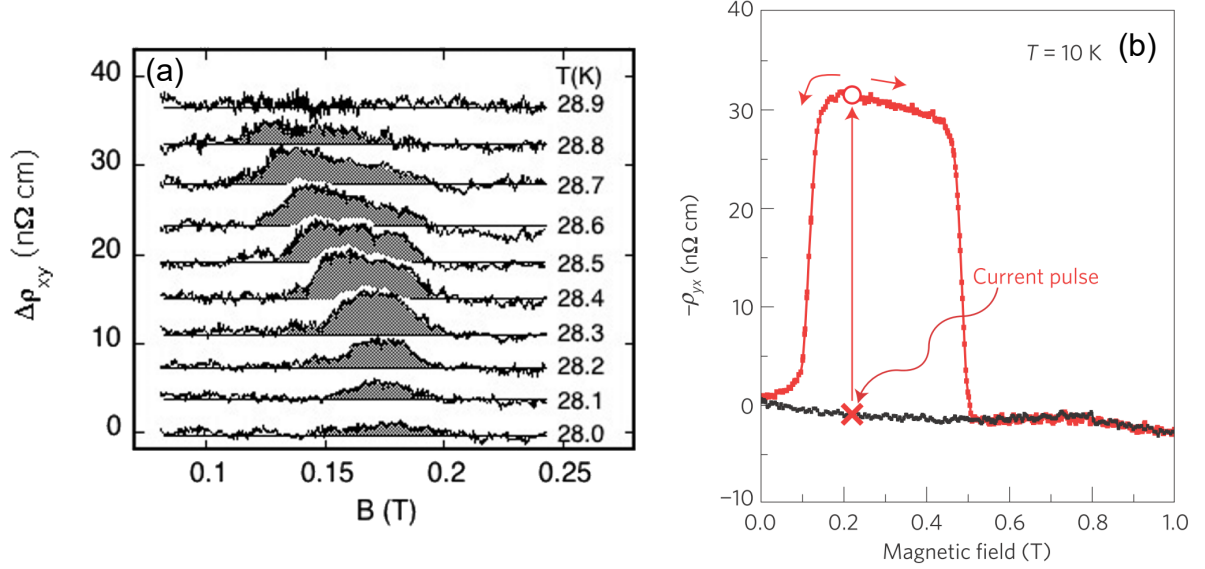
Figure 1.14: Topological Hall effect in the equilibrium skyrmion phase (a) and the metastable skyrmion phase at low temperatures (b) in MnSi. Reproduced from Ref. [49, 19].

1.3.3   Current induced motion of skyrmion

Topological properties of skyrmion play an important role also in current induced dynamics of skyrmions. The conduction electrons can drive underlying spin texture such as ferromagnetic domain walls and skyrmions though exchange of the angular moment (i.e. spin transfer torque). The threshold current density required for the translational motion of skyrmoin (typically $10^6 A/m^2$) [51, 52, 53] is five or six orders of magnitude smaller than that of ferromagnetic domains (typically $10^{11} - 10^{12} A/m^2$) [54, 55]. This property results mainly from the topological nature of a skyrmion, stimulating research on the skyrmion-based non-volatile energy-saving memory devices [56, 57, 58, 59]. The equation of motion of the

center of mass of a skyrmion can be described as

$$m_{\text{sk}}\frac{d\boldsymbol{v}_{\text{sk}}}{dt} + \boldsymbol{G} \times (\boldsymbol{v}_{\text{e}} - \boldsymbol{v}_{\text{sk}}) - k(\alpha\boldsymbol{v}_{\text{e}} - \beta\boldsymbol{v}_{\text{sk}}) = -\boldsymbol{F}_{\text{pin}}, \tag{1.12}$$

where $\boldsymbol{v}_{\text{sk}}$, $\boldsymbol{v}_{\text{e}}$, m_{sk}, $\boldsymbol{F}_{\text{pin}}$, $\boldsymbol{G}$, and k are the drift velocity of the skyrmion, the drift velocity of the electrons, the mass of the skyrmion, the pinning force, gyrovector, and a dimensionless constant, respectively. The gyrovector originates from topological nature of spin object and given by $\boldsymbol{G} = (0, 0, 4\pi N_{\text{sk}})$ for the skyrmion and $\boldsymbol{G} = (0, 0, 0)$ for the non-topological spin objects such as ferromagnetic domain wall. Hence, in the case of a skyrmion, the second term with $|\boldsymbol{G}| = 4\pi$ is dominant in Eq. 1.12, and the order of threshold current density can be estimated as $|\boldsymbol{F}_{\text{pin}}|/|\boldsymbol{G}|$. In contrast, in the case of the non-topological spin object, because $|\boldsymbol{G}|$ is zero, $|k\beta|$ is dominant in Eq. 1.12, and the order of threshold current density can be estimated as $|\boldsymbol{F}_{\text{pin}}|/|k\beta|$, which is much larger than that for the skyrmion.

From Eq. 1.12, the drift velocity of skyrmion driven by DC current is derived as [57, 58],

$$\boldsymbol{v}_{\parallel} = \left(\frac{\beta}{\alpha} + \frac{\alpha - \beta}{\alpha^3(k/|\boldsymbol{G}|)^2 + \alpha^2}\right), \tag{1.13}$$

$$\boldsymbol{v}_{\perp} = \frac{(\alpha - \beta)(k/|\boldsymbol{G}|)}{\alpha^2(k/|\boldsymbol{G}|)^2 + 1}, \tag{1.14}$$

where $\boldsymbol{v}_{\parallel}$ and $\boldsymbol{v}_{\perp}$ are the components of the skyrmion velocity parallel and perpendicular to the current direction, respectively. Here, we neglect $\boldsymbol{F}_{\text{pin}}$. The transversal motion of skyrmion in reference to the current direction is termed as skyrmion Hall effect. Figure 1.15 (a) is the snapshots of a current-induced motion of a Neel-type skyrmion in a bilayer of $Ta/Co_{20}Fe_{60}Co_{20}$ taken by using a polar magneto-optical Kerr effect (MOKE) [60]. The skyrmion moves both parallel and perpendicular to the current direction. This is further confirmed by the trajectory of the skyrmion as shown in Fig. 1.15 (b). We note Eq 1.12 holds regardless of helicity of skyrmion.

In electromagnetism, the change in magnetic flux induces an electric field (Faraday's law of induction). Since a skyrmion acts as an emergent magnetic
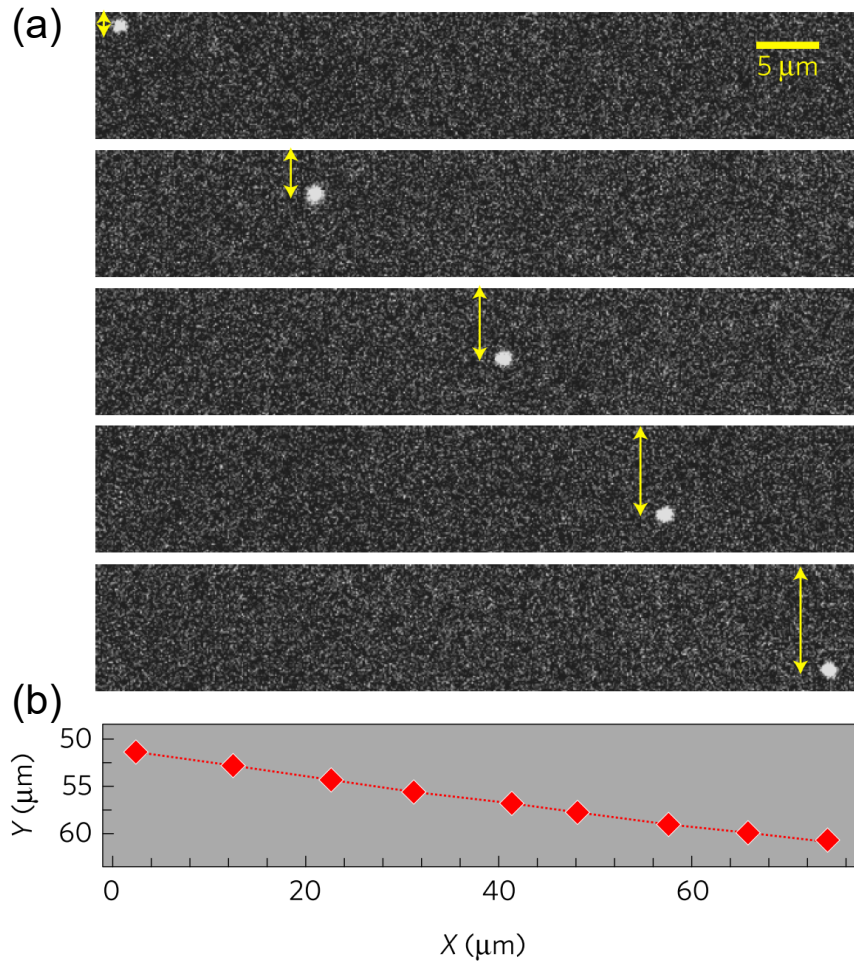
Figure 1.15: (a) Snapshots of current-induced motion of skyrmion in Ta/Co$_{20}$Fe$_{60}$Co$_{20}$ taken by using a polar magneto-optical Kerr effect. (b) The trajectory of skyrmion. Reproduced from Ref. [60].

flux, the skyrmion motion induces an electric field in analogy to Faraday's law, which is called as emergent electric field [4, 52]. The emergent electric field is given by

$$e_i = \frac{h}{2\pi e} \boldsymbol{n} \cdot \left(\frac{\partial \boldsymbol{n}}{\partial i} \times \frac{\partial \boldsymbol{n}}{\partial t} \right). \tag{1.15}$$

From Eq. 1.9, the emergent electric field is related to the emergent magnetic field as $\boldsymbol{e} = -\boldsymbol{v}_{\mathrm{sk}} \times \boldsymbol{b}$. Because the direction of the emergent electric field is opposite to that of topological Hall field, the magnitude of Hall resistivity is reduced when the skyrmion moves. Figure 1.16 is the current density dependence of Hall resistivity in MnSi [52]. The Hall resistivity decreases only in the skyrmion phase above a threshold current density $j_{\mathrm{c}} \approx 0.5 - 2 \times 10^6 \, \mathrm{A/m^2}$.

1.4 Basic information of MnSi

In this section, we briefly summarize basic information of B20-type MnSi.

The crystal structure of B-20 type MnSi belongs to the space group of $P2_13$. The unit cell of MnSi contains four Mn atoms and four Si atoms [Fig. 1.17 (a)], and there exist two enantiomeric forms: right- and left-handed structures. Crystal structures of right- and left-handed MnSi viewed from the [111] direction are shown in Fig. 1.17 (b) and (c), respectively. We define the right- and left-handed MnSi as the atomic coordinates (u, u, u), $(1/2+u, 1/2-u, 1/2-u)$, $(1/2-u, -u, 1/2+u)$, $(-u, 1/2+u, 1/2-u)$ with $u_{\mathrm{Mn}} = 0.863$, $u_{\mathrm{Si}} = 0.155$ and with $u_{\mathrm{Mn}} = 0.137$, $u_{\mathrm{Si}} = 0.845$, respectively.

As already mentioned, due to the competition between the ferromagnetic exchange interaction and the DM interaction, there emerge various spin winding structures, whose modulation directions, i.e. magnetic helicity, are determined by handedness of the corresponding lattice structures. Below the magnetic ordering temperature $T_{\mathrm{c}} = 29.5$ K, the long-period (18 nm) helical spin structure forms [61]. In addition, skyrmions condense in triangular-lattice (SkL) at 0.1 T $\leq B \leq$ 0.3 T just below T_{c} [see Fig. 1.5 (a)] [7]. Above T_{c}, where the long-range
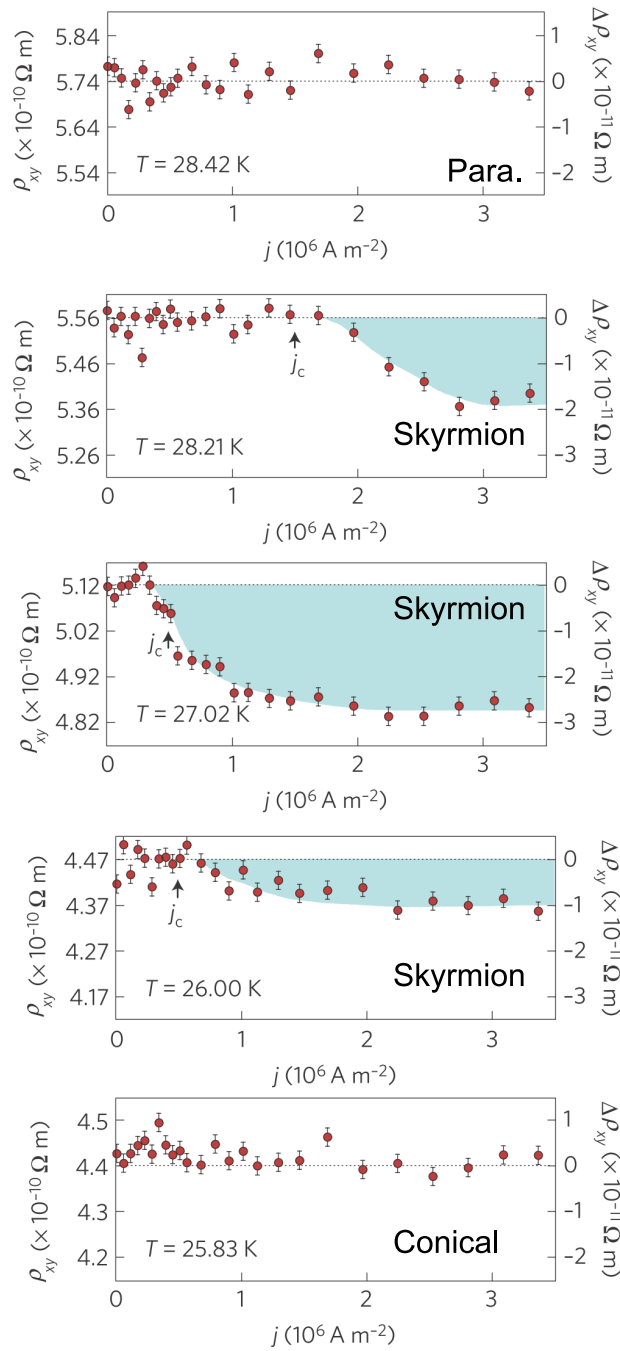
Figure 1.16: Current density dependence of Hall resistivity in MnSi at various temperatures. The light blue shadows represent the reduction of Hall resistivity due to emergent electric field originating from current-induced skyrmion motion. Reproduced from Ref. [52].
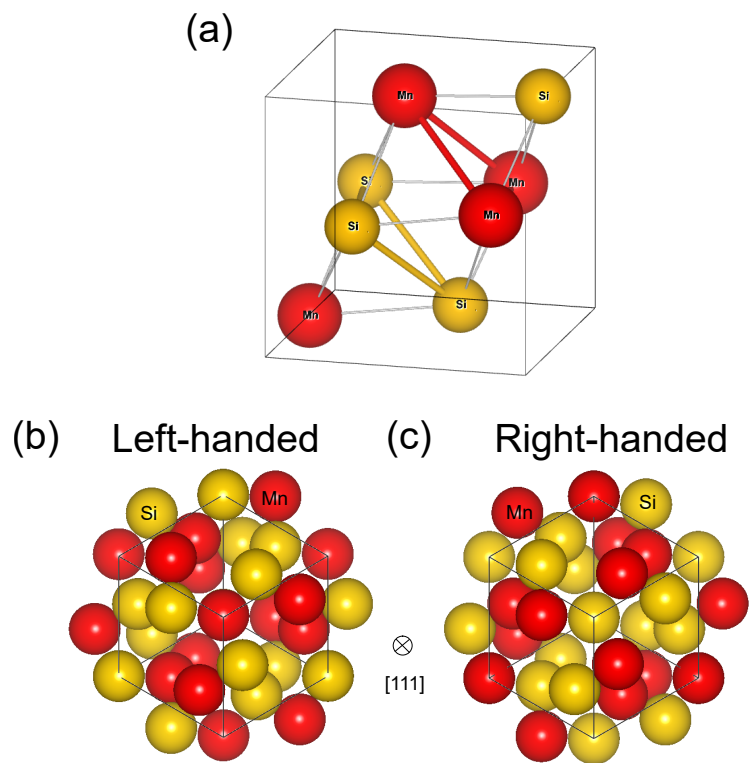
Figure 1.17: (a) Crystal structures of MnSi. Crystal structures of left- (b) and right- (c) handed MnSi viewed from the [111] direction.

magnetic orders disappear, short-range spin correlations still survive without losing the chiral nature (see the section 1.2 2 for the details) [22, 23, 24, 25].

1.5   Purpose of this thesis

The concept of topology is related to fundamental and remarkable transport phenomena, and chirality also produces unique responses. As introduced in the above sections, spin structures in chiral crystal also have chirality due to Dzyaloshinskii-Moriya (DM) interaction. Furthermore, some chiral spin structures such as skyrmion also have nontrivial topology. We envisage that chirality and topology of chiral spin structures produce novel transport phenomena and these phenomena can provide a basic principle of novel electronic devices. However, these phenomena have not been well investigated. Therefore, in this Thesis, we investigate transport phenomena in which both chiral and topological properties of skyrmion and chiral spin structures play crucial roles.

In chapter 3, we investigate anisotropic magnetoresistance related to the modulation of chiral spin structures in bulk samples of MnSi. For this purpose, we focus on planar Hall effect, which is a sensitive probe for anisotropic magnetoresistance. Planar Hall effect sensitively detects the 90°-flop of the magnetic modulation vector upon the skyrmion formation and destruction, showing the prominent stepwise anomaly in the skyrmion phase. This finding provides a new underlying principle for the establishment of a method to detect skyrmion formation.

In Chapter 4 and 5, we investigate nonreciprocal and current-nonlinear transport phenomena. which are allowed in the chiral systems from the viewpoint of symmetry. Here, nonreciprocal response in the nonlinear transport phenomena is defined as different responses against positive and negative current $(\pm j)$ when viewed from the current direction. In Chapter 4, we investigate the electrical magnetochiral effect (eMChE), which is nonreciprocal magnetotransport effect with the resistance proportional to the inner product of magnetic field and

current. Prominent eMChE signals emerge at specific temperature-magnetic field-pressure regions: in the paramagnetic phase just above the helical ordering temperature and in the partially-ordered topological spin state at low temperatures and high pressures. Electrical magnetochiral effect is also discerned at the phase boundary of the equilibrium skyrmion phase and in the amorphous-like metastable skyrmion phase. In chapter 5, we demonstrate that the current-induced asymmetric deformation of skyrmion strings arising from both its flexible nature and the Dzyaloshinskii-Moriya interaction results in nonreciprocal nonlinear Hall effect related to the real-space Berry phase. These results demonstrate the topology and chirality of spin structure give birth to novel current-nonlinear transport phenomena.

In Chapter 6, we investigate stability of skyrmions in thin films by using measurements of topological Hall effect and planar Hall effect. When in-plane magnetic field is applied, in-plane skyrmion, which is an array of skyrmion strings stretching in the plane of the thin films, are stabilized at low temperatures. In contrast, when out-of-plane magnetic field is applied, the quasi-two-dimensional skyrmion is stabilized, and the number of the quasi-two-dimensional skyrmion is the largest in the vicinity of T_c. These results provide an insight into the stabilization mechanism of skyrmions in thin films.

In Chapter 7, we summarize the results and conclude this thesis.

Chapter 2

Experimental Method

2.1 Fabrication of thin plate devices

We fabricated microscale thin plates of MnSi, whose thickness and width are approximately 500 nm and 10 μm, by using focused ion beam (FIB) technique (NB-5000, Hitachi). The detailed procedure is as follows:

1. We cut a plate of MnSi (typically 3μm $\times 15\mu$m $\times 30\mu$m) out of single crystals of MnSi, which Ms. Kikkawa (RIKEN) synthesized with use of the Czochralski method. The crystalline chirality was confirmed by using convergent beam electron diffraction (CBED) method by Dr. Morikawa (RIKEN). The plate was picked up by using a micro-sampling probe [Fig. 2.1 (a)].

2. The picked up thin plate was fixed on a copper plate with the use of the FIB-assisted tungsten deposition. Then we thinned the plate until the thickness reached approximately 500 nm by using focused Ga ion beam. [Fig. 2.1 (b)].

3. We deposited gold electrodes on a silicon substrate by using photolithography and electron-beam deposition. The thin plate is mounted on the silicon
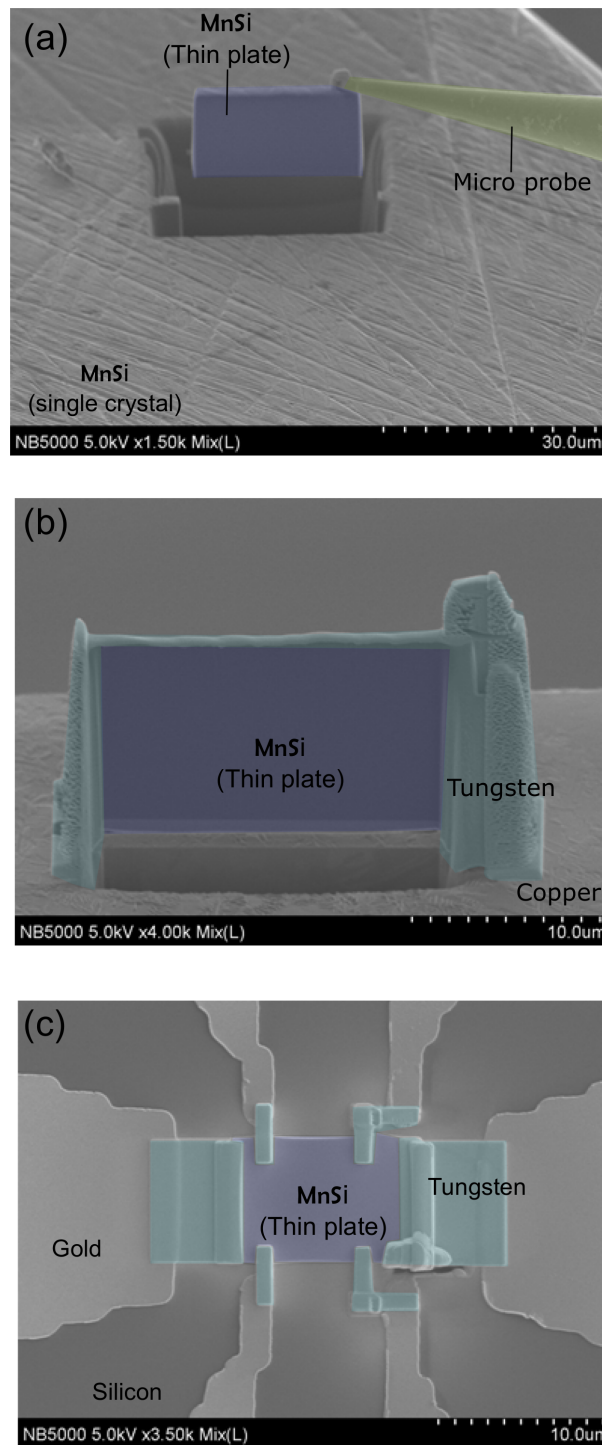
Figure 2.1: Scanning Electron Microscopy (SEM) images of the fabrication process of a thin plate device

substrate and fixed by using the FIB-assisted tungsten deposition. Finally, we connected the thin plate to the gold electrodes with the use of either the FIB-assisted tungsten deposition or gold deposition by using photolithography and electron-beam deposition. [Fig. 2.1 (c)].
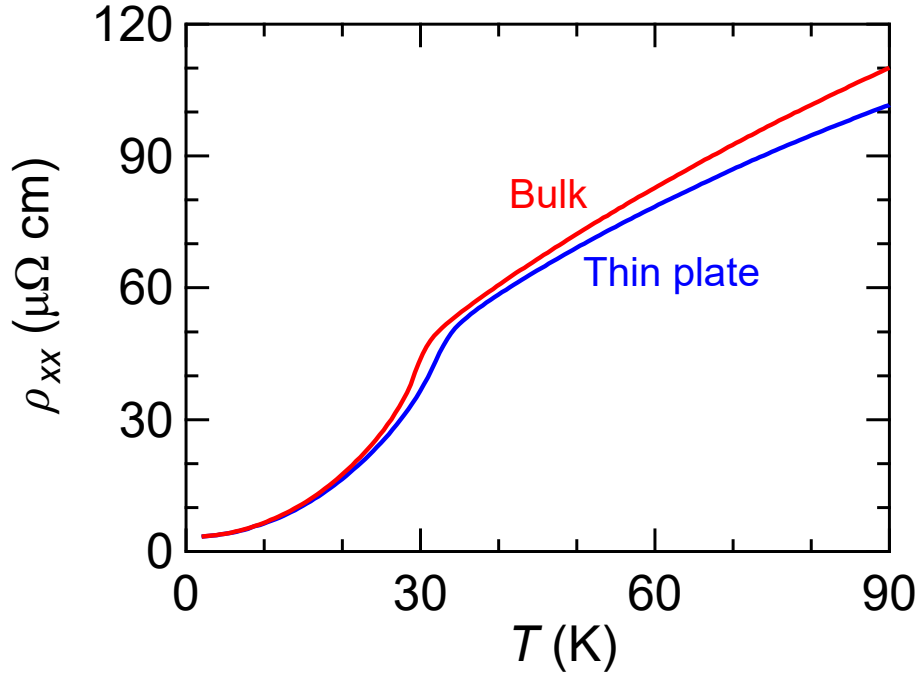
Figure 2.2: Comparison of temperature dependence of resistivity (ρ_{xx}) between bulk sample (red line) and thin plate sample of MnSi (blue line).

Temperature dependence of resistivities and magnetic phase diagram of thin plate samples resemble those of bulk samples. In Fig. 2.2, we compare linear longitudinal resistivity (ρ_{xx}) of a MnSi thin plate sample with that of bulk single crystal, out of which we sliced the thin plate. Resistivities of two samples show similar T dependence, indicating minimal damage due to FIB fabrication process. We determined the transition temperature of the helical ordering as the temperature where $\rho_{xx} - T$ curve exhibits an inflection. Note that the slight increase of transition temperature in the thin plate sample compared to that of the bulk is due to perhaps uniaxial strains from the silicon sample stage.
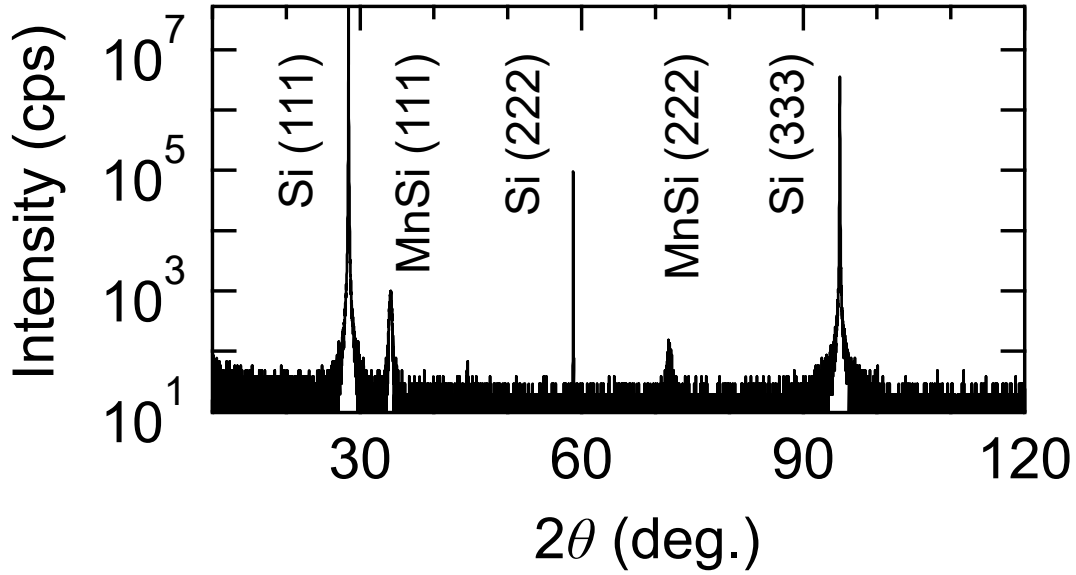
Figure 2.3: X ray diffraction patterns of MnSi thin film

2.2 Thin-film growth

$Mn_{1-x}Fe_xSi$ epitaxial films were grown on highly-resistive Si(111) substrates ($\rho >$ $1000\,\Omega$cm) by solid phase epitaxy. All the components (Mn, Fe, and Si) were deposited on the wafer using Knudsen cells. We made a seed layer of MnSi by depositing 4-monolayer Mn at room temperature onto a Si(111)-7×7 surface followed by annealing at 200 °C. Then, Mn, Fe, and Si were deposited alternately at room temperature until a prescribed thickness was reached. The film temperature was raised until the characteristic $\sqrt{3} \times \sqrt{3}$ reflection high-energy electron diffraction (RHEED) pattern on the B20-compound (111) surface appeared, and then held for 5 minutes to anneal the sample. All the films are subject to the compressive strain of about -0.3 % normal to the plane due to the in-plane tensile strain from the lattice mismatch of -3 %. The single phase nature of B20-$Mn_{1-x}Fe_xSi$ was confirmed in all the films by 2θ-θ X-ray diffraction [Fig. 2.3].

2.3   Magnetization and transport measurement

Magnetization and longitudinal resistivity and Hall resistivity were measured by using Magnetic Property Measurement System (MPMS) and Physical Property Measurement System (PPMS). Hydrostatic pressures were applied with use of a CuBe clamp cell, and the applied pressures were calibrated with pressure change of superconducting transition temperature of Pb. Second harmonic resistivity was measured by using a Lock-in technique (SR-830, Stanford Research Systems); we input low-frequency (f) ac current and measured second harmonic resistivity.

Chapter 3

Planar Hall effect in MnSi

3.1 Introduction

In practicalized magnetic storage devices such as hard disk drives and magneto-optical drives, which store information as the magnetization direction, various phenomena have been used to read out the magnetization direction. One of them is anisotropic magnetoresistance (AMR) effect, i.e difference between magnetoresistance with $\boldsymbol{M} \perp \boldsymbol{j}$ ($\rho^{\perp \boldsymbol{M}}$) and $\boldsymbol{M} \parallel \boldsymbol{j}$ ($\rho^{\parallel \boldsymbol{M}}$) [62, 63]. When magnetization lies in-plane, longitudinal resistivity in polycrystalline samples can be described as

$$\rho_{xx} = \rho^{\perp \boldsymbol{M}} + (\rho^{\parallel \boldsymbol{M}} - \rho^{\perp \boldsymbol{M}}) \cos^2 \theta_{\boldsymbol{M}}, \qquad (3.1)$$

where $\theta_{\boldsymbol{M}}$ is the relative angle between the current ($\boldsymbol{j}$) and the magnetic field. Anisotropic magnetoresistance leads to the transversal voltage, so-called planar Hall effect [64, 65, 66, 67, 68]. Planar Hall resistivity ρ_{yx}^{PHE} is described as

$$\rho_{yx}^{\mathrm{PHE}} = \frac{1}{2}(\rho^{\parallel \boldsymbol{M}} - \rho^{\perp \boldsymbol{M}}) \sin 2\theta. \qquad (3.2)$$

Hence planar Hall effect can sensitively extract difference in magnetoresistance between $\rho^{\perp \boldsymbol{M}}$ and $\rho^{\parallel \boldsymbol{M}}$, and a relative angle between magnetization and current (θ). Since resistivity depends on the magnetization direction, AMR can be used for the determination of magnetization direction. We note that although AMR

effect had been applied to reading heads of hard disk drives in the 90's, it has been replaced by giant magnetoresistance (GMR) effect.

In the case of skyrmion, although a direction of macroscopic magnetization of a skyrmion is same as that of conical and ferromagnetic state (i.e. both are parallel to the external magnetic field), the orientation of modulation vector ($\boldsymbol{Q}$) of skyrmion ($\boldsymbol{Q} \perp \boldsymbol{B}$) is different from that of conical ($\boldsymbol{Q} \parallel \boldsymbol{B}$). Hence, skyrmion possibly can be detected by monitoring the orientation of $\boldsymbol{Q}$ vector with respect to the magnetic field direction. Especially, on the basis of the analogy to AMR associated with magnetization, we envisage modulation vector ($\boldsymbol{Q}$) also should give rise to the anisotropic resistance, i.e. difference in magnetoresistance with $\boldsymbol{Q} \perp \boldsymbol{j}$ ($\rho^{\perp \boldsymbol{Q}}$) and $\boldsymbol{Q} \parallel \boldsymbol{j}$ ($\rho^{\parallel \boldsymbol{Q}}$). This AMR associated with $\boldsymbol{Q}$ should be used for determination of direction of $\boldsymbol{Q}$ vector as in the case of the AMR associated with magnetization. To test this working hypothesis, we investigate planar Hall effect in a single crystal of MnSi. In the following, we demonstrate that planar Hall effect shows non-monotonous field dependence, and especially exhibits step-like jump at the phase boundaries between conical and skyrmion phase. The origin of which is assigned to anisotropic magnetoresistance associated with the orientation of magnetic modulation. The planar Hall effect offers new method to electrically detect skyrmion formations.

3.2   Planar Hall effect in MnSi

The MnSi single crystal cut into rectangular shape with a typical size of $2 \times 1 \times 0.3$ mm^3. Planar Hall effect is measured with a setup shown in the inset of Fig. 3.2(b). Magnetic field is applied in the x (current direction)-y (voltage direction) plane. Measured planar Hall resistivity ρ_{yx}^{PHE} reads

$$\rho_{yx}^{\mathrm{PHE}} = \frac{1}{2}(\rho^{\parallel} - \rho^{\perp}) \sin 2\theta, \tag{3.3}$$

where θ is angle between the current and the magnetic field, $\rho^{\parallel}$ and $\rho^{\perp}$ are resistivities with the current parallel and perpendicular to the magnetic field, respectively. We note again that PHE originates from the anisotropic magnetoresistivity, not the conventional Hall effect. To remove voltages from Hall effect and longitudinal resistivity due to misalignments of the sample mounting and the electrodes, we measured the transversal voltage for $\pm B$ and $\pm \theta$ and then symmetrized it against B and antisymmetrized it against θ. Hereafter we define ρ_{yx}^{PHE} as its signal at $\theta = 45°$ unless otherwise noted. The results of PHE shown below were confirmed to be reproducible.

Figure 3.1(a) shows the B-dependence of magnetoresistivity $\rho_{xx}(H)/\rho_{xx}(0)$ at various temperatures for a setup of $H \parallel J \parallel [110]$. The magnetoresistivity (MR) shows an inflection at the critical field B_{c}, where the transition occurs between conical and ferromagnetic structures. In the magnetic field scan crossing the skyrmion phase, a small kink (0.1 % change) in MR is also observed [Fig. 3.1(b)], which is consistent with previous reports [69, 70].

We compare planar Hall signals at the corresponding temperatures measured with $J \parallel [110]$ and B lying in (001) plane in Fig. 3.2. Planar Hall resistivity exhibits clear changes at the magnetic phase boundaries. In particular, ρ_{yx}^{PHE} displays a distinctive stepwise anomaly at the skyrmion phase, which enables us to use ρ_{yx}^{PHE} as a sensitive probe for the skyrmion phase. Here we again note that the step-like behavior of PHE in SkX is not a contribution from THE because the symmetrization against B removes Hall contribution as mentioned above; in fact the magnitude is approximately ten times larger than THE in MnSi [49]. To build further assurance about the correspondence between the skyrmion phase boundaries and ρ_{yx}^{PHE} anomalies, we present development of ρ_{yx}^{PHE} in the T-B region around the skyrmion phase in Fig. 3.3(a). Sharp stepwise structures are confirmed between 27.0–28.5 K. In Fig. 3.3(c), we map the B-derivative of PHE [Fig. 3.3(b)], which emphasizes the abrupt change in PHE, for comparison with the established phase diagram. The abrupt rises and falls of ρ_{yx}^{PHE} coincide with
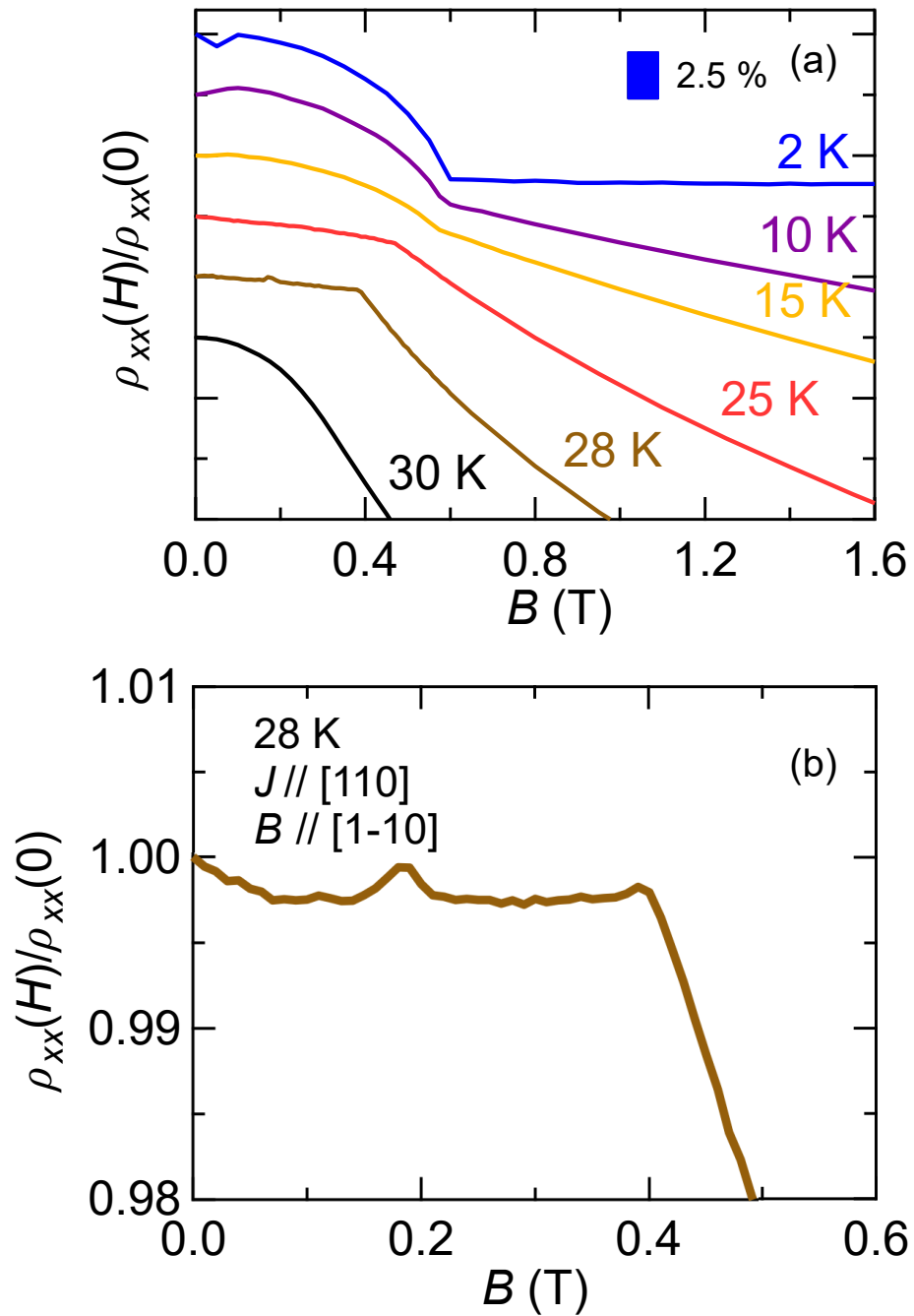
Figure 3.1: (a) Magnetic-field dependence of magnetoresistivity. (b) A magnified image of magnetoresistivity at the skyrmion phase.
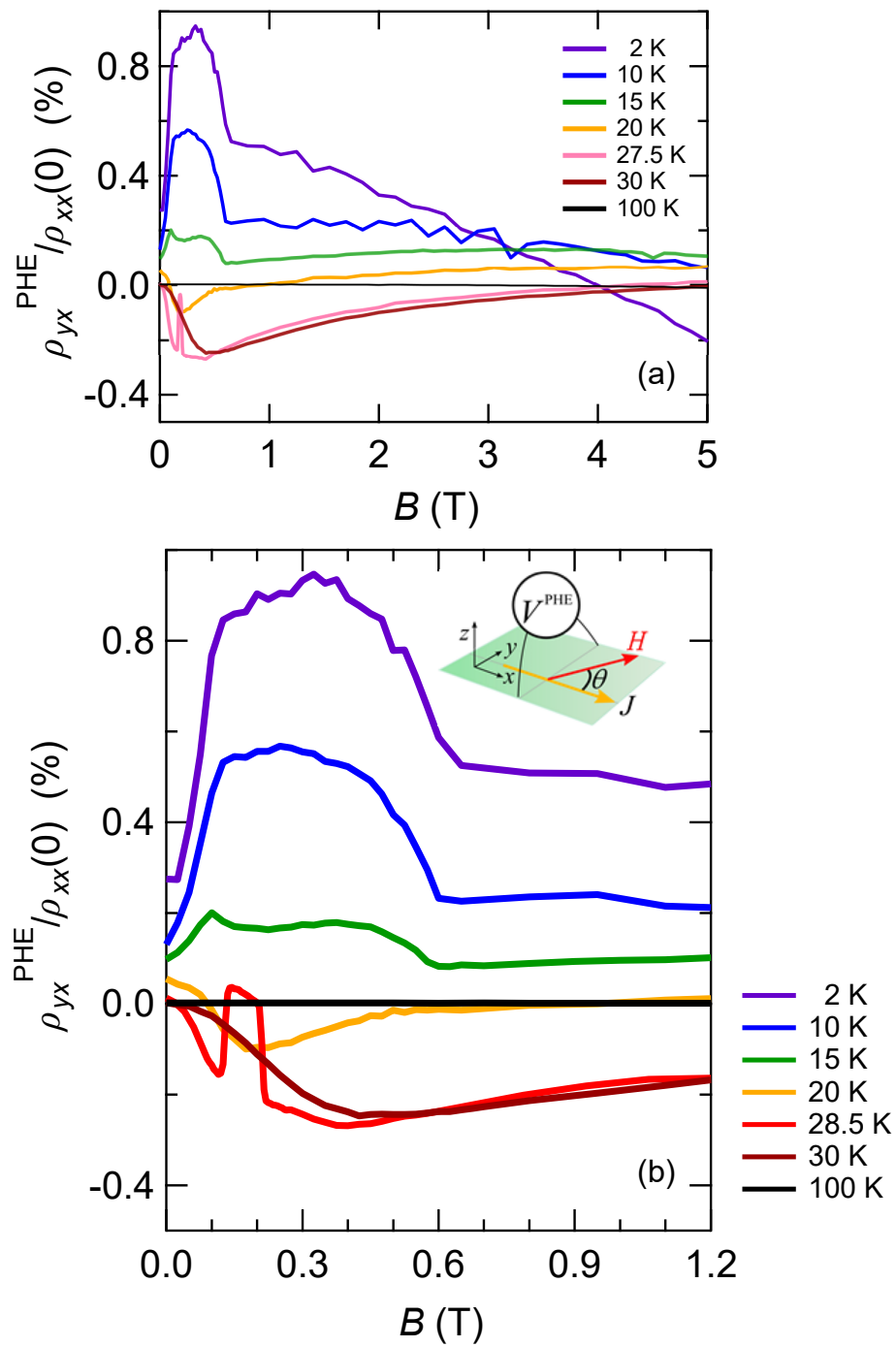
Figure 3.2: (a) Magnetic-field dependence of planar Hall resistivity in the bulk sample. (b) A magnified image of magnetoresistivity in low-magnetic field region. The inset is experimental setup for the measurement of PHE.

the phase boundaries determined by the magnetization measurements in the T-B plane, from which we confirmly assign the PHE anomaly to the skyrmion formation.

3.3 Phenomenological model of the planar Hall effect

The PHE anomaly at the skyrmion phase can be accounted for with a following phenomenological model. Provided that resistivity in a periodically modulated magnetic texture also depends on the orientation of the modulation vector ($\boldsymbol{Q}$), an additional contribution will appear obeying the following relation in a similar way to the conventional PHE with reference to the magnetization: $\rho_{yx}^{\mathrm{PHE},\,\boldsymbol{Q}} = \frac{1}{2}(\rho^{\|\boldsymbol{Q}} - \rho^{\perp\boldsymbol{Q}})\sin 2\theta_{\boldsymbol{Q}}$, where $\rho^{\|\boldsymbol{Q}}$, $\rho^{\perp\boldsymbol{Q}}$, and $\theta_{\boldsymbol{Q}}$ are corresponding parameters measured with reference to $\boldsymbol{Q}$. Upon the transformation to the skyrmion state, $\rho_{yx}^{\mathrm{PHE},\,\boldsymbol{Q}}$ changes its sign due to the sign inversion of $\sin 2\theta_{\boldsymbol{Q}}$ accompanied by the 90°-flop of $\boldsymbol{Q}$, which causes the distinctive anomaly. We note that the magnetic-field dependence of ρ_{yx}^{PHE} with passing through other magnetic phases [Fig. 3.2] can be also explained on the basis of this phenomenological model: While the formation of a multidomain state of the single-$\boldsymbol{Q}$ helical structure nearly cancels out $\rho_{yx}^{\mathrm{PHE},\,\boldsymbol{Q}}$, the AMR feature is restored by B-alignment of the domains of the helical (conical) structure, as the enhanced absolute value of $\rho_{yx}^{\mathrm{PHE},\,\boldsymbol{Q}}$ in the conical phase. When the ferromagnetic state is induced above B_{c}, the contribution from $\rho_{yx}^{\mathrm{PHE},\,\boldsymbol{Q}}$ disappears, leading to the reduction of ρ_{yx}^{PHE} magnitude.

The phenomenological expression is further verified by the angular dependence of PHE. Figure 3.4(a) shows PHE signals normalized by $\sin 2\theta$ at various θ measured with the same setting for Fig. 3.2, i.e., $J \parallel [110]$ and $B \parallel (001)$. Since the spin $\boldsymbol{Q}$ vectors of the conical and skyrmion structures are parallel and perpendicular to B, respectively, each $\rho_{yx}^{\mathrm{PHE},\,\boldsymbol{Q}}$ as well as $\rho_{yx}^{\mathrm{PHE},\,\boldsymbol{M}}$ obeys the $\sin 2\theta$
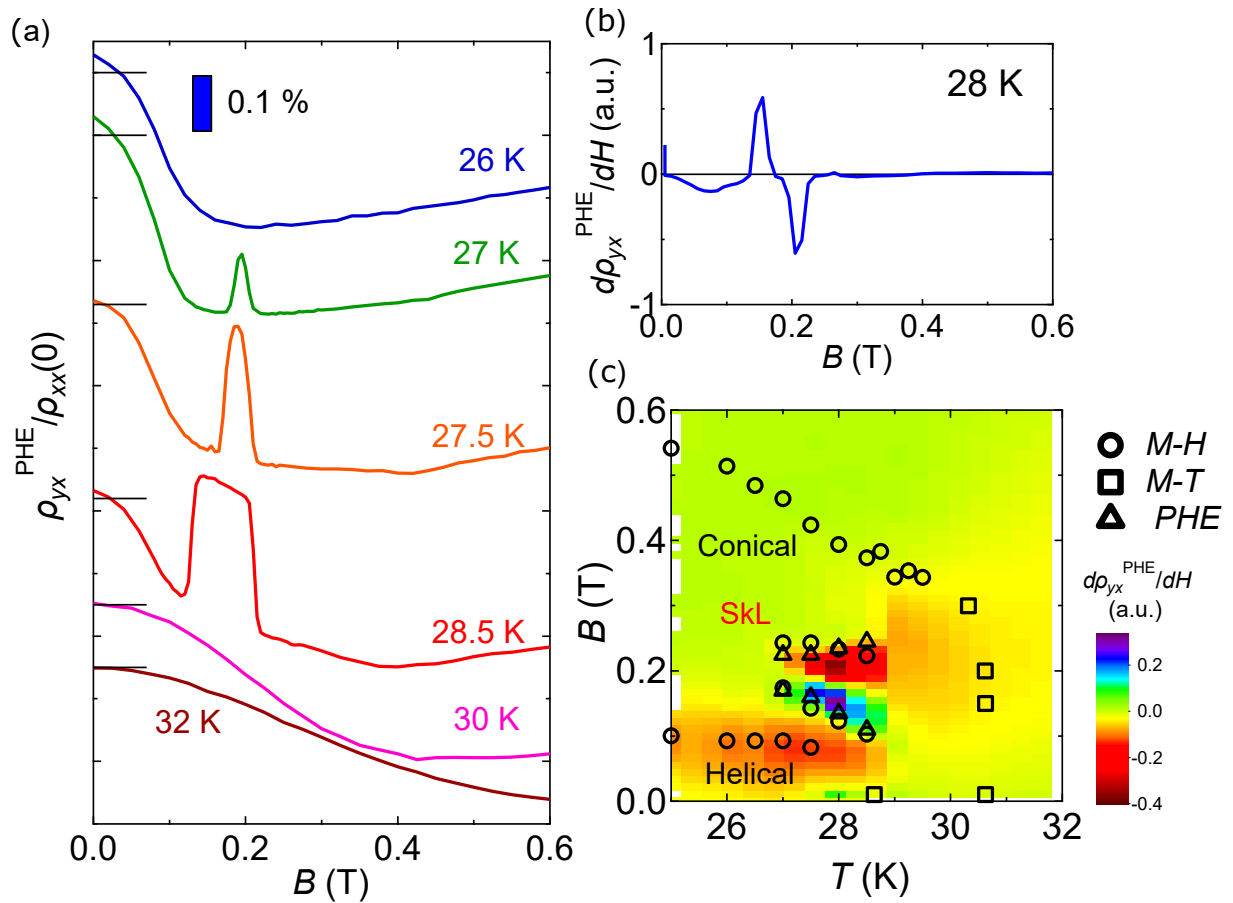
Figure 3.3: (a) Magnetic-field dependence of planar Hall resistivity normalized by longitudinal resistivity at zero field around the skyrmion phase in the bulk sample. (b) The H-derivative of planar Hall resistivity. (c) A contour map of H-derivative of planar Hall resistivity. The solid circles and squares represent phase boundaries determined by magnetization measurements and the open triangles represent the points where the kinks of planar Hall resistivity are observed, corresponding to solid triangles in panel (a).
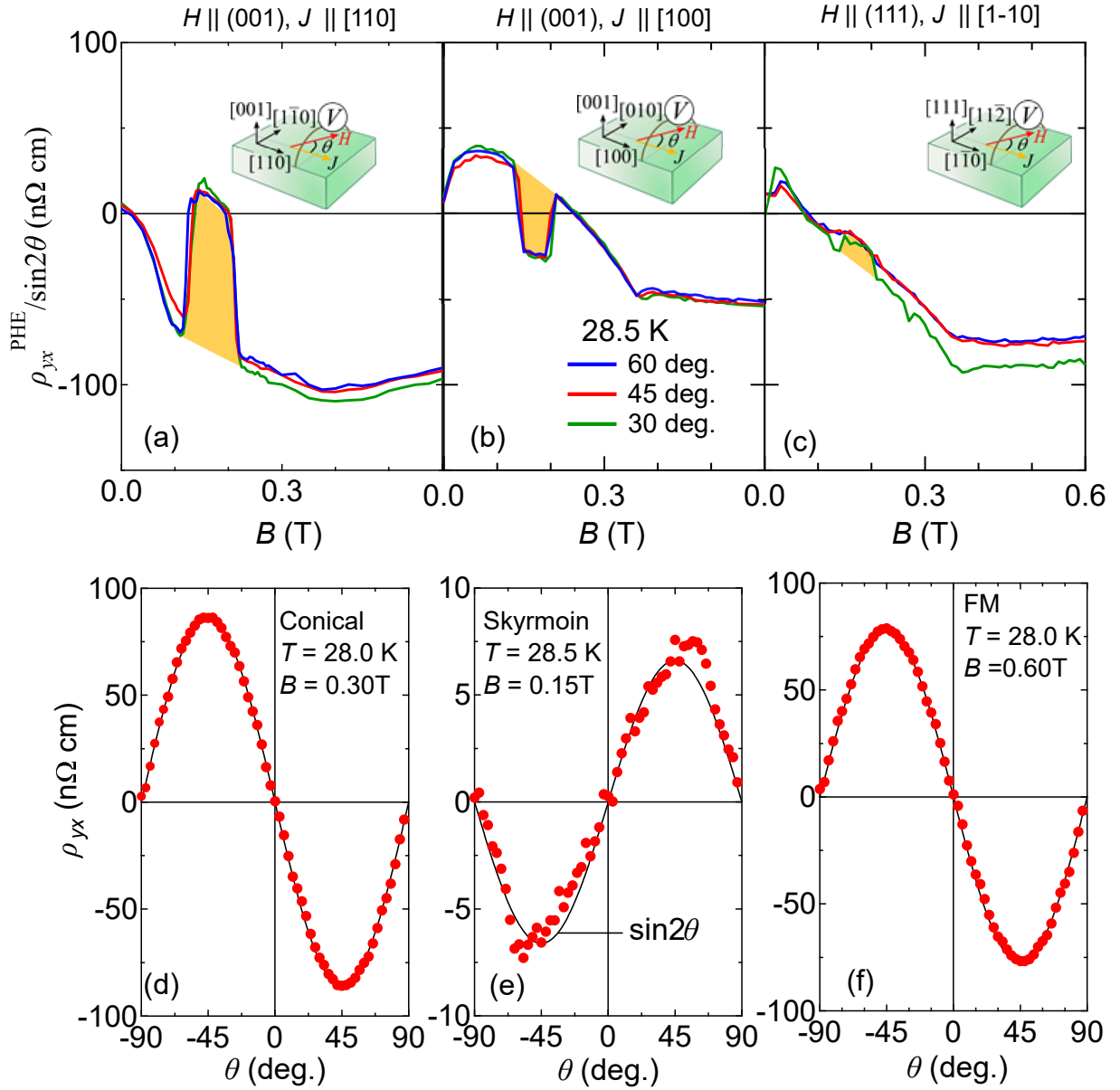
Figure 3.4: Magnetic-field dependence of planar Hall resistivity normalized by $\sin 2\theta$ at various θ with (a) B lying in (001) plane and $J \parallel [110]$, (b) B lying in (001) plane and $J \parallel [100]$, and (c) H lying in (111) plane and $J \parallel [1\bar{1}0]$, respectively. The insets of panels (a)-(c) are experimental setups for the measurement of PHE. Angular (θ) dependence of PHE in (d) conical phase, (e) skyrmion phase, and (f) ferromagetic (FM) phase with B lying in (001) plane and $J \parallel [110]$. Here, θ is angle between the current and the magnetic field. The light blue lines are fits to $\sin 2\theta$.
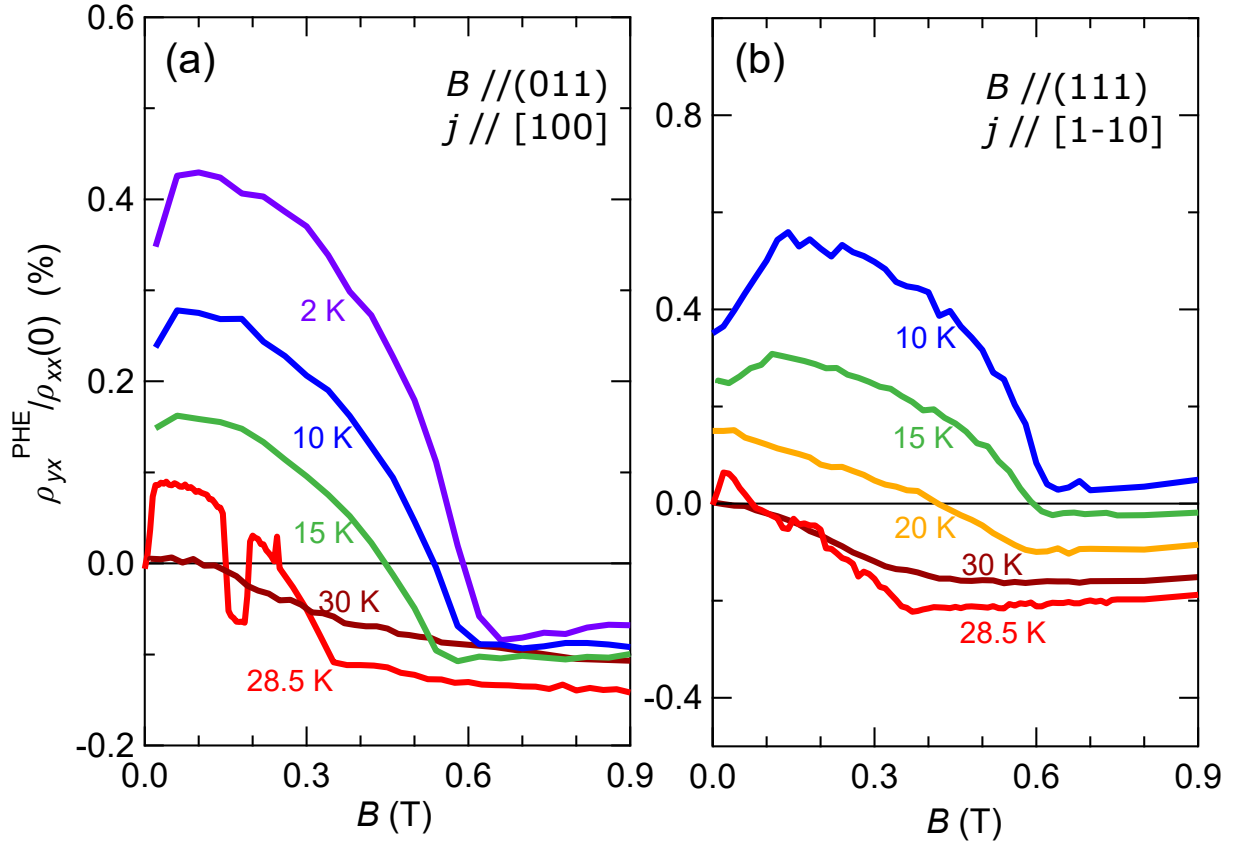
Figure 3.5: (a) Magnetic-field dependence of planar Hall resistivity with (a) H lying in (011) plane and $J \parallel [100]$, and (c) H lying in (111) plane and $J \parallel [1\bar{1}0]$.

dependence. The angles between the electric current and magnetic modulation direction ($\theta_{\boldsymbol{Q}}$) become θ and $\theta + 90°$ in the conical and skyrmion phases, respectively. Consequently, the angle dependencies of PHE remain $\sin 2\theta$ in the both phases: $\sin 2\theta_{\boldsymbol{Q}} = \sin 2\theta$ and $\sin 2\theta_{\boldsymbol{Q}} = \sin 2(\theta + 90°) = -\sin 2\theta$. In fact, the signals of PHE normalized by $\sin 2\theta$ trace the identical curve [3.4(a)]. This is further confirmed by θ dependence of ρ_{yx}^{PHE} [Fig. 3.4(d)-(f)]; planar Hall signals at each magnetic phase clearly follow $\sin 2\theta$ curves.

We measured planar Hall resistivity with different settings of magnetic field and crystallographic orientation. As shown in Fig. 3.5, B-dependencies of ρ_{yx}^{PHE} show different profiles near T_{c}; ρ_{yx}^{PHE} in conical phase is negative and ρ_{yx}^{PHE} in

skyrmion phase is positive in the case of $B \parallel (001)$ [Fig. 3.2] and (111) [Fig. 3.5(b)], whereas ρ_{yx}^{PHE} in conical phase is positive and ρ_{yx}^{PHE} in skyrmion phase is negative in the case of $B \parallel (011)$ [Fig. 3.5(a)]. As shown in Fig. 3.2 and 3.5, the sign of PHE depends on temperature and magnetic field; ρ_{yx}^{PHE} is positive (i.e. $\rho^{\parallel Q} - \rho^{\perp Q} > 0$) both in high-field region and at low temperatures and negative (i.e. $\rho^{\parallel Q} - \rho^{\perp Q} < 0$) near T_{c}. This indicates that there is at least two contributions to AMR related to Q. The contribution with $\rho^{\parallel Q} - \rho^{\perp Q} > 0$ is dominant at low temperatures and high-field region and the contribution with $\rho^{\parallel Q} - \rho^{\perp Q} < 0$ is dominant near T_{c}. Around the skyrmion phase, the dominant contribution depends on the direction of magnetic field with respect to crystalline axes; the contribution with $\rho^{\parallel Q} - \rho^{\perp Q} > 0$ is dominant in the case of $B \parallel (011)$ and $\rho^{\parallel Q} - \rho^{\perp Q} < 0$ in the case of $B \parallel (001)$ and (111). This causes the significant difference in the field profiles of ρ_{yx}^{PHE} at the skrymion phase as observed. We note that the angular dependence of ρ_{yx}^{PHE} is confirmed also in different settings of magnetic field and crystallographic orientation [Fig. 3.4(b) and (c)], although they show much different B-profiles.

3.4 Summary

In this section, we have investigated planar Hall effect in MnSi. Planar Hall effect sensitively detects the 90°-flop of the magnetic modulation associated with the skyrmion formation and destruction, showing the prominent stepwise anomaly in the skyrmion phase. This finding provides the new guiding principle for the establishment of a method to detect skyrmion formation.

Chapter 4

Electrical magnetochiral effect in MnSi

4.1　Introduction

Transport phenomena related to magnetism, including spin fluctuations and chiral magnetism, provide rich physics and functionalities. For example, antiferromagnetic spin fluctuations are involved in formation of Cooper pairs in the high-temperature superconducting cuprates [72], and quantum spin fluctuations break down the Fermi-liquid behaviour [73]. As for the chiral magnetism, real-space Berry phase related to non-coplanar spin textures with finite scalar spin chirality $\chi_{ijk} = \boldsymbol{S} \cdot (\boldsymbol{S}_j \times \boldsymbol{S}_k)$ where $\boldsymbol{S}_n(n = i, j, k)$ are adjacent three spins, can produce emergent magnetic field and hence the topological Hall effect [49, 74]. Despite appreciation of these two concepts, cooperative phenomena from spin fluctuations and spin chirality ($\boldsymbol{C}_{ij} = \boldsymbol{S}_i \times \boldsymbol{S}_j$) have not fully been explored in charge transport phenomena. For their exploration, we focus on directional nonlinear magneto-transport with the resistance proportional to inner product of magnetic field (B) and current, termed electrical magnetochiral effect (eMChE) [75, 76]. The eM-ChE is one kind of directional magnetotransport phenomena being odd against B,

which are generally allowed in noncentrosymmetric systems. Recently, from the viewpoint of not only fundamental physics but also applications, such directional nonlinear transports are investigated, for example, in polar systems such as at interfaces between ferromagnetic metals and nonmagnetic heavy metals [77, 78], at surfaces of magnetic and nonmagnetic topological insulator heterostructures [79], and in polar bulk semiconductor [80]. As for chiral system, however, eMChE in chiral magnet has not been explored, and the relationship between eMChE and chiral magnetism remains elusive.

Spin structures and their dynamics in chiral-lattice magnets bear chiral nature due to antisymmetric exchange interactions, such as Dzyaloshinskii-Moriya (DM) interaction ($\boldsymbol{D} \cdot \boldsymbol{C}_{ij}$); the sign of the DM vector $\boldsymbol{D}$ is intrinsically dependent on the crystalline chirality. As a consequence, the sign of their magnetic chirality, as defined for example by $\boldsymbol{r}_{ij} \cdot \boldsymbol{C}_{ij}$ ($\boldsymbol{r}_{ij}$ being the vector connecting i-th and j-th sites), is macroscopically coherent throughout the crystal, which can make the chirality dependent transport signals macroscopically visible. MnSi of the present focus has the noncentrosymmetric lattice structure, which can exist in two enantiomeric forms: right- and left-handed structures as shown in Fig. 4.1(a). Due to the competition between the ferromagnetic exchange interaction and the DM interaction, there emerge various spin winding structures, whose modulation directions, i.e. magnetic helicity, are determined by handedness of the corresponding lattice structures. Below the magnetic ordering temperature $T_c = 29.5$ K, the long-period (18 nm) helical spin structure [Fig. 4.1(b)] forms [61]. In addition, topological spin objects, skyrmions [Fig. 4.1(c)], condense in triangular-lattice (skyrmion-lattice state) at 0.1 T $\leq B \leq 0.3$ T just below T_c [7]. Above T_c, where the long-range magnetic orders disappear, short-range spin correlations still survive without losing the chiral nature [22, 23, 24, 25]. Strong enhancement of the chiral spin fluctuations around T_c has been theoretically proposed [81] and demonstrated by polarized neutron scattering experiments [22, 23, 24, 25].

In the following we demonstrate that thermal and quantum spin fluctuations
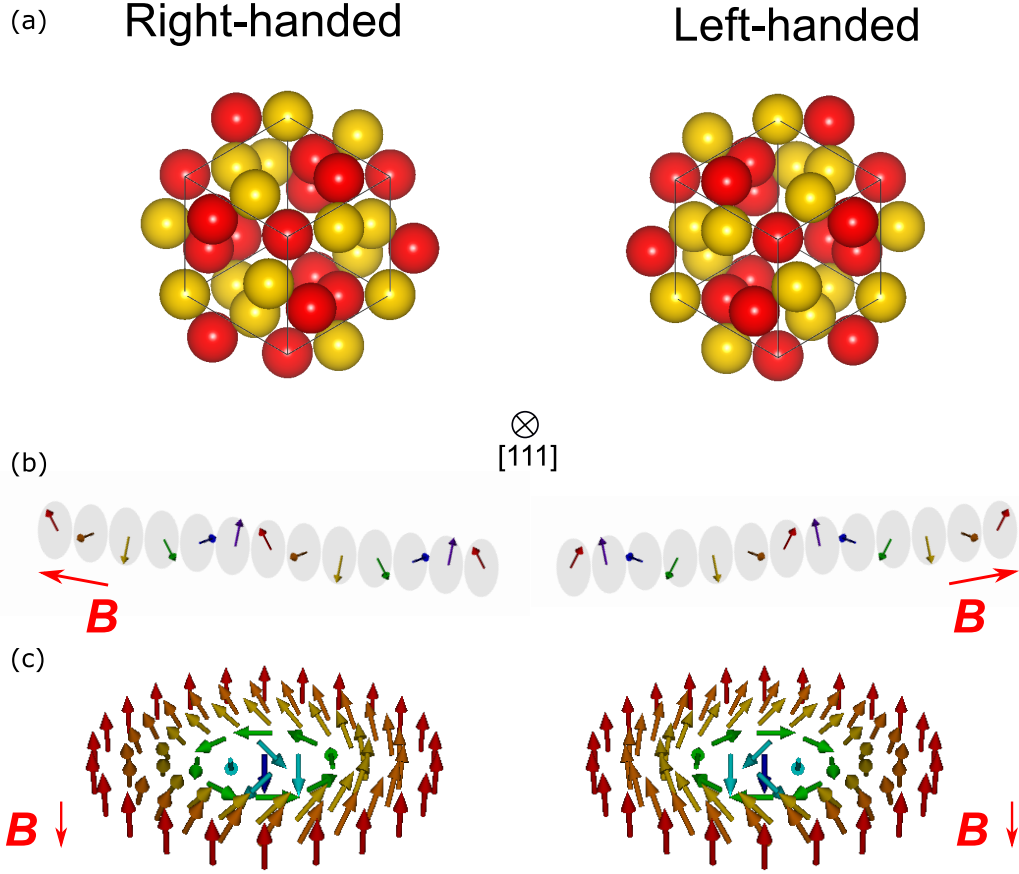
Figure 4.1: Crystal structures of right- and left-handed MnSi viewed from the [111] direction (a) and the corresponding spin structures of helical orders (b) and skyrmions (c). We define the right- and left-handed MnSi as the atomic coordinates (u, u, u), $(1/2+u, 1/2-u, 1/2-u)$, $(1/2-u, -u, 1/2+u)$, $(-u, 1/2+u, 1/2-u)$ with $u_{Mn} = 0.863$, $u_{Si} = 0.155$ and with $u_{Mn} = 0.137$, $u_{Si} = 0.845$, respectively.

endowed with finite vector spin chirality, i.e. chiral spin fluctuations, produce an eMChE. We find that prominent electrical magnetochiral signals emerge at specific temperature-magnetic field-pressure regions: in the paramagnetic phase just above the helical ordering temperature and in the partially-ordered topological spin state at low temperatures and high pressures, where thermal and quantum

spin fluctuations are conspicuous in proximity of classical and quantum phase transitions, respectively.

4.2 Electromagnetic chiral effect in paramagentic phase and partial order phase

4.2.1 Experimental design for detection of eMChE in MnSi

We found that the chiral spin fluctuations play a key role in the eMChE in MnSi. From the viewpoint of symmetry, eMChE can generally appear in chiral systems. Resistivities with current density j parallel and antiparallel to magnetic field B exhibit different values [75, 76]. Resistivity considering eMChE can be described as follows:

$$\boldsymbol{E} = \rho[1 + \gamma^{\mathrm{R/L}}(B)(\boldsymbol{j} \cdot \boldsymbol{B})]\boldsymbol{j}. \tag{4.1}$$

Here, ρ is the linear term of longitudinal resistivity, R and L denote right- and left-handed crystalline chiralities, and $\gamma^{\mathrm{R/L}}(B)$ is the eMChE coefficient being an even function of B. We schematize the current-directional response in MnSi for each experimental configuration in Fig. 4.2(b). Note that Eq. (1) can be transformed to the equivalent form, $\boldsymbol{j} = (1/\rho)[1 - \gamma^{\mathrm{R/L}}(B)(\boldsymbol{E} \cdot \boldsymbol{B})/\rho^2]\boldsymbol{E}$. Under time-reversal operation, the current direction for higher conductance is reversed. Likewise, the higher-conductance direction is opposite for different crystal chiralities; $\gamma^{\mathrm{R}}(B) = -\gamma^{\mathrm{L}}(B)$. Since voltage signals from eMChE are anticipated to be small, enough large current density is required to detect eMChE. In order to increase current density under the limitation of external high-precision current sources, by using focused ion beam (FIB) we fabricated microscale thin plates of MnSi, whose thickness and width are approximately 500 nm and 10 μm, respectively [Fig. 4.2(a)] (see Chapter 2 for the detail).

(a)

(b)
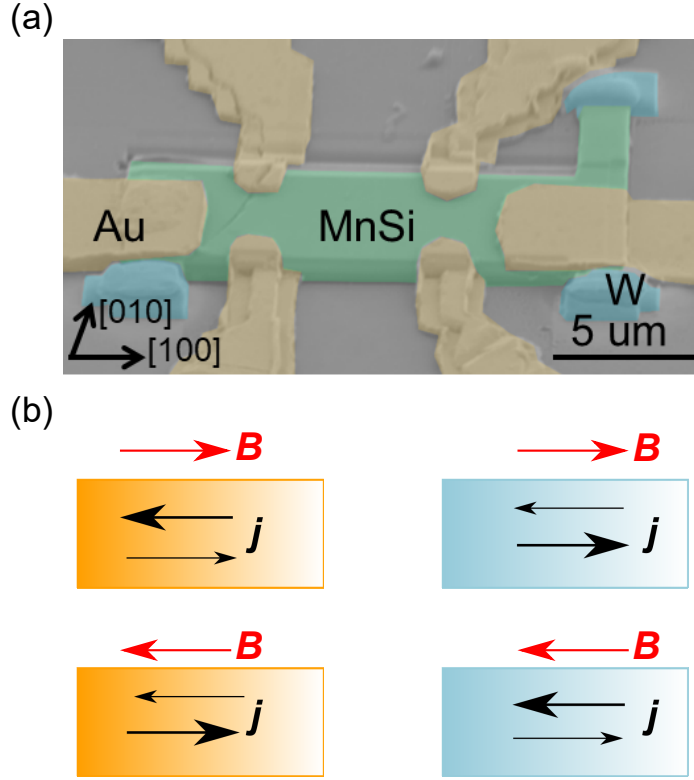
Figure 4.2: (a) A scanning electron microscope image of a MnSi thin plate sample: MnSi crystal (green), gold electrodes (yellow), tungsten for fixing the sample (light blue), and silicon stage (grey). Scale bar, 5 μm. (b) Experimental configurations for measurements of electrical magnetochiral effect and expected dichroic properties of current density. The bold arrows schematically represent paths with the larger current density at a constant electric field along the arrow direction.

4.2.2 Electrical magnetochiral effect at ambient pressure

First, we show typical profiles of eMChE signals observed in MnSi. Since eMChE appears as a nonlinear transport response in proportion to j^2 (Eq. 1), we measured second harmonic resistivity ($\rho^{2\mathrm{f}}$), which is directly connected to eMChE as $\rho^{2f} = \frac{\rho}{2}\gamma^{\mathrm{R/L}}(B)(\boldsymbol{j} \cdot \boldsymbol{B})$. The magnetic field and current were applied parallel to [100] direction unless otherwise noted. Figures 4.3(a) and (b) present $\rho^{2\mathrm{f}}$ of right- and left-handed MnSi at $T = 35$ K with current density $j = 1.0 \times 10^9 \mathrm{Am}^{-2}$ and
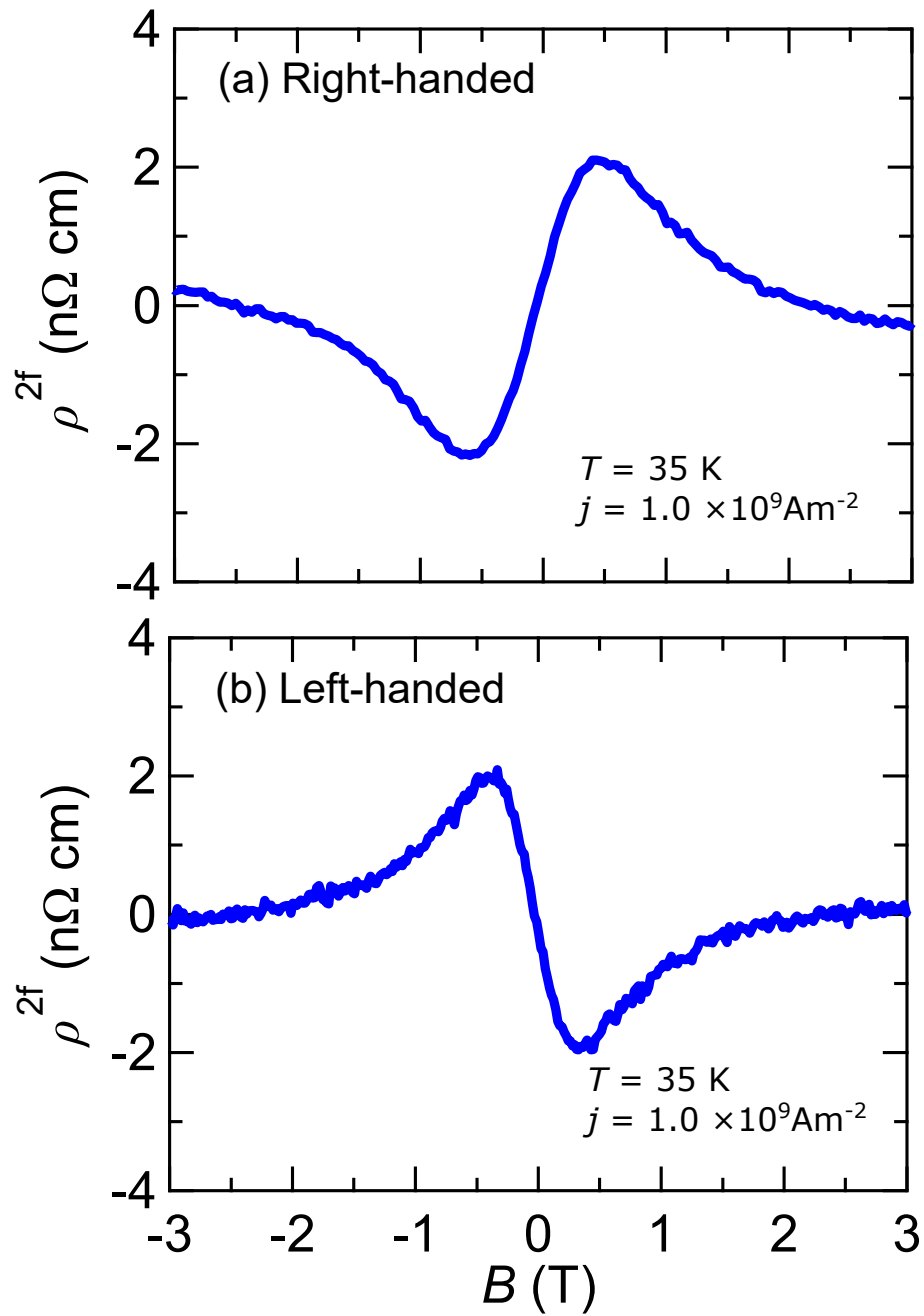
Figure 4.3: Magnetic field dependence of second harmonic resistivity (ρ^{2f}) in right-handed (a) and left-handed MnSi crystals (b).

frequency $f = 30.5$ Hz. The both right- and left-handed crystals were selected from several batches by identifying the handedness in terms of the conversion
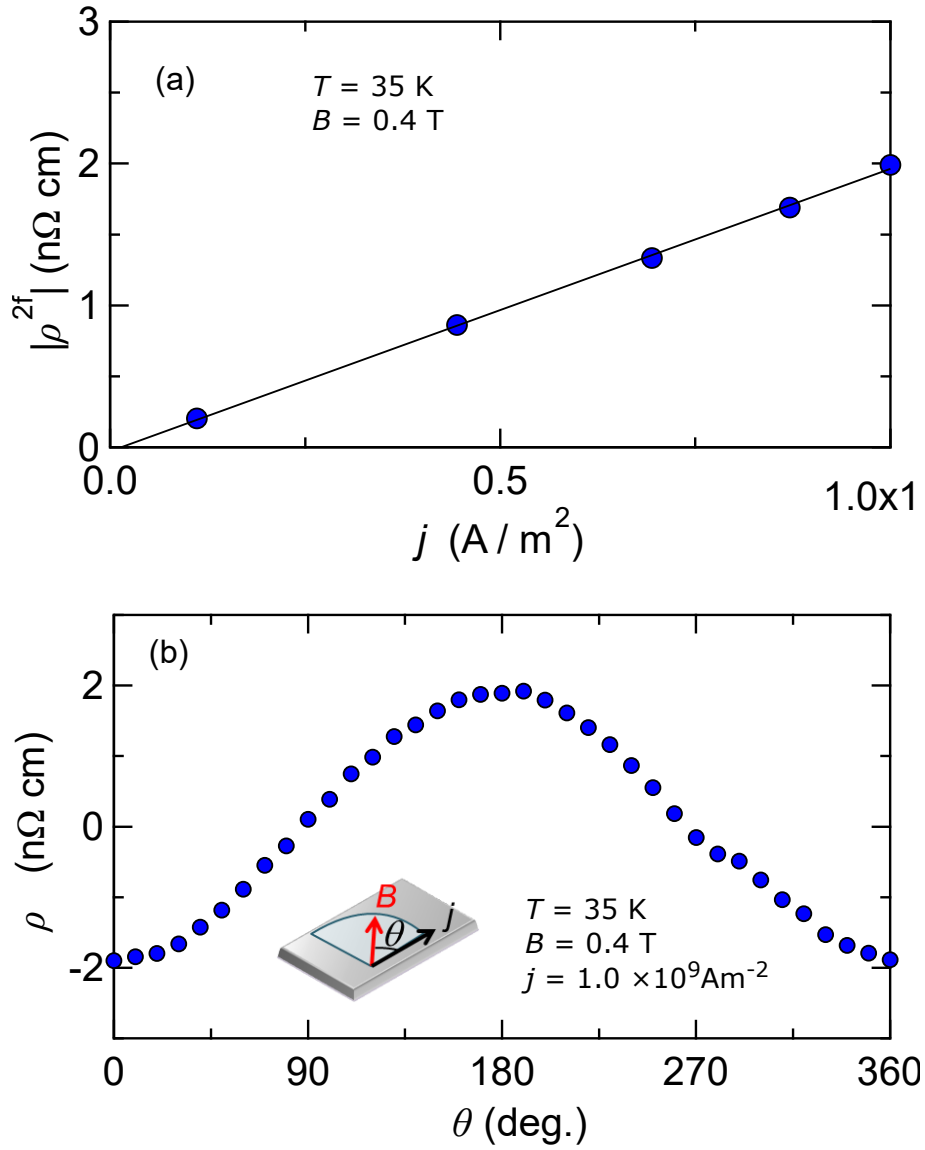
Figure 4.4: Current-density (j) dependence of ρ^{2f} (a) and angle (θ) dependence of second harmonic resistivity ρ^{2f}(b) in left-handed MnSi. Here θ is the angle between current and the magnetic field as shown in the inset of (b). The solid line is fit to $\cos\theta$

beam electron diffraction method (see Chapter 2). In accord with the expected contributions from eMChE, both the field profiles of $\rho^{2\mathrm{f}}$ of the right- and left-handed crystals are antisymmetric against B, exhibiting the opposite sign to each

other. To further confirm that the observed ρ^{2f} signals stem from eMChE, we measured ρ^{2f} at $B = 0.4$ T as functions of current density and relative angle θ between B and j both lying in-plane (Figs. 4.4). Both the j- and θ-dependences obey the expected behaviours from the relation $\rho^{2f} = \frac{\rho}{2}\gamma^{R/L}(B)(j \cdot B)$; ρ^{2f} is proportional to j and $\cos\theta$, respectively. We evaluate $\gamma^{R/L}$ from the fitting of the angular dependence of ρ^{2f} by the equation $\rho^{2f} = \frac{\rho}{2}\gamma^{R/L}(B)(j \cdot B)$ (see also the solid line of Fig. 4.4(b) for the fitting curve). The magnitude of $\gamma^{R/L}(B)$ at $B = 0.4$ T is $1.8 \times 10^{-13}\,\mathrm{m^2 T^{-1} A^{-1}}$, lying within a range of $\gamma^{R/L}(B)$ values reported for non-magnetic chiral materials ($\sim 10^{-8} - 10^{-14}\mathrm{m^2 T^{-1} A^{-1}}$) [76]. We note that the observed second harmonic resistivity does not result from Nernst effect, which is proposed as a possible origin of second harmonic resistivity [77, 79]. While Nernst voltage might be, more or less, generated perpendicular to the magnetic field, the observed angular dependence of ρ^{2f} indicates that the second harmonic voltage is produced parallel to the magnetic field.

Next, we discuss a dominant mechanism of eMChE in MnSi. One mechanism proposed for eMChE in non-magnetic materials is so-called self-field effect [75]. In this mechanism, eMChE is expected to show B-linear dependence. This is however inconsistent with the present observation that ρ^{2f} is suppressed at high magnetic field as presented in Figs. 4.3. Another possible mechanism of eMChE is asymmetric electron scatterings by chiral scatterers [75]. To examine this, we investigate T- and B-dependences of ρ^{2f}. In Fig. 4.5(a), we show a contour mapping of ρ^{2f} in the T-B plane for left-handed MnSi, measured with $j = 7.5 \times 10^8 \mathrm{Am^{-2}}$. We determined the helical-to-ferromagnetic phase boundary and ferromagnetic-to-paramagnetic crossover line from kinks in B-dependence of the planar Hall resistivity (see Chapter 3) and inflection points of $\rho - T$ curve, respectively. Second harmonic resistivity becomes prominent in the paramagnetic region, showing the broad peak profile in the $T - B$ plane just above the phase boundary (helical-to-paramagnetic) and the crossover line (ferromagnetic-to-paramagnetic). In contrast, the signal suddenly declines with entering the long-
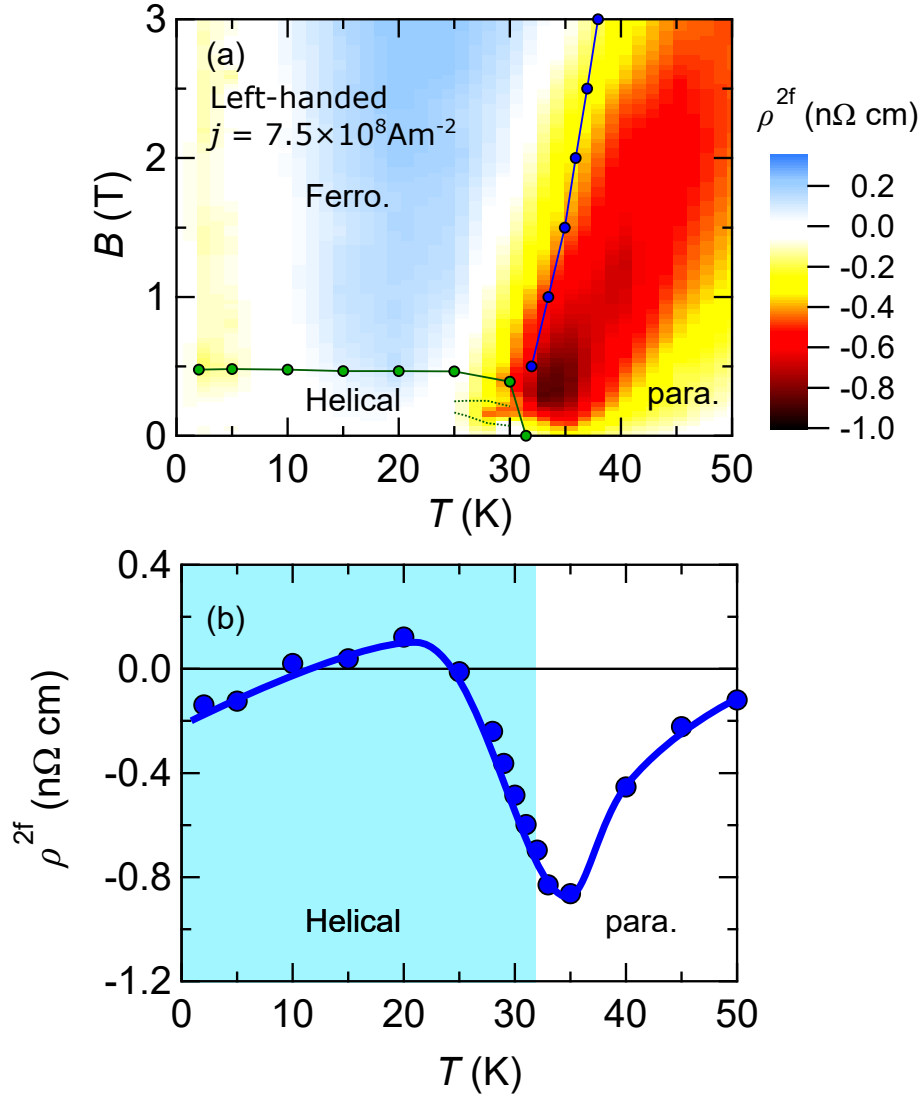
Figure 4.5: (a) Contour mapping of second harmonic resistivity (ρ^{2f}) in left-handed MnSi in T-B plane. The green and blue lines denote the phase boundary enclosing the helical phase and the crossover line between the induced ferromagnetic and paramagnetic phases, respectively. For the ρ^{2f} anomaly around the narrow skyrmion-lattice phase region (denoted by a dotted green line) (b) Temperature dependence of ρ^{2f} at $B = 0.4$ T.

range ordering phases. These behaviours are exemplified by the T-scan of ρ^{2f} at $B = 0.4$ T as shown in Fig. 4.5(b); the magnitude of ρ^{2f} exhibits its maximum near T_c, and shows sharper decrease at the side of helical phase than at the side of paramagnetic phase. Here, we defined the transition temperature for the helical ordering as the temperature where $\rho - T$ curve shows an inflection. We note that ρ^{2f} for right-handed MnSi qualitatively shows similar $T-$ and $B-$dependences to ρ^{2f} for left-handed MnSi, apart from the reversed sign [Fig. 4.6]. The above results indicate that eMChE in MnSi is related to the strongly enhanced chiral spin fluctuations around and immediately above T_c [22, 23, 24, 25], which should induce asymmetric electron scatterings. This scattering process of spin-polarized conduction electrons may share the common microscopic mechanism with asymmetric scatterings of polarized neutrons by chiral spin fluctuations [22, 23, 24, 25].

4.2.3   Electrical magnetochiral effect at the phase boundary of the equilibrium skyrmion-lattice states

Electrical magnetochiral effect is also observed at the phase boundary between the conical and skyrmion-lattice states. To precisely estimate the phase boundary, we employed measurements of planar Hall effect, which was proven in the former study to sensitively detect variations in anisotropic magnetoresistance associated with magnetic transitions, typically showing kinks at phase boundaries between skyrmion-lattice, conical, and induced ferromagnetic states. In Fig. 4.7(b), we present $B-$dependence of planar Hall resistivity (ρ^{PHE}) around T_c, marking the phase boundaries as red and green triangles. The magnetic phase diagram for the thin plate sample is also similar to that for bulk crystal, except for slight expansion of the skyrmion-lattice phase region. Incidentally, the stabilization of skyrmion state are attributed to uniaxial strain, which arises from difference in thermal expansion between the MnSi thin plate and the sample stage made of
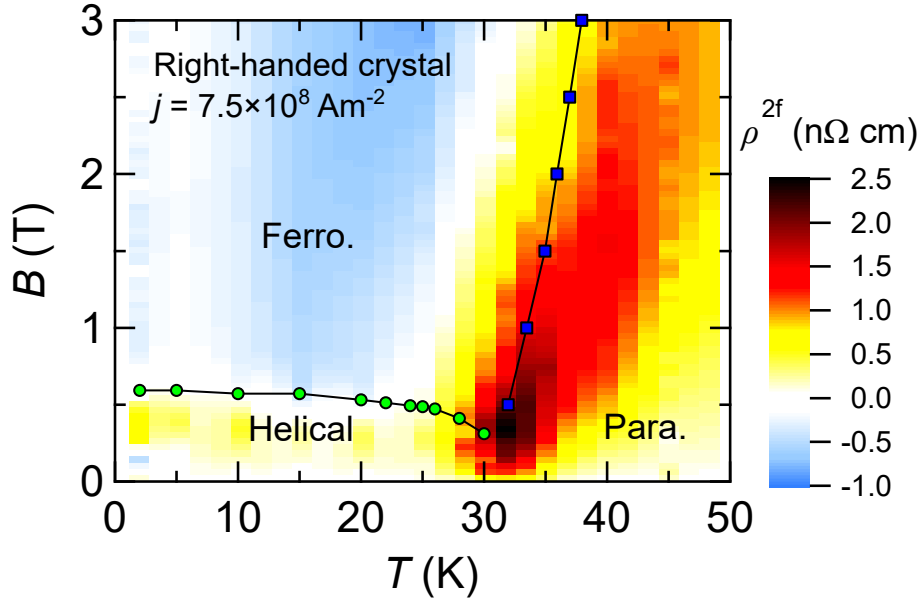
Figure 4.6: Contour mapping of second harmonic resistivity (ρ^{2f}) in right-handed MnSi in $T - B$ plane, measured with $j = 7.5 \times 10^8 \text{Am}^{-2}$. Note that the sign of ρ^{2f} is reversed as compared with the case of left-handed MnSi [Fig. 4.5(a)]. The green and blue lines denote the phase boundary enclosing the helical phase and the crossover line between the induced ferromagnetic and paramagnetic phases, respectively.

Si. A contour mapping of ρ^{2f} in a right-handed MnSi sample measured with $j = 1.0 \times 10^9 \text{A/m}^2$ is presented in Fig. 4.7(a), together with the phase boundaries determined from these ρ^{PHE}-mesurements. This clearly captures the enhanced magnitude of ρ^{2f} at the boundaries of skyrmion-lattice phase, indicating that the asymmetric electron scattering by the chiral spin fluctuations also manifests itself at the phase transition between the skyrmion-lattice and the conical or helical states.
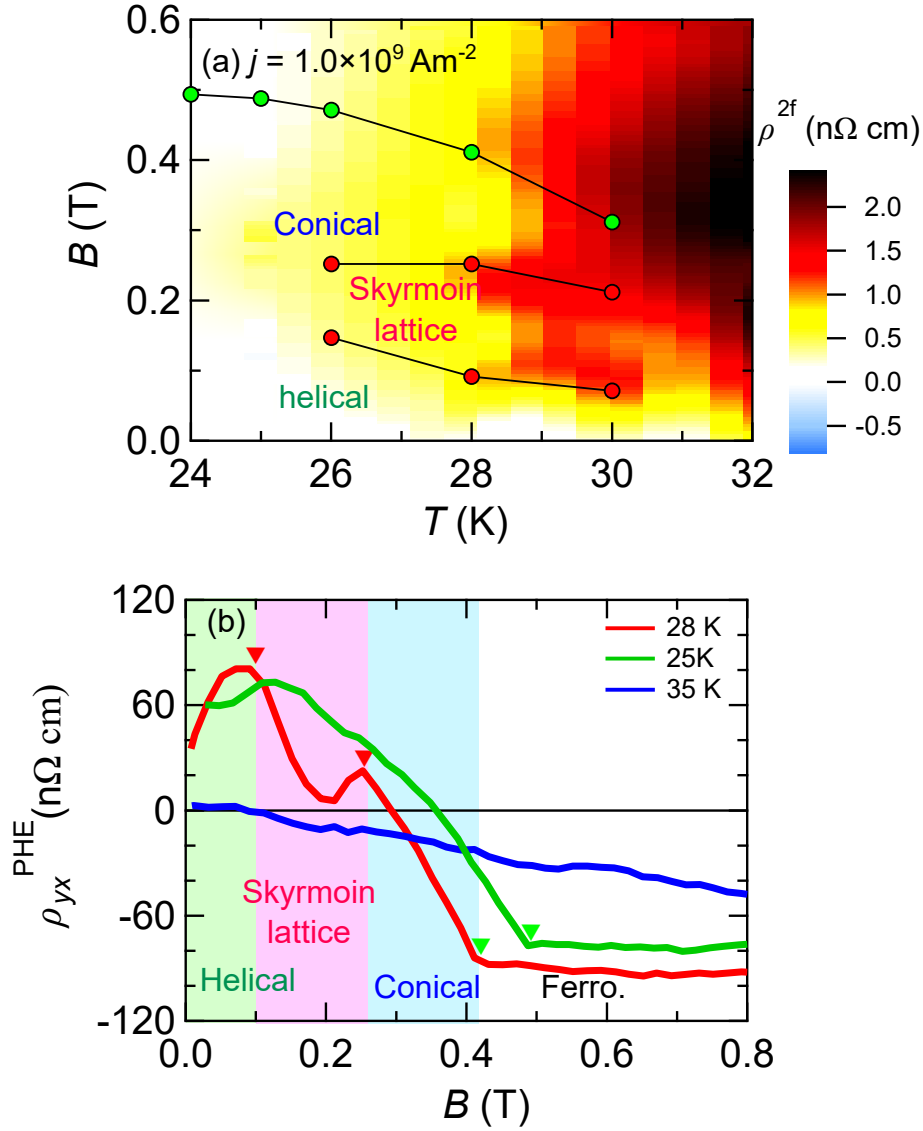
Figure 4.7: (a) Contour mapping of ρ^{2f} of right-handed MnSi around skyrmion phase. (b) Magnetic field dependence of planar Hall resistivity ρ^{PHE} at various temperatures. The green and red triangles represent the phase transitions between the ferromagnetic and conical phases and between the conical and skyrmion-lattice phases, respectively.

4.2.4   Electrical magnetochiral effect in partial order phase

Up to this point, we have revealed that the eMChE in MnSi arises from thermal spin fluctuations enhanced in the vicinity of the helical order as well as of the
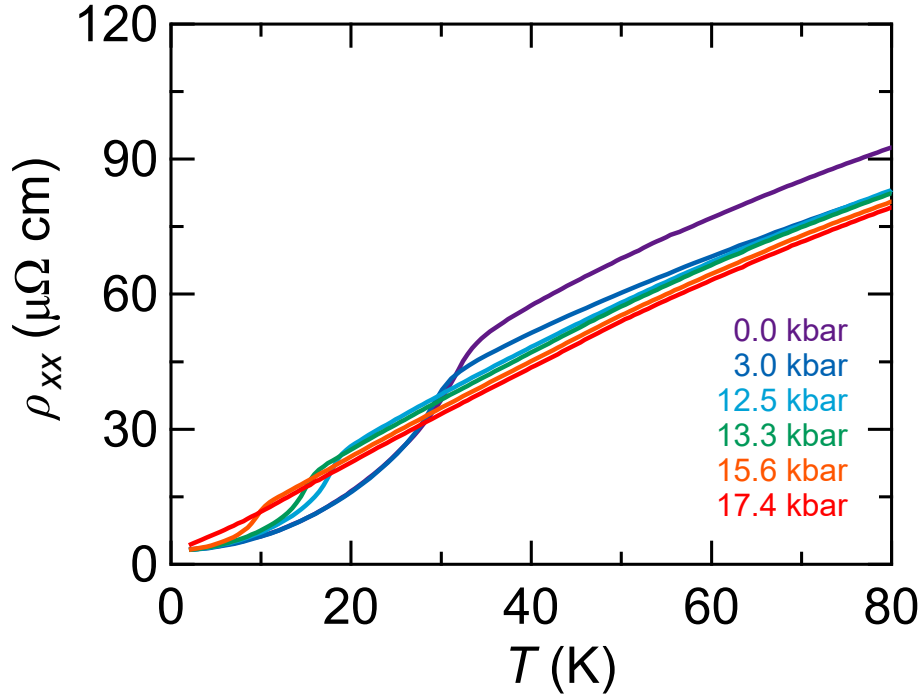
Figure 4.8: Resistivity of thin plate sample at various pressures. The magnetic transition temperatures are determined from the inflection points of $\rho_{xx}-T$ curves. The transition temperatures decrease with increasing applied pressure, resulting in the disappearance of the helical transition above $p = 17.4$ kbar.

skyrmion-lattice phase. In this section, we investigate the possible effect of quantum spin fluctuations on eMChE. In bulk samples of MnSi, the long-range static helical order is suppressed under pressure, and disappears at a pressure of $p = 14.6$ kbar [27, 28, 29], where the quantum phase transition occurs and consequently the quantum spin fluctuations become dominant. Even above the pressure for this quantum phase transition, there exists a dynamical topological magnetic order, which fluctuates on time scales between 10^{-10} s and 10^{-11} s [27, 28, 29] (see also Chapter 1). Since this dynamical magnetic order, called partial order (PO), is promoted by quantum fluctuations, the investigation of eMChE in the PO state will provide us with insight into effects of quantum chiral spin fluctuations.

We determined magnetic phase diagram for MnSi thin plate under pressure
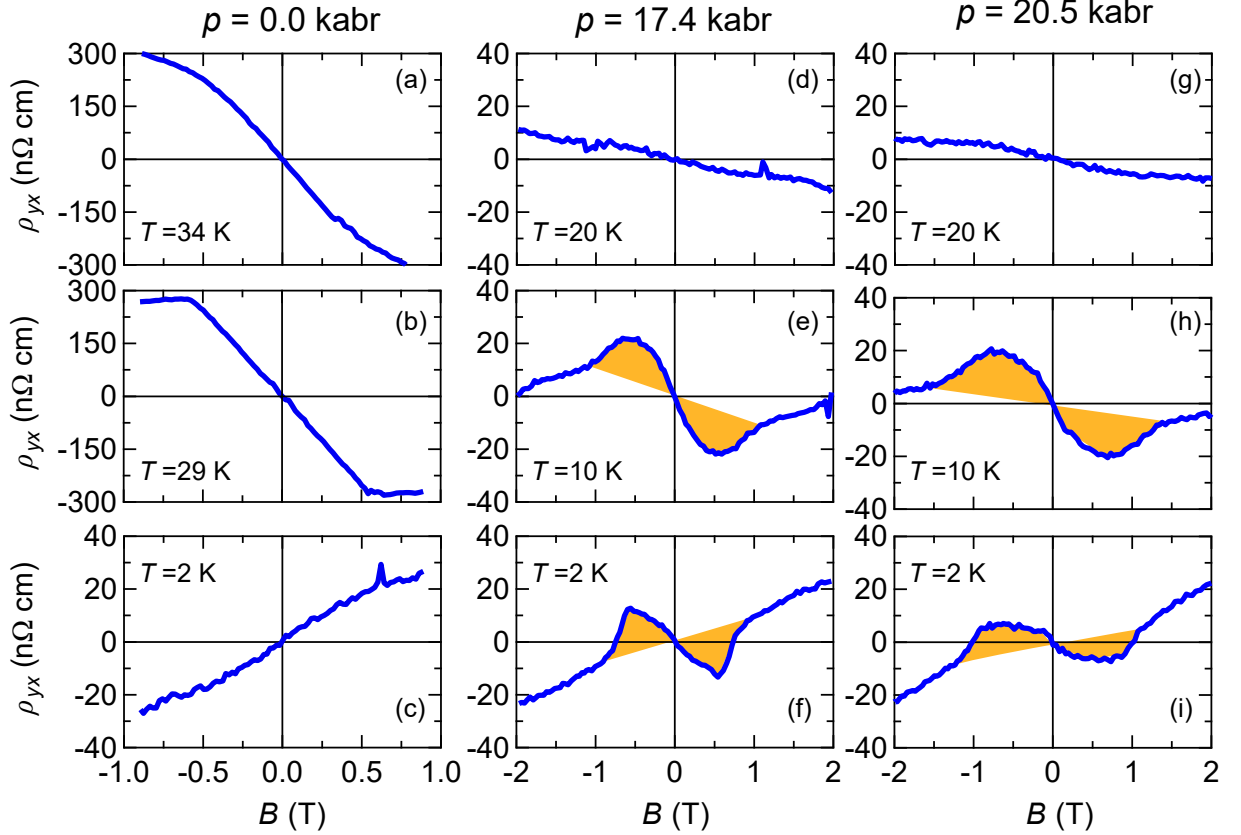
Figure 4.9: (a)-(c), Magnetic-field dependence of Hall resistivity (ρ_{yx}) at various temperatures under $p = 0$ kbar. Magnetic-field dependence of ρ_{yx} at various temperatures under 17.4 kbar (d)-(f) and 20.5 kbar (g)-(i) above the critical pressure (p_c), where long-range helical ordering is suppressed. The orange shadows represent contribution of topological Hall effect. The distinctive topological Hall signals verify the formation of a topological spin structure above p_c in the thin-plate samples of MnSi.

from measurements of ρ_{xx} and ρ_{yx}. In Fig 4.8, we present T-dependence of resistivity of the thin plate sample at various pressures. We assigned inflection points of $\rho_{xx} - T$ curves to the magnetic transition temperatures. The transition temperatures decrease with increasing applied pressure, and above $p = 17.4$ kbar, the helical transition disappears. We also measured the Hall resistivity of MnSi thin

plates and reproduced the similar signals of topological Hall effect as reported in MnSi bulk sample. In Fig. 4.9, we show magnetic-field dependence of Hall resistivity in a MnSi thin plate sample at various temperatures and pressures, in accord with the results reported in Ref. [49]. Hall resistivity at $p = 0$ kbar is dominated by sum of ordinary and anomalous Hall signals [Fig. 4.9(a) — (c)]. In contrast, above p_c, we found the additional contribution of topological Hall effect as indicated by orange shadows [Fig. 4.9 (d) — (i)]. The observation of topological Hall effect identifies the existence of topological spin structure above p_c even in thin plate samples of MnSi. In Fig. 4.10(a), we show $p - T$ phase diagram determined from T-dependence of resistivity and topological Hall resistivity ρ_{yx}^{THE}. The $p - T$ phase diagram is almost identical to that of bulk sample except for increase of the critical pressure $p_c \approx 17$ kbar. The increased p_c is probably due to the tensile strain from the Si sample stage, which compensates the effect of applied hydrostatic pressure.

Figure 4.10(b) shows T-dependence of ρ^{2f} in a left-handed MnSi thin plate sample under $B = 0.4$ T at various pressures, measured with $j = 7.5 \times 10^8 \mathrm{Am}^{-2}$. Contour mappings of ρ^{2f} in $T - B$ plane are presented at several pressures in Figs. **??**. Here, we determined the helical-to-ferromagnetic and the partial order-to-ferromagnetic phase boundaries from the inflection points of $\rho - B$ curves and magnetic field where ρ_{yx}^{THE} disappeared, respectively. For $p \leq p_c \approx 17$kbar, a large magnitude of eMChE signal is detected at the periphery just above T_c, like the case under the ambient pressure (see also Fig. 4.6 for ρ^{2f} at $p = 0$ kbar). For $p \geq p_c \approx 17$ kbar, the eMChE signal shows the maximum magnitude at the lowest measurement temperature within the PO phase, not around the boundaries between the PO and ferromagnetic states nor between the PO and paramagnetic states [Figs. 4.11(c) and (d)]. This feature suggests that the eMChE under $p \geq p_c$ is induced by the quantum spin fluctuations or dynamics of the PO state, which should possess the chiral nature as well.

Lastly, we comment on the existence of eMChE signals with positive (negative)
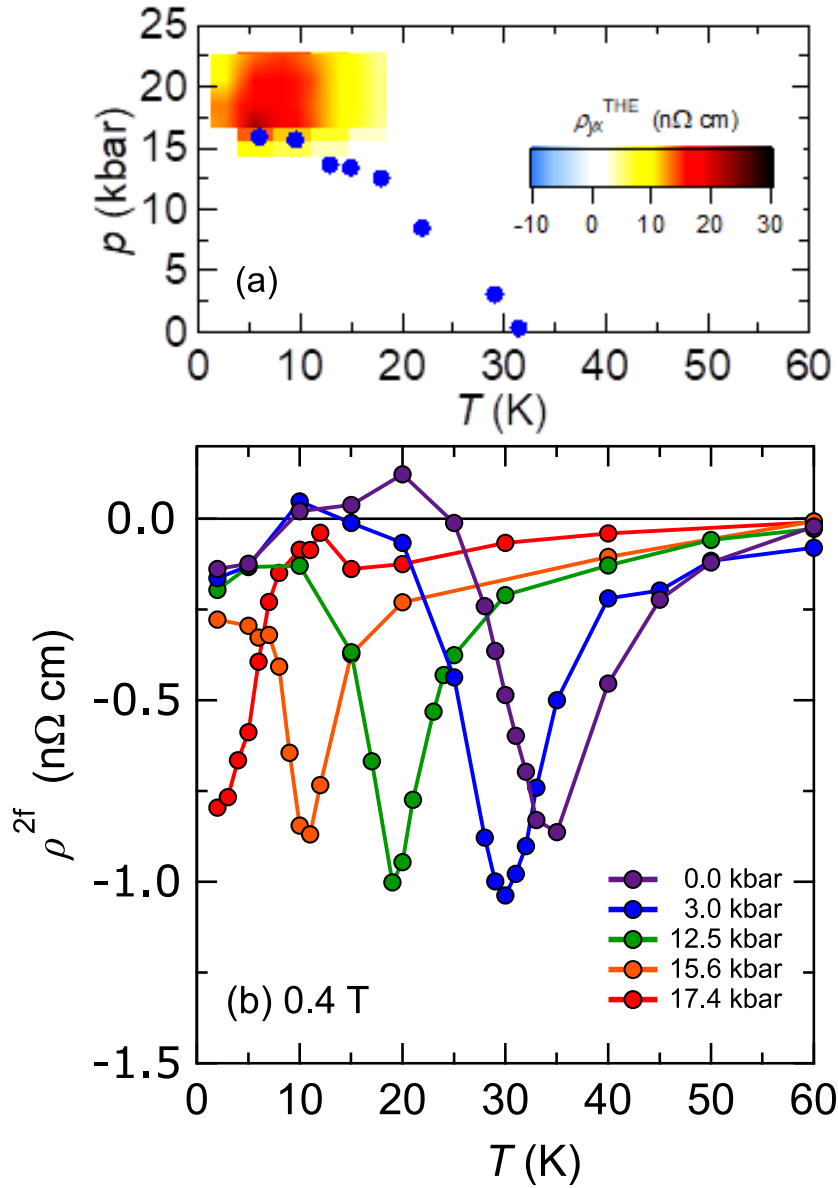
Figure 4.10: (a) Pressure (p) - Temperature (T) phase diagram together with contour mapping of observed topological Hall resistivity ρ_{yx}^{THE} at 0.4 T (see Fig. 4.9). (b) Temperature dependence of second harmonic resistivity (ρ^{2f}) for 0.4 T at various pressures in left-handed MnSi.

sign in the left-handed (right-handed) MnSi, which show the opposite sign to those induced by thermal and quantum spin fluctuations as discussed above. The
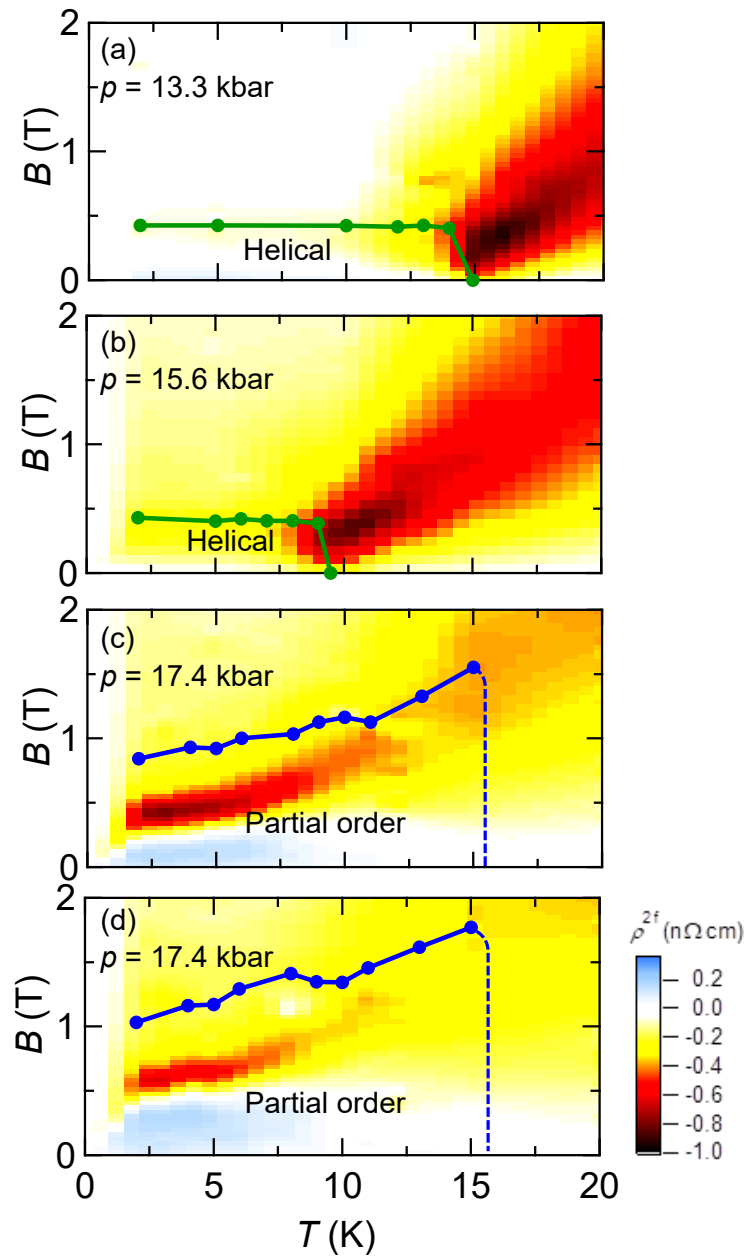
Figure 4.11: (a)-(d), Contour mappings of second harmonic resistivity ρ^{2f} at various pressures in T-B plane in left-handed MnSi. The green lines are the phase boundary between the conical and induced ferromagnetic phases determined from magnetoresistivity measurements, and the blue lines are the phase boundary of the partial order phase determined from topological Hall effect measurements.

positive ρ^{2f} signals in the left-handed crystal are observed at portions of helical and ferromagnetic phases at ambient pressure (blue region of Fig. 4.6) and at low magnetic fields in the PO phase [blue regions of Figs. 4.11(c) and (d)]. Magnetic-field scans in the temperature region with positive ρ^{2f} at ambient pressure ($T =$ 10 - 25 K) indicates that the eMChE signals vary in proportion to magnetization. This implies contribution from another mechanism for eMChE related not to the spin fluctuations but to the static magnetization. Observation of such a different sign of ρ^{2f} in the low-field region of the PO phase may also capture some static or frozen-order nature of the PO state.

4.3 Electrical magnetochiral effect in metastable skyrmion phase

As mentioned above, we observed electrical mangetochiral effect in phase boundary of the equilibrium skyrmion phase. However, because equilibrium skyrmion phase is stable only in a narrow temperature (T)-magnetic field (B) region, the observed signal is a little bit obscure and detailed investigation of the relationship between eMChE and skyrmion strings is challenging. To overcome this problem, we focus on the metastable skyrmions, which is stable in a wider T-B field range.

Both the thermodynamic equilibrium phase diagram and the metastable skyrmion phase are determined by using planar Hall effect, which can sensitively monitor the direction of Q vectors with respect to the magnetic field; the planar Hall resistivity associated with Q vector can be described as

$$\rho_{yx}^{\mathrm{PHE},\,\boldsymbol{Q}} = \frac{1}{2}(\rho^{\|\boldsymbol{Q}} - \rho^{\perp \boldsymbol{Q}}) \sin 2\theta_{\boldsymbol{Q}}. \tag{4.2}$$

Here $\theta_{\boldsymbol{Q}}$ is the relative angle between B and Q (see also Chapter 3 for the detail). Since the direction of Q vectors of the skyrmion phase ($\boldsymbol{Q} \perp \boldsymbol{B}$) and the conical phase ($\boldsymbol{Q} \parallel \boldsymbol{B}$) differ by 90° , the sign of $\rho_{yx}^{\mathrm{PHE},\,\boldsymbol{Q}}$ is abruptly reversed at the phase boundary of skyrmion phase.
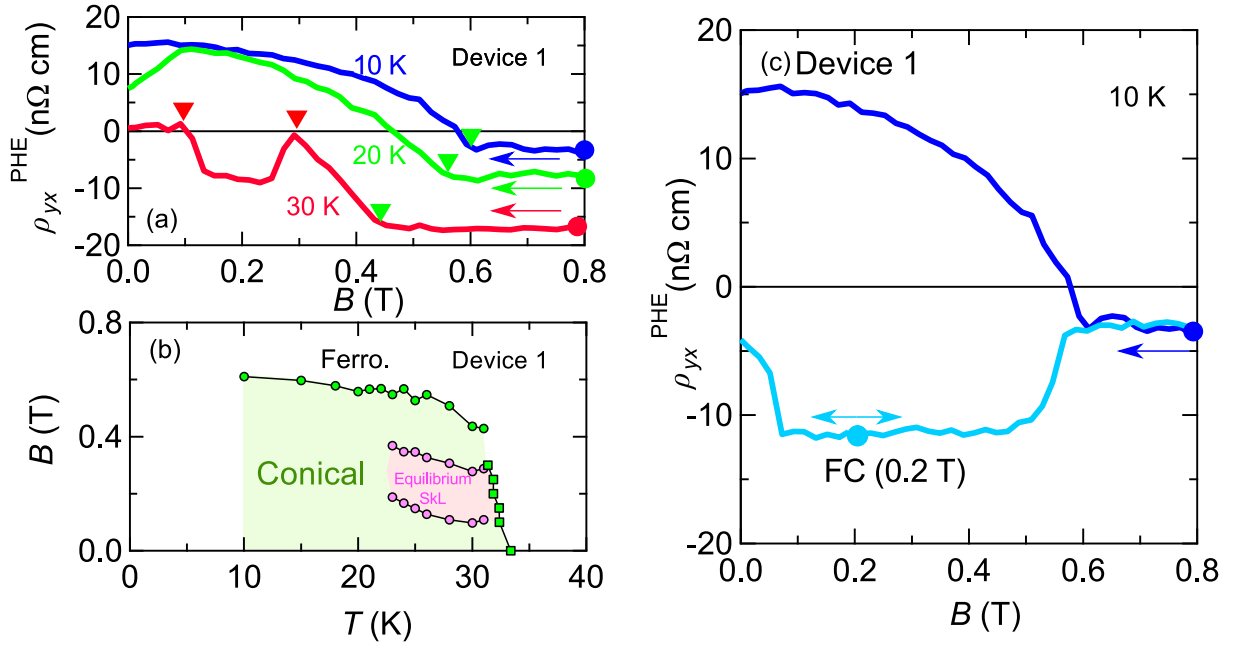
Figure 4.12: (a) Magnetic field dependence of planar Hall resistivity ρ_{yx}^{PHE} measured with decreasing field from 0.8 T at various temperatures. (b) Phase diagram under thermodynamic equilibrium determined by measurement of planar Hall effect. (c) Magnetic field dependence of ρ_{yx}^{PHE} measured with decreasing field from 0.8 T (the dark blue) and measured after field cooling (FC) with 0.2 T (light blue).

Figure 4.12(a) is the planar Hall resistivity (ρ_{yx}^{PHE}) measured with decreasing field from 0.8 T. At 10 K and 20 K, ρ_{yx}^{PHE} shows almost constant negative values at high field region ($0.6 \lesssim B \lesssim 0.8$ T), which we assign to planar Hall effect related magnetization (M). With decreasing magnetic field, ρ_{yx}^{PHE} continually increases below 0.6 T. This positive contribution to ρ_{yx}^{PHE} results from planar Hall effect associated with conical modulation. At $T = 30$ K, ρ_{yx}^{PHE} exhibits abrupt reduction and becomes negative at a narrow magnetic field range ($0.1 < B < 0.3$ T). The abrupt reduction of ρ_{yx}^{PHE} indicates that 90°-flop of Q vector, and hence we assign this magnetic field range to the skyrmion phase. The equilibrium magnetic
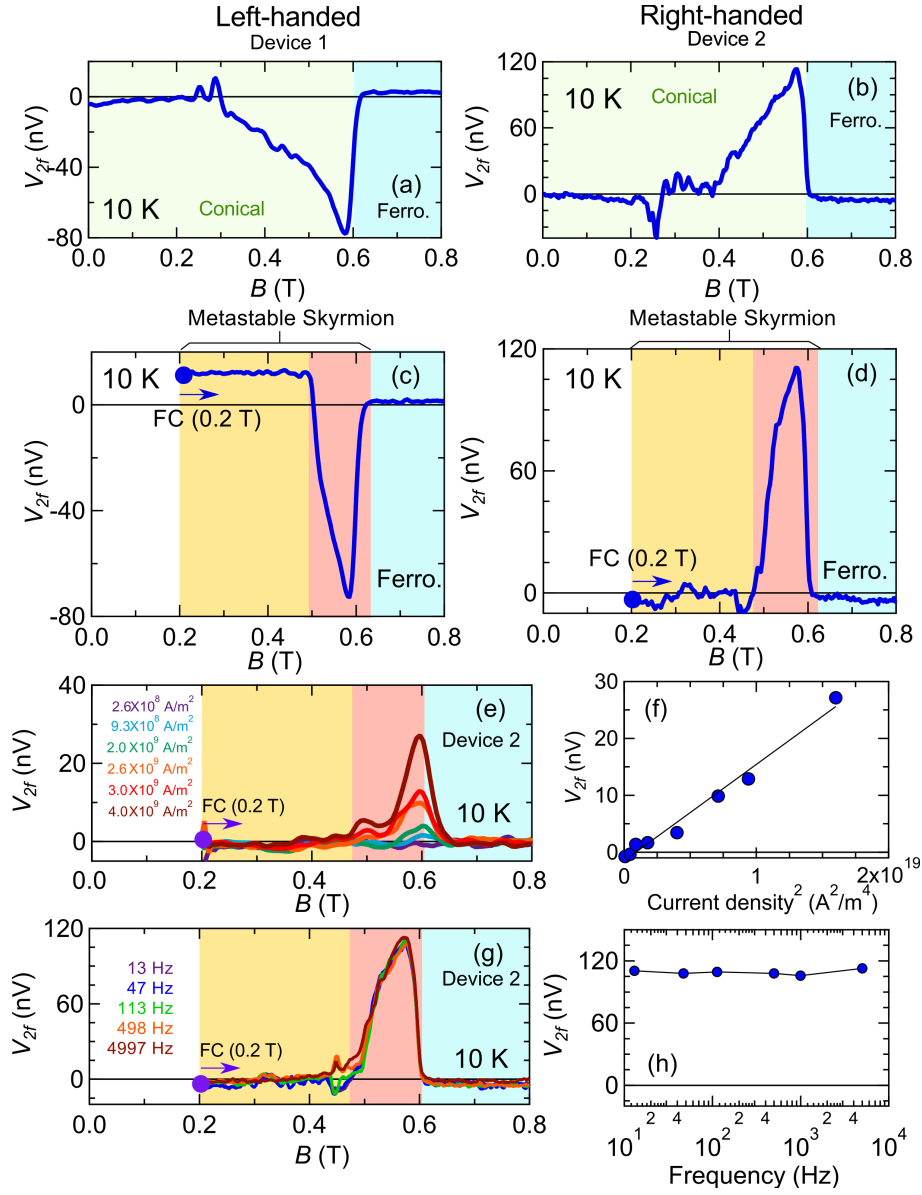
Figure 4.13: Magnetic field (B) dependence of second harmonic voltage (V^{2f}) in conical phase of left-handed MnSi (a) and right-handed MnSi (b). Magnetic field dependence of V^{2f} starting from metastable skyrmion phase created by field cooling with 0.2 T in left-handed MnSi (c) and right-handed MnSi (d). Magnetic field dependence of V^{2f} at various current density (e) and with various frequency of the input current (g). (f) Current density dependence of V^{2f}. (h) Dependence of V^{2f} on frequency of the input current.

phase diagram determined from the measurements of planar Hall effect is shown in 4.12(b). Next, we demonstrate formation of metastable skyrmion in the thin plate sample. Magnetic field dependence of ρ_{yx}^{PHE} after field cooling (FC) passing through the equilibrium skyrmion phase with $B = 0.2$ T and cooling rate of 0.16 K/s is shown in Fig. 4.12(c) (the light blue line). Hereafter, we employ the field cooling condition with $B = 0.2$ T and cooling rate of 0.16 K/s. The sign of ρ_{yx}^{PHE} after FC shows opposite to the sign of ρ_{yx}^{PHE} in the thermodynamically stable conical phase (the dark blue line), indicating direction of $\boldsymbol{Q}$ is perpendicular to the magnetic field direction, and therefore we conclude that metastable skyrmion is created.

In the phase boundary between the thermodynamically stable conical and the ferromagnetic phase, magnetic field-profiles of second harmonics voltage (V^{2f}) of left- and right-handed MnSi exhibit the broad peaks, whose sign is opposite to each other in accord with the expected contribution from electrical magnetochiral effect. [Figs. 4.13(a) and (b)]. This originates from the critically enhanced chiral spin fluctuations at the second-order conical-to-ferromagnetic transition. In Figs. 4.13(c) and (d), we show the magnetic field dependence of V^{2f} of left- and right-handed MnSi in metastable skyrmion phase created by FC. Second harmonic resistivity shows the sharp peaks at high field region of the metastable skyrmion phase ($0.5 < B < 0.6$ T), whereas ρ^{2f} is almost zero at low field region of the metastable skyrmion phase ($0.2 < B < 0.5$ T). The peaks exhibit opposite sign to each other in accord with the expected contribution from eMChE. Figure 4.13(e) is magnetic field dependence of V^{2f} of right-handed MnSi after FC at various current density; the magnitude of V^{2f} continuously increase with increasing current density. As shown in Fig. 4.13(f), the peak value of V^{2f} is proportional to the square of the current density. We also measured the dependence of V^{2f} on the input-current frequency; the field profile of V^{2f} is almost same regardless of the input-current frequency [Fig. 4.13(g) and (h)]. The absence of neither any threshold current density or frequency dependence indicates that the observed
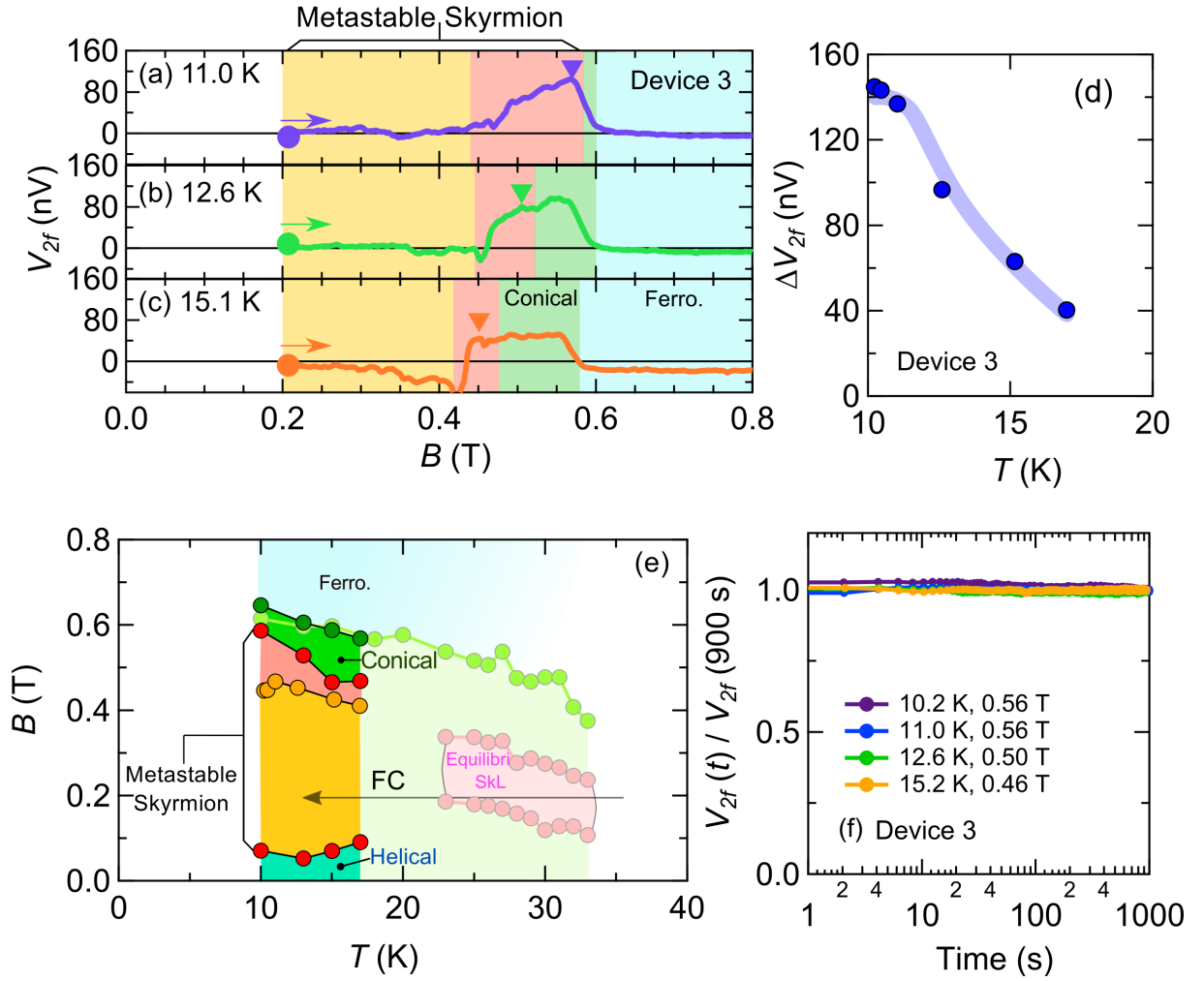
Figure 4.14: (a)-(c) Magnetic field dependence of second harmonic voltage (V^{2f}) after field cooling (FC) passing through the equilibrium skyrmion phase at various temperatures. (d) Temperature dependence of ΔV^{2f}. We defined V^{2f} as the difference between the peak value of V^{2f} and the value of ΔV^{2f} at the ferromagnetic phase. (e) Magnetic phase diagram including metastable skyrmions, constructed by a magnetic field sweep measurement after FC of planar Hall effect and V^{2f}. (d) The time dependence of V^{2f} normalized by the value of V^{2f} at 900 s at various temperatures.

sharp peaks are irrelevant to the current-induced dynamics of skyrmions.

Magnetic field dependence of V^{2f} at various temperatures is shown in Fig. 4.14(a)-(c). Here, two aspects are highlighted: (1) the magnetic field range where nonzero V^{2f} is observed becomes wider with decreasing temperature. (2) the peak value of V^{2f} at the metastable skyrmion phase increases with decreasing temperature [Fig. 4.14(d)]. Note that at 12.6 K and 15.1 K, in addition to the peaks of ρ^{2f} at the metastable skyrmion phase, we also observe the broad peaks of V^{2f} around the conical-to-ferromagnetic phase boundary, which originates from enhancement of chiral spin fluctuations associated with the second-order conical-to-ferromagnetic transition. Figure 4.14 (e) is magnetic phase diagram constructed by a magnetic field sweep measurement after FC of ρ_{yx}^{PHE} and V^{2f}; the metastable skyrmion phase divided into distinct two regimes: (1) low-magnetic-field field region, where V^{2f} is almost zero and (2) high-magnetic-field region, where V^{2f} is nonzero. In fact, the similar metastable skyrmion phase diagram is also observed in FeGe by using LTEM and the high-field region is revealed as amorphous-like metastable skyrmions. Therefore, we assume that the high-magnetic-field region corresponds to amorphous-like form of metastable skyrmions and the disorders of skyrmion strings produces prominent V^{2f} signals.

To examine this scenario, we measured time dependence of the V^{2f}; after FC with 0.2 T passing through the equilibrium skyrmion phase, we increased the magnetic field from 0.2 T to target field with the sweep rate 100 Oe/sec and monitored V^{2f}. Figure 4.14(f) is the time dependence of the peak value of V^{2f} normalized by V^{2f} at 900 s. The second harmonic voltage remains almost constant as a function of a time at least up to 900 s, which indicates that V^{2f} arises from a relatively long-lived state rather a transient process such as an annihilation process of a skyrmion string; in the case of a transient annihilation process of skyrmion string, the signal should decrease as a function of time and finally become zero because the number of skyrmions continuously decreases with time. Hence the above result reasonably supports the scenario that an amorphous-like skyrmion

string stats give rise to the enhancement of V^{2f}.

To further verify the formation of an amorphous-like skyrmion state at the high-field region, we performed a micromagnetic simulation using MuMax3 [82], employing the cuboid with a size of $256 \times 128 \times 256 \, \mathrm{nm}^3$. The following parameters were used: saturation magnetization $M_{\mathrm{sat}} = 1.6 \times 10^5$ A/m, exchange stiffness $A_{\mathrm{ex}} = 1.8 \times 10^{-12}$ J/m, DM interaction $D = 6.7 \times 10^{-4}$ J/m^2, and damping constant $\alpha = 0.1$. The size of the elementary cells was $4 \times 1 \times 1 \, \mathrm{nm}^3$, and magnetic field is applied to the x-axis. We introduced the magnetic anisotropy with easy-axis parallel to the x-axis at randomly selected sites to represent the impurities. Figures 4.15(a)-(d) are the color maps of the x component of magnetization on $y - z$ planes, their fast Fourier transform (FFT) patterns, and position of the core of skyrmion strings at various magnetic field. At $0.14B_{\mathrm{c}}$, the metastable skyrmions form the triangular lattice, and skyrmion strings are almost straight [Fig. 4.15(a)]. At $0.73B_{\mathrm{c}}$, the triangular lattice begins to be distorted, and the six-fold spots of FFT is broadened [Fig. 4.15(b)]. With increasing magnetic field further, the number of skyrmions are decrease, and the six-fold spots of FFT patters almost disappear [Fig. 4.15(c)]. The magnetic field dependence of the peak intensity of the FFT patterns and the skyrmion number N_{Sk} highlights the existence of distinct three regions as a function of the magnetic field [Figs. 4.15(e) and (f)]: (1) the triangular-lattice skyrmion region, where both the peak intensity and the skyrmion number almost are constant, (2) the disordered skyrmion region, where both peak intensity and the skyrmion number are continuously reduced, and (3) the ferromagnetic region. The simulated magnetic field dependence of metastable skyrmions is consistent with experimental observations.

4.4 Summary

In this section, we have investigated the electrical magnetochiral effect (eMChE), which is directional nonlinear magnetotransport effect with the resistance propor-

tional to the inner product of magnetic field and current, and have revealed the close relationship between eMChE and fluctuations and/or disorders of chiral spin structures.

Prominent eMChE signals emerge at specific temperature-magnetic field-pressure regions: in the paramagnetic phase just above the helical ordering temperature and in the partially-ordered topological spin state at low temperatures and high pressures, where thermal and quantum spin fluctuations are conspicuous in proximity of classical and quantum phase transitions, respectively. Electrical magnetochiral effect is also discerned in the phase boundary of the equilibrium skyrmion phase and in the high-magnetic-field region of the metastable skyrmions phase, where skyrmions form amorphous-like state. Our finding sheds light not only on the transport phenomena related to the vector spin chirality but also on the novel functionality in chiral magnets, such as the directional nonlinear magnetotransport.
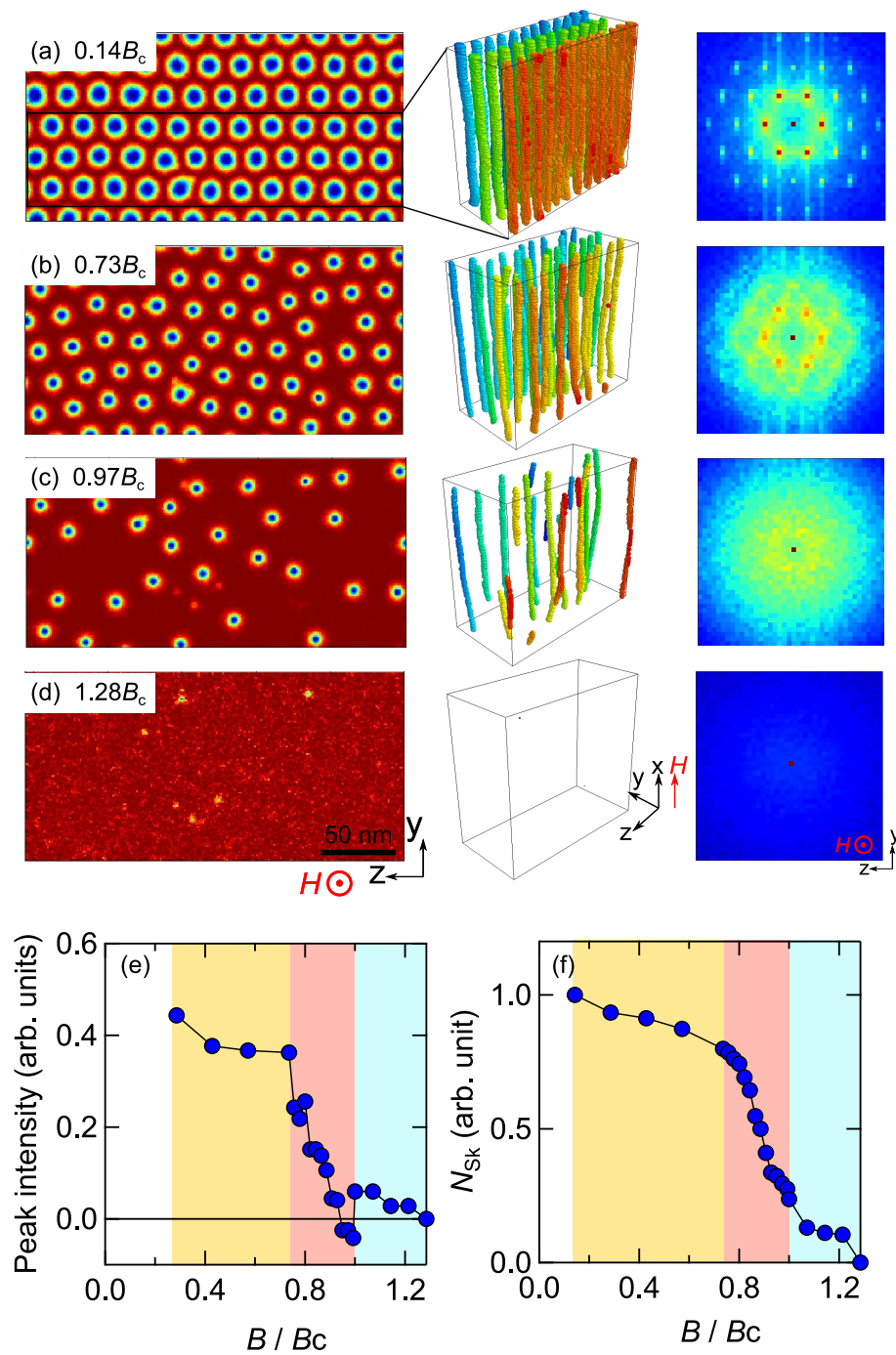
Figure 4.15: (a)-(d) Color maps of the x component of magnetization on $y - z$ planes, their fast Fourier transform (FFT) patterns, and position of the core of skyrmion strings at various magnetic field. B_c is determined from a kink in the magnetic field dependence of magnetization. Magnetic field dependence of peak intensity of FFT patterns (e) and the skyrmion number (N_{Sk}).

Chapter 5

Current-induced dynamics of skyrmion strings investigated by nonreciprocal Hall effect

5.1   Introduction

Topologically stable defects cannot be unwound by continuous transformation or weak perturbations [83]. As for string-like topological defects, the topological stability brings about the degree of freedom of bends; for example, when a part of a string is pulled, string does not tear up but flexibly deforms. Because of this nature the string-like topological defects exhibit rich forms and dynamical properties. One of the most prototypical examples is vortex lines in type-II superconductors (SC); aggregate of vortex lines forms various state such as glass state and liquid state, mainly depending on relative strength of pinning force, thermal fluctuations and energy cost to bend vortex lines [84]. Moreover, deformations are also dynamically induced by external forces such as electrical current[85].

Recently a string-like topological defect has been found in spin system, that is skyrmion strings [7, 8, 13, 4]. Skyrmion string is a vortex-like topological spin
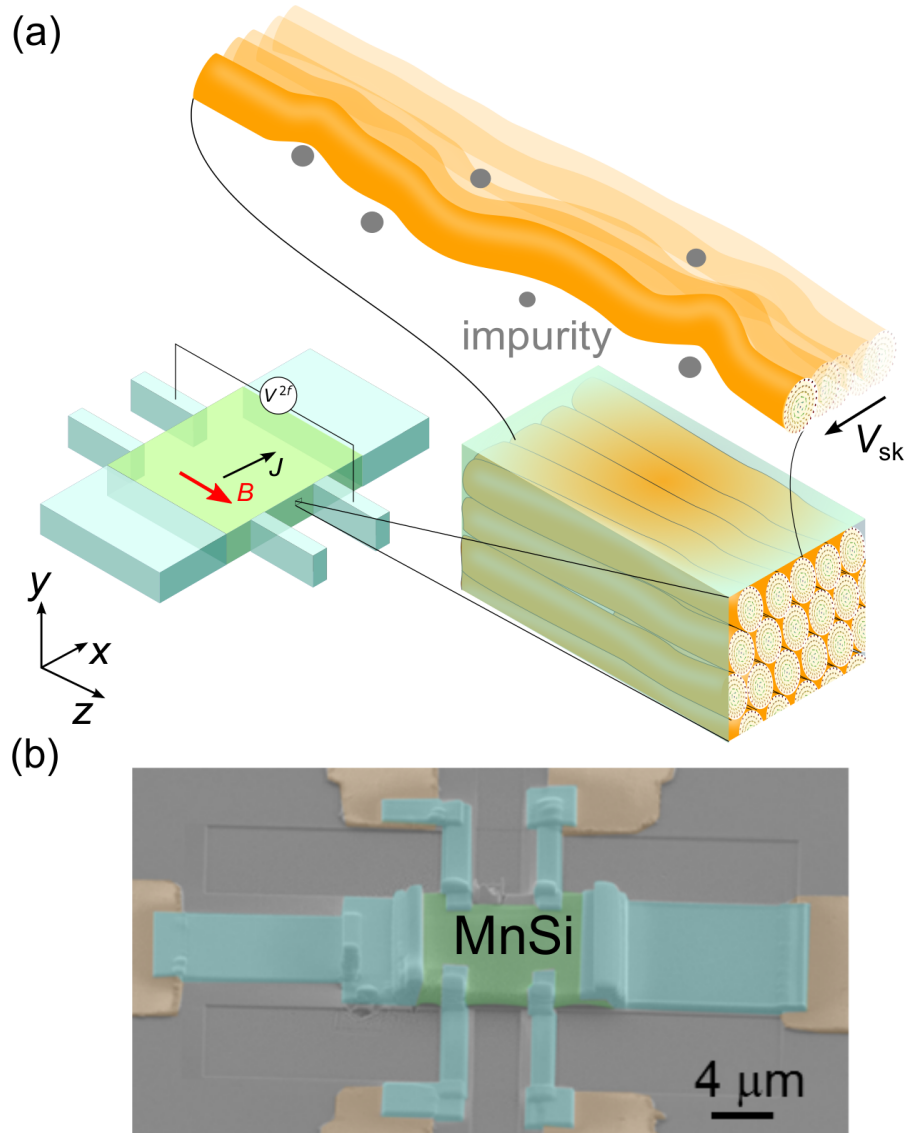
Figure 5.1: (a) schematic picture of translationally moving skyrmion strings and the experimental setup for second- harmonic Hall measurement. (b) A scanning electron microscope image of a MnSi thin plate sample: MnSi crystal (green), gold electrodes (yellow), tungsten (light blue) for fixing the MnSi and connecting the gold electrodes to MnSi, and a silicon stage (grey).

structure of 5-200 nm in diameter and 10-10,000 nm in length along the external magnetic field direction, emerging in non-centrosymmetric magnets due to competition between ferromagnetic exchange interaction and Dzyaloshinskii-Moriya (DM) interaction. The topological nature of skyrmion, which is characterized by a topological number of -1, not only guarantees its stability against weak perturbations but also leads unique transport phenomena related to the real-space Berry phase, which acts as emergent electromagnetic field to conduction electrons [4, 86], such as topological Hall effect [49], and low-current drive [51] and consequent emergent electric field in analogy to the electromagnetic induction [52]. Especially, the latter stimulates researches on the skyrmion-based memory device application [5]. However, in previous researches on the current-induced translational motion, skyrmion strings are treated as two-dimensional objects or straight cylinders, and the degree of freedom of the bend of skyrmion strings (i.e. flexibility) has been ignored. In reality, a skyrmion string possesses flexible nature as in the case of the vortex line because of its topological nature. Hence, especially under translational motion in the presence of random impurities, skyrmions string should dynamically bend to avoid impurities [Fig. 5.1 (a)]. This assumption is based on the simulation in a two-dimensional system [58], according to which translationally moving skyrmion is deformed so as to avoid impurities; it is natural to extend the concept of the deformation to a skyrmion string in three-dimensional system. We note that current-induced dynamics of skyrmion strings in three-dimensional system also have been simulated to find flexible deformation of the strings [87]. Here, we investigate current-induced deformation dynamics of skyrmion strings arising from the flexibility. To this end, we focus on the nonreciprocal and current-nonlinear Hall effect, which is empirically known as a sensitive probe for current-induced spin dynamics in non-centrosymmetric systems [88], typically for the skyrmion lattice (SkL) phase of B20-type MnSi, in which the skyrmion strings form a triangular lattice as in the Abrikosov lattice of SC vortex lines [84]. In the following, we demonstrate that skyrmion strings

asymmetrically deformed due to both the flexible nature and the DM interaction, consequently giving rise to nonreciprocal nonlinear Hall response originating from emergent electromagnetic field.

5.2 Second-harmonic Hall effect

B20-type MnSi has the non-centrosymmetric lattice structure, which can exist in two enantiomeric forms: right- and left-handed structures. From the viewpoint of symmetry, nonreciprocal nonlinear Hall electric field (E_z) in MnSi can be described as follows:

$$E_z = \alpha(j_x, B_z)j_x \tag{5.1}$$

Here, j_x, and B_z are the x component of current density, and the z component of magnetic field, respectively, and the nonlinear Hall coefficient $\alpha(j_x, B_z)$ is pseudo-scalar which is an odd function of j_x and B_z [Fig. 5.1(a)]. Hence, a direction of the nonlinear Hall electric field is independent of current direction, being parallel or anti-parallel to B_z depending on the crystal chirality. We fabricated microscale MnSi thin plates by using focused ion beam (FIB) [Fig. 5.1(b)] to increase current density under the limitation of external high-precision current sources. The crystal chirality was determined by using convergent beam electron diffraction. We determined the magnetic phase diagram for MnSi thin plate from the measurements of longitudinal resistivity (ρ_{xx}) and planar Hall resistivity (ρ^{PHE}), both of which are widely employed as the sensitive probes of magnetic transitions in MnSi. The helical-ordering temperature (T_{c}) at the zero magnetic field is determined as the temperature where the $\rho_{xx} - T$ curve exhibits an inflection [Fig. 5.2(a)]. The helical-to-conical, helical/conical-to-skyrmion, and conical-to-ferromagnetic transitions are determined from the kinks in B-dependence of ρ^{PHE} [Figs. 5.2(b)-(e)].

To detect nonlinear Hall signal, we performed second-harmonic measurement; low-frequency sine-wave AC current was input and real part and imaginary part of second-harmonic complex resistivity ($\text{Re}\rho_{zx}^{2f}$ and $\text{Im}\rho_{zx}^{2f}$) were measured, which
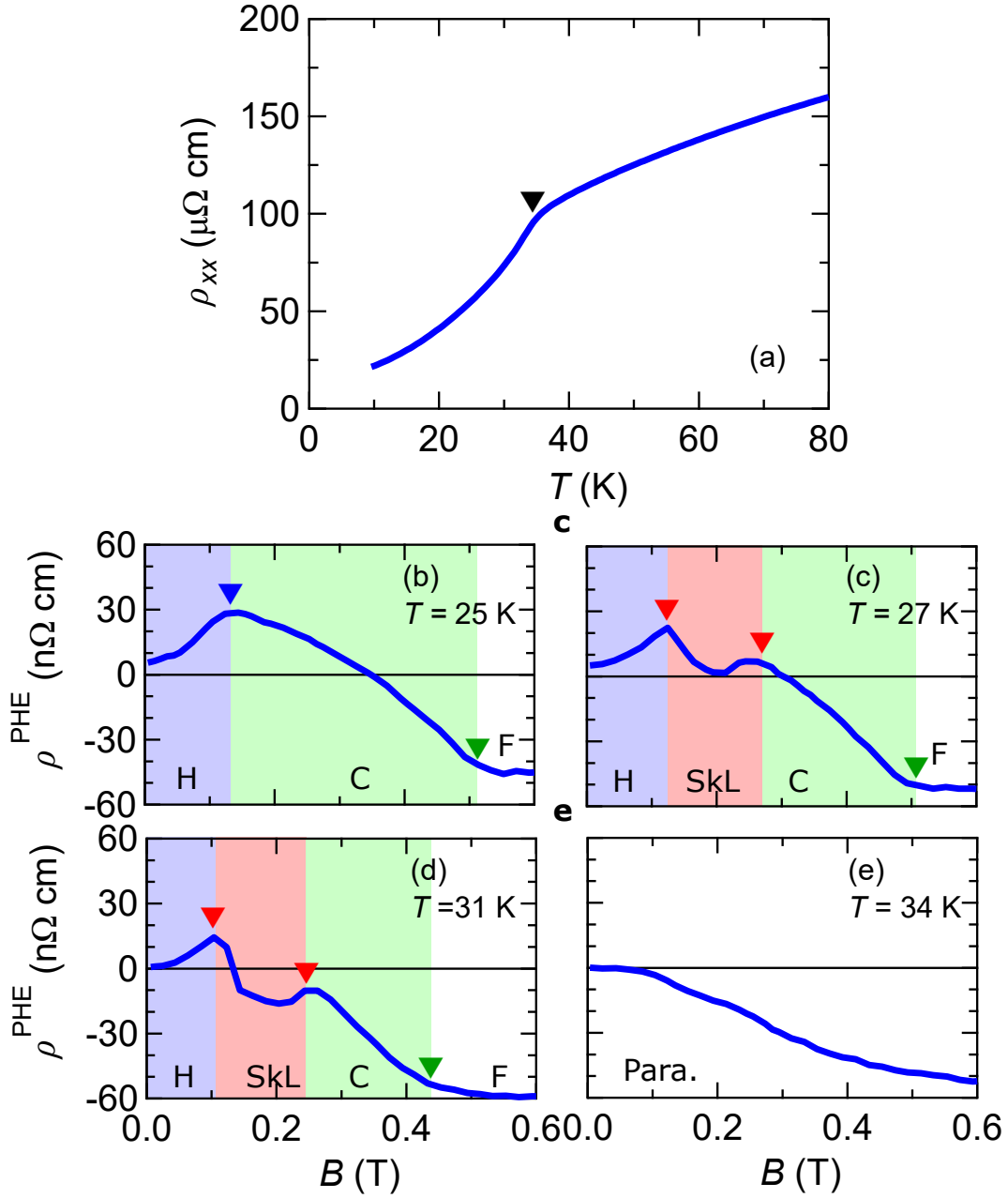
Figure 5.2: (a) Temperature (T) dependence of longitudinal resistivity (ρ_{xx}). We determined the helical-ordering temperature as the inflection point of the $\rho_{xx} - T$ curve (the black triangle). (b)-(e), Magnetic-field (B) dependence of planar Hall resistivity (ρ^{PHE}) at various temperatures. We assigned the kinks in B-dependence of ρ^{PHE} to the helical-to-conical transition (the blue triangle), helical/conical-to-skyrmion transition (the red triangles), and conical-to-ferromagnetic transition (the green triangles). The letters H, C, SkL, and F represent helical, conical, skyrmion-lattice, and ferromagnetic phases, respectively.
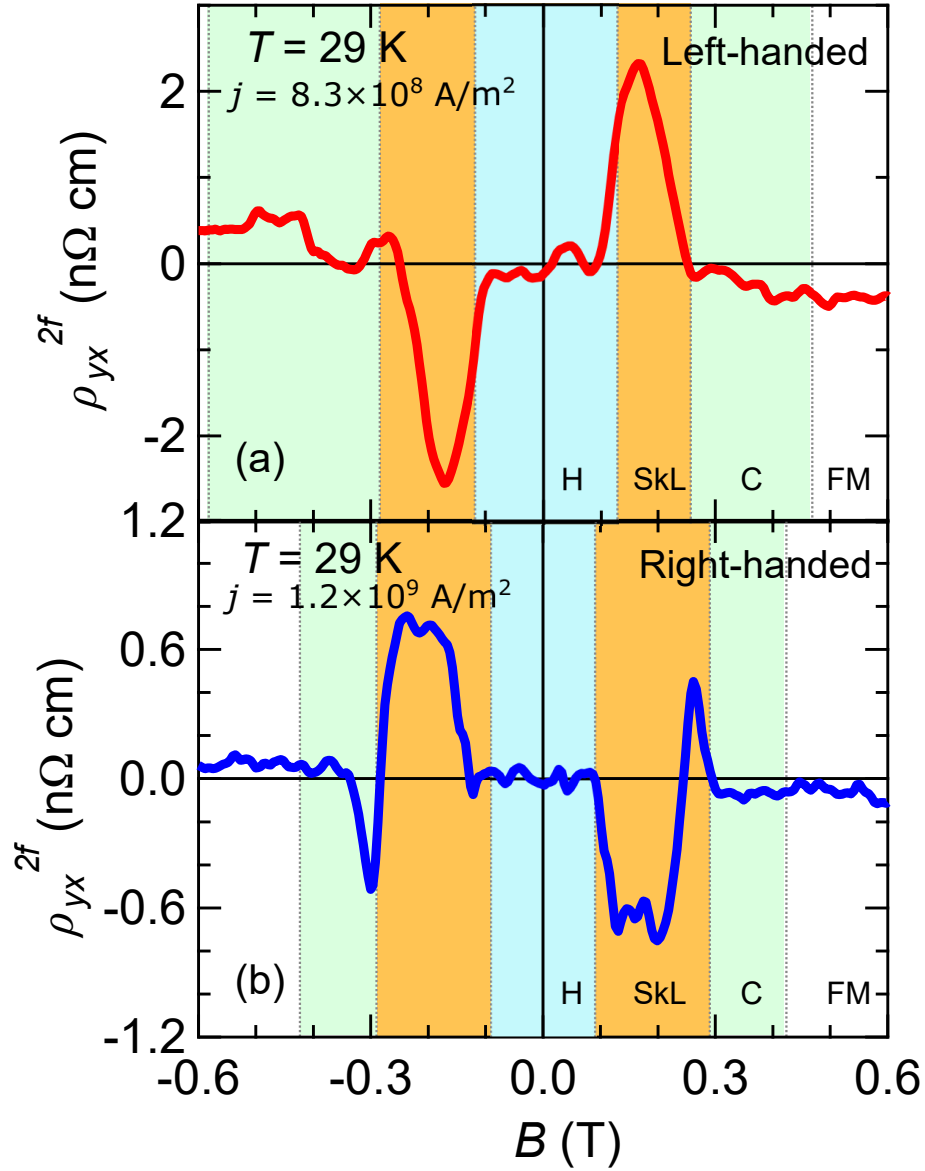
Figure 5.3: Magnetic field dependence of second-harmonic Hall resistivity (ρ_{zx}^{2f}) in right-handed (c) and left-handed MnSi crystals (d). The blue, orange, green, and white shadow represent helical (H), skyrmion lattice (SkL), conical (C), and ferromagnetic (FM) phase, respectively.

are directly linked to the nonreciprocal nonlinear Hall coefficient. First, we show typical profiles of the second-harmonic Hall effect. As shown in Figs. 5.3 (a) and (b), the B-dependence of $\mathrm{Re}\rho_{zx}^{2f}$ of both right- and left- handed crystal exhibits the prominent enhancement in the SkL phase. The signs of $\mathrm{Re}\rho_{zx}^{2f}$ are opposite between right- and left-handed crystal in accord with the expected contributions from the nonreciprocal nonlinear Hall effect. Figure 5.4 shows the B-dependence of $\mathrm{Re}\rho_{zx}^{2f}$ in left-handed MnSi with current density $j = 2.1 \times 10^8 \mathrm{A/m^2}$ (blue lines) and $j = 8.3 \times 10^8 \mathrm{A/m^2}$ (red lines) at various temperatures. The magnitude of $\mathrm{Re}\rho_{zx}^{2f}$ measured with $j = 2.1 \times 10^8 \mathrm{A/m^2}$ is small below noise levels. In contrast, in the case of $\mathrm{Re}\rho_{zx}^{2f}$ measured with $j = 8.3 \times 10^8 \mathrm{A/m^2}$, the prominent signals of $\mathrm{Re}\rho_{zx}^{2f}$ are observed in the skyrmion phase. The clear correspondence between SkL phase and the conspicuous $\mathrm{Re}\rho_{zx}^{2f}$ signals is further confirmed in the contour map of $\mathrm{Re}\rho_{zx}^{2f}$ with $j = 8.3 \times 10^8 \mathrm{A/m^2}$ in $T - B$ phase diagram (Fig. 5.5).

To gain more insight, we measured the detailed current-density dependence of ρ_{zx}^{2f}. Taking account of increase in the sample temperature owing to Joule heating, we derived the temperature from longitudinal resistivity of the thin plate sample itself, and adjusted the temperature of the heat bath so that the sample temperature was kept constant. Figure 5.6(a) shows current-density dependence of the temperature of the sample, assuring us that temperature of the sample is kept nearly constant within the range of $T = 29.0 \pm 0.08$ K. The current-density dependence of $\mathrm{Re}\rho_{zx}^{2f}$ at $T = 29$ K measured by using sine-wave AC current with $f = 13$ Hz exhibits the non-monotonous profile [Fig. 5.6(b)]. Here, we note that current-density dependence measured by using sine-wave AC current and square-wave current is almost similar. This result rules out the possibility that the non-monotonous current dependence results from temporal temperature change, which would possibly occur in the case of sine-wave AC current but not in the case of square-wave current [see Figs. 5.7(a) and (b)]. When a square-wave current applied, the nonreciprocal nonlinear Hall voltage appears as a constant DC voltage V_z^{DC} parallel to magnetic field. Here we define nonreciprocal nonlinear Hall
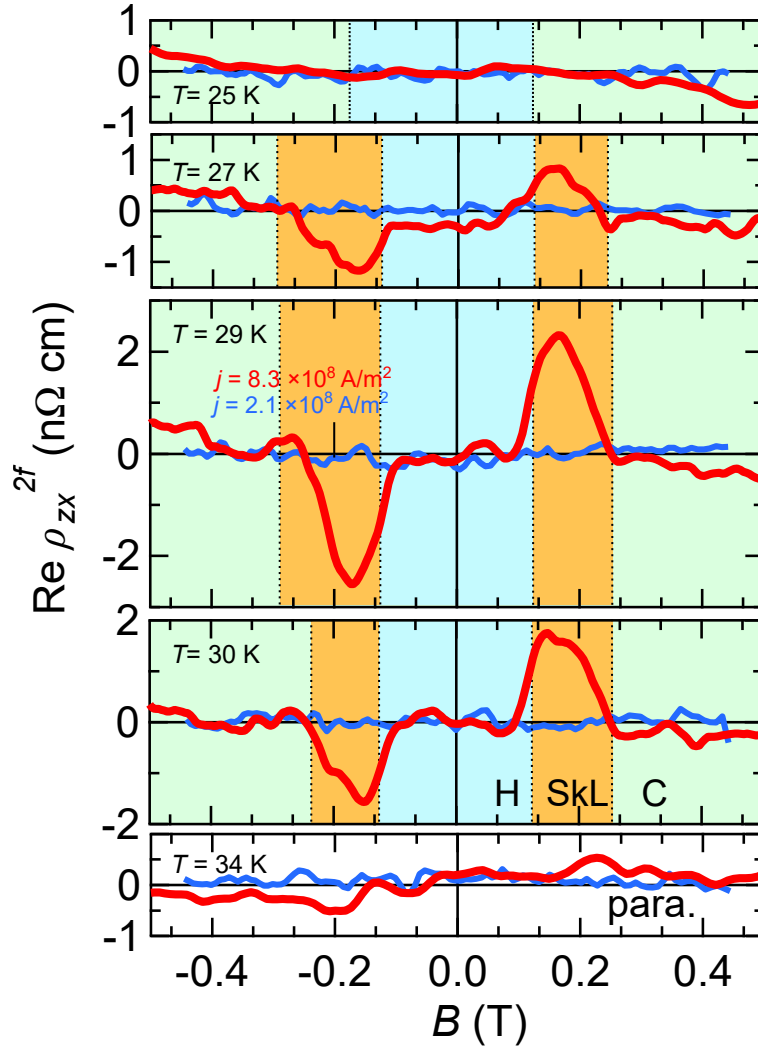
Figure 5.4: Magnetic field dependence of real part of second-Hall resistivity (Re ρ_{zx}^{2f}) measured with current density $j = 2.1 \times 10^8 \mathrm{A/m^2}$ (blue lines) and $j = 8.3 \times 10^8 \mathrm{A/m^2}$ (red lines). The blue, orange, green, and white shadow represent helical (H), skyrmion lattice (SkL), conical (C), and ferromagnetic (FM) phase, respectively.

resistivity measured by using the square-wave current as $\rho_{zx}^{\mathrm{square}} = V_z^{\mathrm{DC}}/j_x d$. As in the case of the measurement using the sine-wave current, we estimated the sample temperature from the longitudinal resistivity, and adjusted the temperature of the
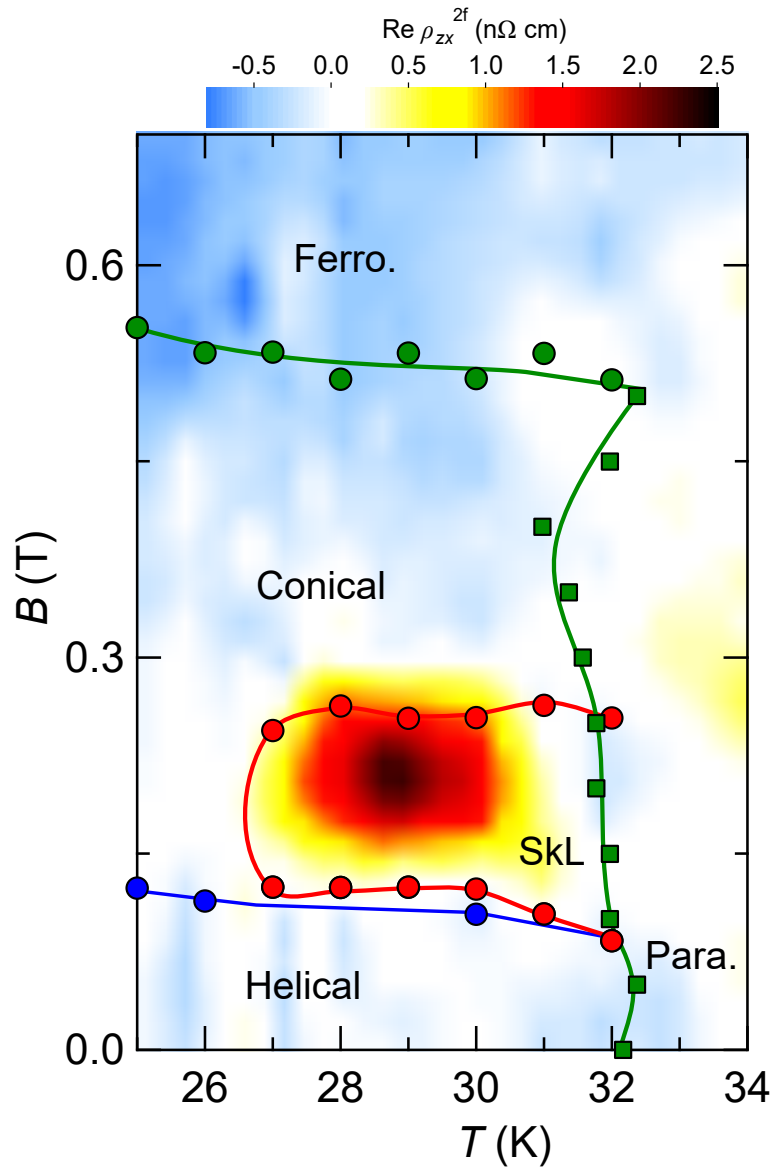
Figure 5.5: Contour mapping of second-Hall resistivity (Re ρ_{zx}^{2f}) in the plane of temperature and magnetic-field. The blue, green, red circles denote the phase transitions of helical-to-conical, conical-to-ferromagnetic, and skyrmion-to-conical phase, respectively, determined from kinks in magnetic-field dependence of planar Hall resistivity. The green squares represent the phase transitions of helical, conical, SkL to paramagnetic phase determined from inflection points of temperature dependence of longitudinal resistivity

heat bath of PPMS to control the cooling power. As shown in Fig. 5.7(c) the sample temperature stays almost constant. As shown in Fig. 5.7(d), the current dependence of $\rho_{zx}^{\text{square}}$ in the skyrmion phase exhibits a profile almost similar to that of second harmonic Hall resistivity measured by using the sine-wave current [Fig. 5.6(b)]. This result rules out the possibility that the non-monotonous current dependence of second-harmonic Hall resistivity measured by using the sine-wave current results from the possible temporal temperature change.
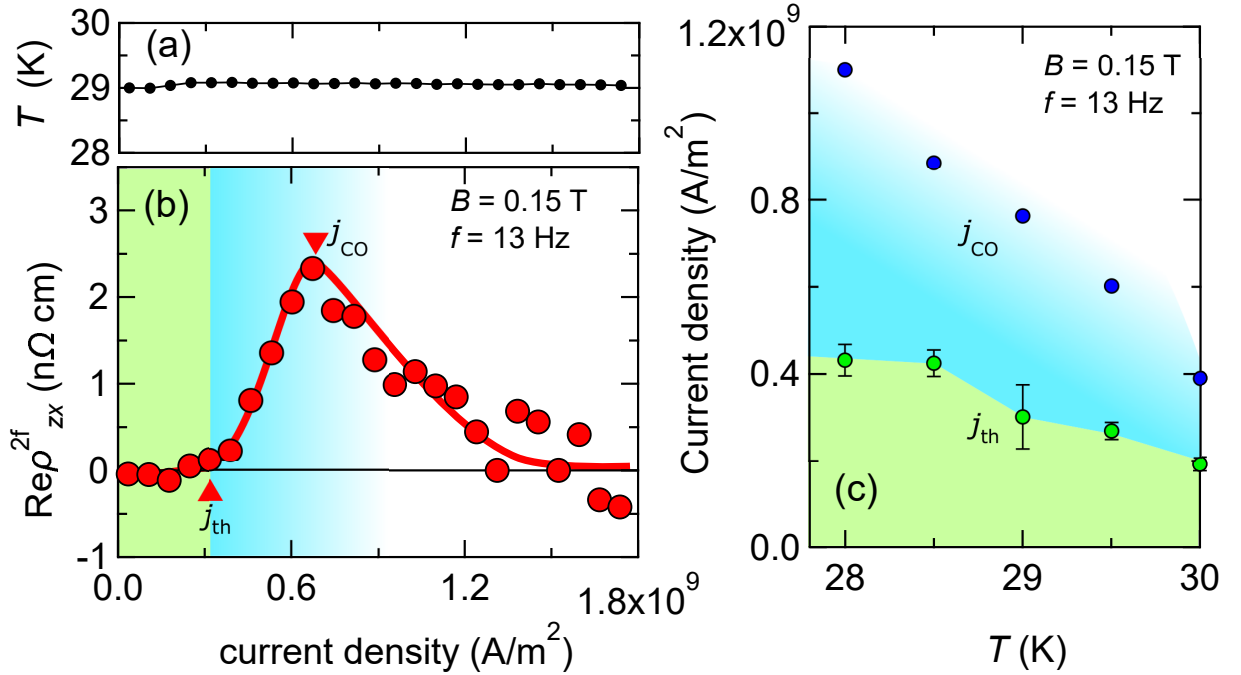
Figure 5.6: The current density (j) dependence of temperature of MnSi thin plate sample estimated from longitudinal resistivity (a) and real part of second-harmonic Hall resistivity (Re ρ_{zx}^{2f}) at $B = 0.15$ T measured with frequency $f = 13$ Hz (b). The red solid curve is a guide to eyes. (c) The temperature dependence of threshold current densities j_{th} and the crossover point j_{CO} at $B = 0.15$ T. The values of j_{th} and j_{CO} at $T = 29.0$ K are represented as inverse triangles in Fig. 5.6(b).

The profile of the current-density dependence of Reρ_{zx}^{2f} is divided into the dis-
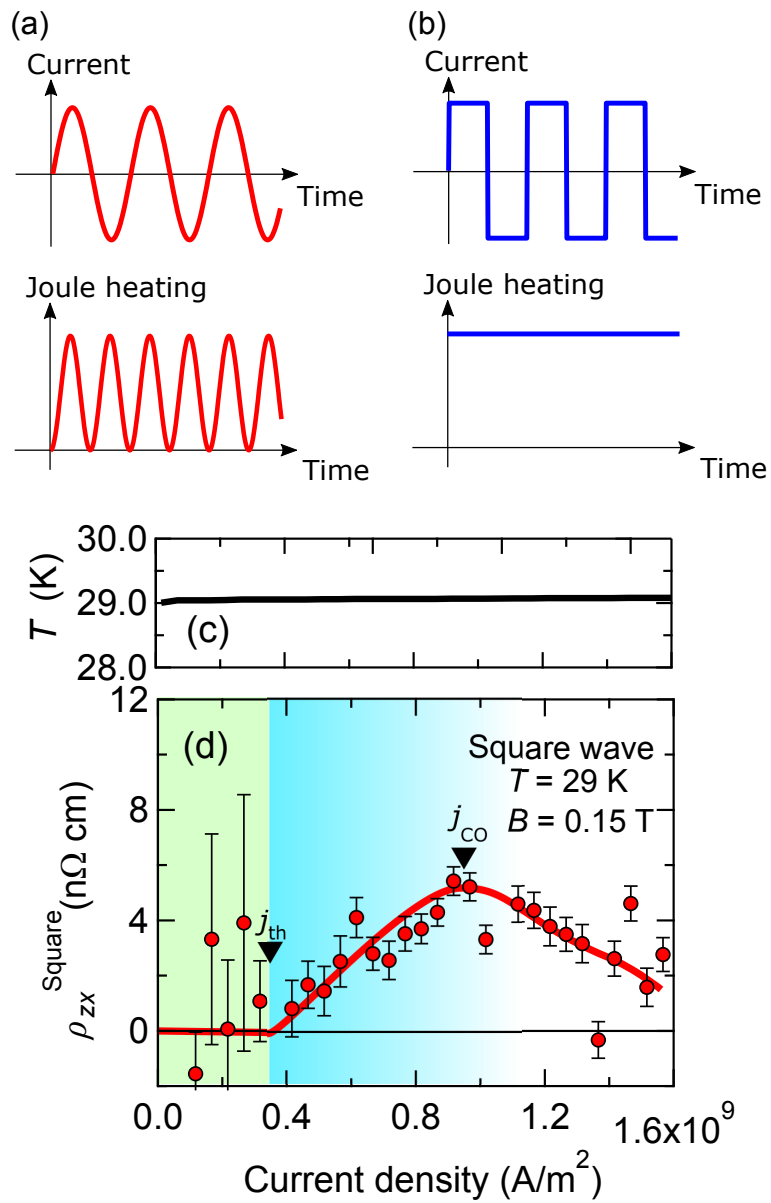
Figure 5.7: Schematic illustrations of time profiles of the sine-wave (a) and square-wave (b) input currents, and those of their corresponding Joule heating. The current dependence of sample temperature estimated from the longitudinal resistivity measurement (c) and non-reciprocal Hall effect measured using square-wave current (d).

tinct three regimes: (1) almost zero below $j_{th} = 3.2 \times 10^8 A/m^2$, (2) monotonic increase between j_{th} and $j_{CO} = 8.9 \times 10^8 A/m^2$, and (3) monotonic decrease above j_{CO}. This indicates that the nature of the SkL state changes with increasing current density. In fact, such changes are widely observed in charge density wave (CDW) [89, 90] and SC vortex [91, 92]: (1) pinned lattice state at low current densities, (2) disordered flow of lattice affected by pinning potential in intermediate current densities, and (3) recovery of crystallinity due to the motional narrowing, i.e., relative reduction of pinning force, at large current densities, termed the dynamical reordering. In fact, such a dynamical phase diagram is also theoretically predicted for SkL in the presence of strong random pinning potential [93]. On the basis of this theoretical prediction and the analogy to dynamical phase diagrams of CDW and SC vortex, we assign j_{th} and j_{CO} to the onset of disordered translational motion and dynamical reordering of skyrmion strings, respectively. Note that jth corresponds to the dynamical phase transition point, while j_{CO} characterizes the crossover (CO). The temperature dependences of j_{th} and j_{CO} are also consistent with the above assignment; j_{th} and j_{CO} decrease with increasing temperature as shown in Fig. 5.6(c), because thermal activation effectively weakens the pinning force. Therefore a plausible scenario accounting for the non-monotonous current dependence of ρ_{zx}^{2f} is that the translational motion of deformed skyrmion strings occurs at the current densities between j_{th} and j_{CO}, leading to the second-harmonic Hall signal along B-direction. We note that the critical current density required for translational motion of SkL $j_{th} = 3.2 \times 10^8 A/m^2$ is two orders of magnitude larger than that in bulk MnSi [51, 52]. This is perhaps due to the chemical disorder/strain on the wide top and bottom surfaces of the sample plate caused by the device fabrication procedure with focused ion (Ga ion) beams, which acts as additional pinning sites for skyrmion strings.

The close relationship between second-harmonic Hall effect and the translational motion of skyrmion strings is further confirmed by dependence of ρ_{zx}^{2f} on the input-current frequency. In Fig. 5.8(a), we show the frequency dependence of
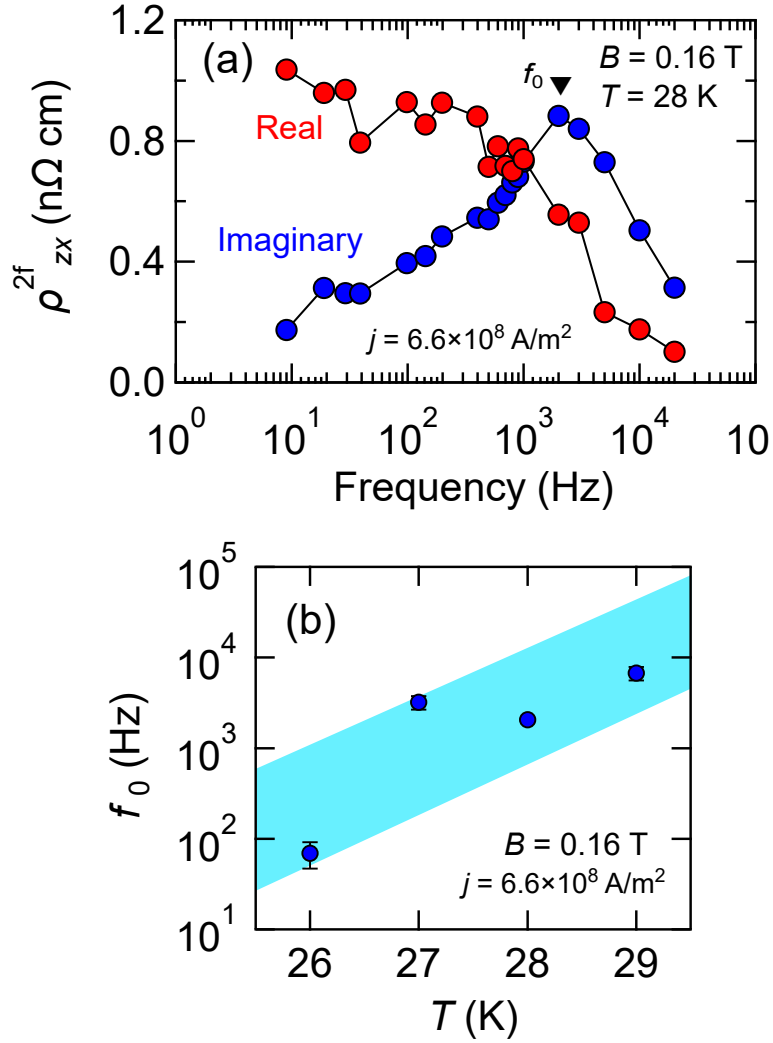
Figure 5.8: (a) Dependence of real part (red line) and imaginary part (blue line) of ρ_{zx}^{2f} on the input current frequency at $T = 28$ K and $B = 0.16$ T. (b), Temperature dependence of frequency where imaginary part of ρ_{zx}^{2f} peak (f_0). The f_0 at $T = 28$ K are represented by the inverse triangle in Fig. 5.8(a). The thick light blue band is a guide to eyes.

$\text{Re}\rho_{zx}^{2f}$ and $\text{Im}\rho_{zx}^{2f}$ measured with $j = 7.0 \times 10^8 \text{A/m}^2$ at $T = 28$ K. Around $f = 3$ kHz, $\text{Re}\rho_{zx}^{2f}$ shows rapid decrease together with the $\text{Im}\rho_{zx}^{2f}$ peak, and both $\text{Re}\rho_{zx}^{2f}$ and $\text{Im}\rho_{zx}^{2f}$ are almost zero above $f = 6$ kHz. This non-monotonous frequency dependence in the range of the present frequency range ($f < 10$ kHz) cannot
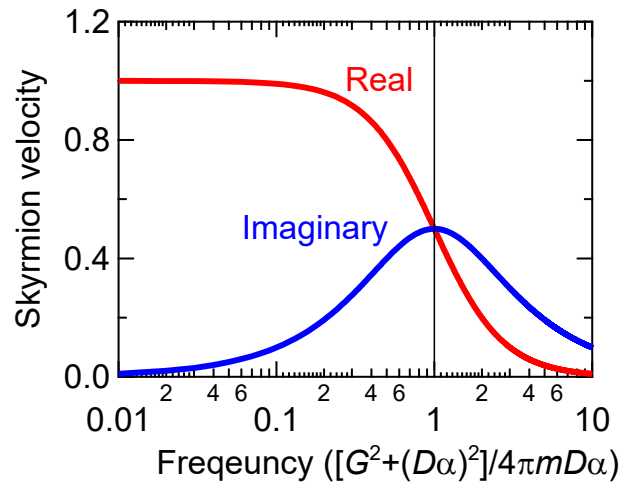
Figure 5.9: The real part (red) and imaginary part (blue) of frequency-dependent skyrmion velocity derived from Thiele's equation. The vertical and horizontal axes are normalized by the velocity at zero frequency and $f = (G^2 + (D\alpha)^2)/4\pi m D\alpha$, where G, D, α and m are gyromagnetic coupling, dissipative force, the coefficients for Gilbert damping.

be explained by conventional mechanisms of second-harmonic Hall effect, such as spin-orbit torque [88] or asymmetric electron-magnon scattering [94], whose typical frequencies are several gigahertz. Since characteristic frequency in motion of nanoscale spin structures such as ferromagnetic domain wall is below several megahertz [95], the observed frequency dependence can be interpreted as representing the relationship between ρ_{zx}^{2f} and translational motion of skyrmion strings; skyrmion string cannot follow the AC current with high frequency above $f = 6$ kHz. In fact, the profile of the observed frequency dependence of ρ_{zx}^{2f} resembles that of the skyrmion velocity (v_{SK}) derived from Thiele's equation:

$$v_{\mathrm{Sk}}^x(f) = \frac{G/(G^2 + (D\alpha^2)}{1 + 2\pi i \frac{2mD\alpha}{(G^2 + (D\alpha)^2} f} v_{\mathrm{e}}. \tag{5.2}$$

Here, m, D, α and v_{e} are effective mass of skyrmion, dissipative force constant, the Gilbert damping coefficient, and drift velocity of electrons, respectively. Because the skyrmion velocity perpendicular to the current direction (v_{Sk}^y) is smaller than v_{Sk}^x, we ignore v_{Sk}^y. As shown in Fig 5.9, the real part of $v_{\mathrm{Sk}}^x(f)$ begins to decrease around $f = [G^2 + (D\alpha)^2]/4\pi mD\alpha$, and the imaginary part of $v_{\mathrm{Sk}}^x(f)$ exhibits the peak at $f = [G^2 + (D\alpha)^2]/4\pi mD\alpha$. This is because skyrmions motion cannot follow the driven AC current with frequency above $f = [G^2 + (D\alpha)^2]/4\pi mD\alpha$. The frequency profile of skyrmion velocity resembles that of second-harmonic resistivity [Fig. 5.8(a)], which supports the relationship of nonlinear Hall signal to translational motion of SkL. Additionally, as shown in Fig. 5.8(b), the frequencies (f_0) at which Imρ_{zx}^{2f} peaks increases with increasing temperature. Because skyrmion strings can be driven faster at higher temperatures owing to assistance of thermal activation, the temperature dependence of f_0 also reasonably supports the relationship between ρ_{zx}^{2f} and the translational motion of SkL.

5.3   Current-induced dynamics of skyrmion strings

In order to clarify the dominant mechanism of the nonlinear Hall signal along B-direction, Hoshino calculate the current-induced dynamics of skyrmion strings and consequent emergent electromagnetic field in the presence of impurity potential. The model corresponds to the experimental situations in which skyrmion strings flow while accompanying distortions (i.e. $j_{\text{th}} < j < j_{\text{CO}}$). In the following, we demonstrate that the experimental observation is well explained in terms of current-driven asymmetric flexible bending dynamics of skyrmion string and consequent generation of emergent electromagnetic field. On the basis of the spin density wave picture, the spin texture for SkL is given by the triple-helix state with the modulated phase in space-time [7, 4, 96]. This deformation corresponds to the low-lying spin-wave excitation modes of SkL, namely phason [96]. The response function for phasons is calculated from the energy cost of the deformation based on the DM ferromagnetic Hamiltonian in the presence of impurities [97]:

$$H = \int \frac{d\boldsymbol{r}}{a^3} \left[\frac{1}{2} J a^3 (\boldsymbol{\nabla}\boldsymbol{n})^2 + D a \boldsymbol{n} \cdot (\boldsymbol{\nabla} \times \boldsymbol{n} - g\mu_{\text{B}}\boldsymbol{B} \cdot \boldsymbol{n}) \right] + \int \frac{d\boldsymbol{r}}{l^3} V(\boldsymbol{r})(n_z)^2 \quad (5.3)$$

where the first, second, third and fourth terms are Heisenberg interaction, DM interaction, Zeeman term, and impurity potential, respectively. The length l ($>$ lattice constant a) is an averaged distance between impurities, and the inverse of skyrmion radius is given by $Q = |D|/(Ja)$ in this model. Combining the above Hamiltonian with the Berry phase term in the action, we derive a dynamical response function. The excitation energy $\epsilon(q)$ of SkL, which is determined from the pole of the response function, has the following form: $\epsilon(q) = \alpha q^2 + \beta q^4 + \gamma q^4 q_z + O(q^6)$ [Fig. 5.10(a)]. The third term with q_z shows nonreciprocity of skyrmion string dynamics along z direction, which is crucial for the nonlinear Hall effect as shown in the following.

To provide an intuitive picture for the current-induced string dynamics in the presence of impurities and consequent emergent electromagnetic fields, we focus on a single flowing skyrmion string deformed to avoid an impurity. Bending of the
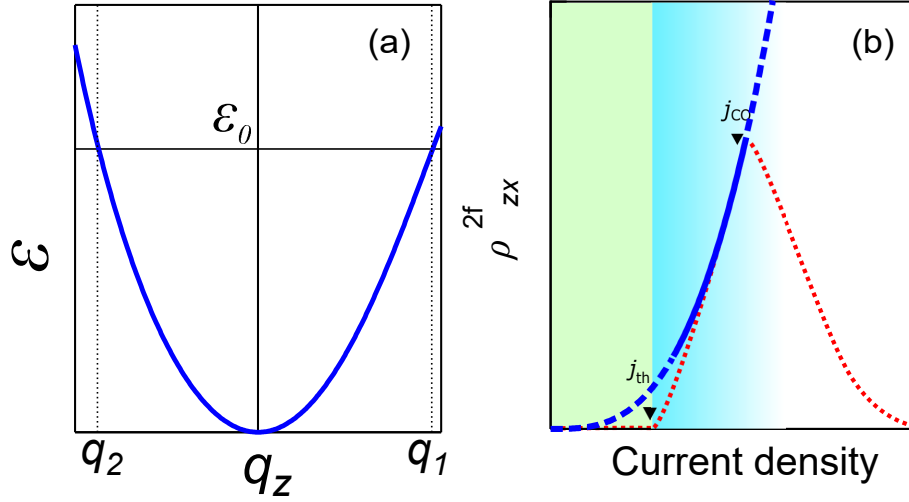
Figure 5.10: (a) Dispersion relation of low-energy excitation (ϵ) of SkL with a propagating vector along external magnetic field direction (q_z). (b) Schematic picture for current dependence of nonlinear Hall resistivity. The blue solid line represents the theoretical calculation, which is valid for the current density between j_{th} and j_{CO}, and the blue broken line is square of current density (guide to eyes). Red line is the experimentally observed current profile [see also Fig. 5.6(a)].

skyrmion string is described by displacement vector $u = (u_x, u_y, 0)$ [Fig. 5.11 (a)], and the Hall electric field originating from emergent magnetic and electric field is given by $\boldsymbol{E} = \boldsymbol{e} + (\boldsymbol{v}_{\text{e}} - \boldsymbol{v}_{\text{Sk}}) \times \boldsymbol{b}$, where $\boldsymbol{v}_e = v_e \hat{\boldsymbol{x}}$ and $\boldsymbol{v}_{Sk} = v_{Sk} \hat{\boldsymbol{e}}$ are velocity of electron and skyrmion ($v_{Sk} < v_e$), and $\boldsymbol{e} = -\dot{\boldsymbol{u}} \times \boldsymbol{b}$ and $(\boldsymbol{v}_{\text{e}} - \boldsymbol{v}_{\text{Sk}}) \times \boldsymbol{b}$ are the emergent electric field and topological Hall electric field in the moving frame of skyrmion, respectively. As shown in Figs. 5.11(a) and (d), the electric field E_z along magnetic field direction is nonzero only when a skyrmion string bends. For detailed investigation of electric fields along the B-direction arising from current-induced dynamical bending, we calculate time evolution of the bending skyrmion string by using $\epsilon(q)$ and its eigenmode and the concomitant magnitude of $[(\boldsymbol{v}_{\text{e}} - \boldsymbol{v}_{\text{Sk}}) \times \boldsymbol{b}]_z$ and $e_z = -[\dot{\boldsymbol{u}} \times \boldsymbol{b}]_z$. Figures 5.11(b) and (e) are time evolution of

a bending skyrmion string shown together with the color map of the magnitude of $[(\boldsymbol{v}_{\mathrm{e}} - \boldsymbol{v}_{\mathrm{Sk}}) \times \boldsymbol{b}]_z$ and $e_z = -[\dot{\boldsymbol{u}} \times \boldsymbol{b}]_z$, respectively, and Figs. 5.11(c) and (f) are time dependence of the averages of $[(\boldsymbol{v}_{\mathrm{e}} - \boldsymbol{v}_{\mathrm{Sk}}) \times \boldsymbol{b}]_z$ and $e_z = -[\dot{\boldsymbol{u}} \times \boldsymbol{b}]_z$ over the skyrmion string. At the initial state $(t = 0)$, because deformation is symmetric, both $[(\boldsymbol{v}_{\mathrm{e}} - \boldsymbol{v}_{\mathrm{Sk}}) \times \boldsymbol{b}]_z$ and $e_z = -[\dot{\boldsymbol{u}} \times \boldsymbol{b}]_z$ cancel out. With increasing time, however, the skyrmion string asymmetrically deforms due to the nonreciprocity of the dispersion, which leads to nonzero average of $[(\boldsymbol{v}_{\mathrm{e}} - \boldsymbol{v}_{\mathrm{Sk}}) \times \boldsymbol{b}]_z$ and $e_z = -[\dot{\boldsymbol{u}} \times \boldsymbol{b}]_z$. The above intuitive picture thus indicates asymmetric deformation of skyrmion strings and therein the emergent electromagnetic fields play a crucial role in the nonreciprocal nonlinear Hall signal along the B-direction.

Hoshino calculate the the nonreciprocal response in SkL and obtain the nonreciprocal Hall resistivity defined by $E_z^{\mathrm{DC}} = \rho_{zx}^{\mathrm{DC}} j_x$

$$\rho_{zx}^{\mathrm{DC}} \sim \frac{\hbar a}{e^2} \frac{\left(\frac{\hbar a^2}{e} j_{\mathrm{c}}\right)^3}{(^2 D} \left(\frac{j}{j_{\mathrm{c}}}\right)^2, \tag{5.4}$$

where the electrical current is given by $j = e n_e v_e$ with $n_e = a^{-3}$ being an electron density. From Eq. 5.4, the sign of D, which depends on crystal chirality, corresponds to the sign of nonreciprocal Hall resistivity, which is consistent with the experimental observation. With the parameter values for MnSi, typical value at $j = 2j_{\mathrm{c}}$ is estimated as $\rho_{zx}^{\mathrm{DC}} 0.6 \mathrm{n\Omega\,cm}$, which is comparable to the experimental values.

Although Eq. 5.4 is valid in the disordered-skyrmion flowing regime at the current density with $j_{\mathrm{th}} < j < j_{\mathrm{CO}}$, the above microscopic mechanism also qualitatively explain the experimental observation of the decrease of the nonreciprocal Hall signal above j_{CO}, which we assign to the onset of the dynamical reordering (i.e. onset of reduction of effective pinning force). Since the stronger disorder potential gives the larger deformation of SkL, the nonreciprocal Hall signal is an increasing function of strength of pinning potential. Therefore the effective reduction of pinning force reduces the deformation of skyrmion strings, leading the decrease of nonreciprocal Hall signals.
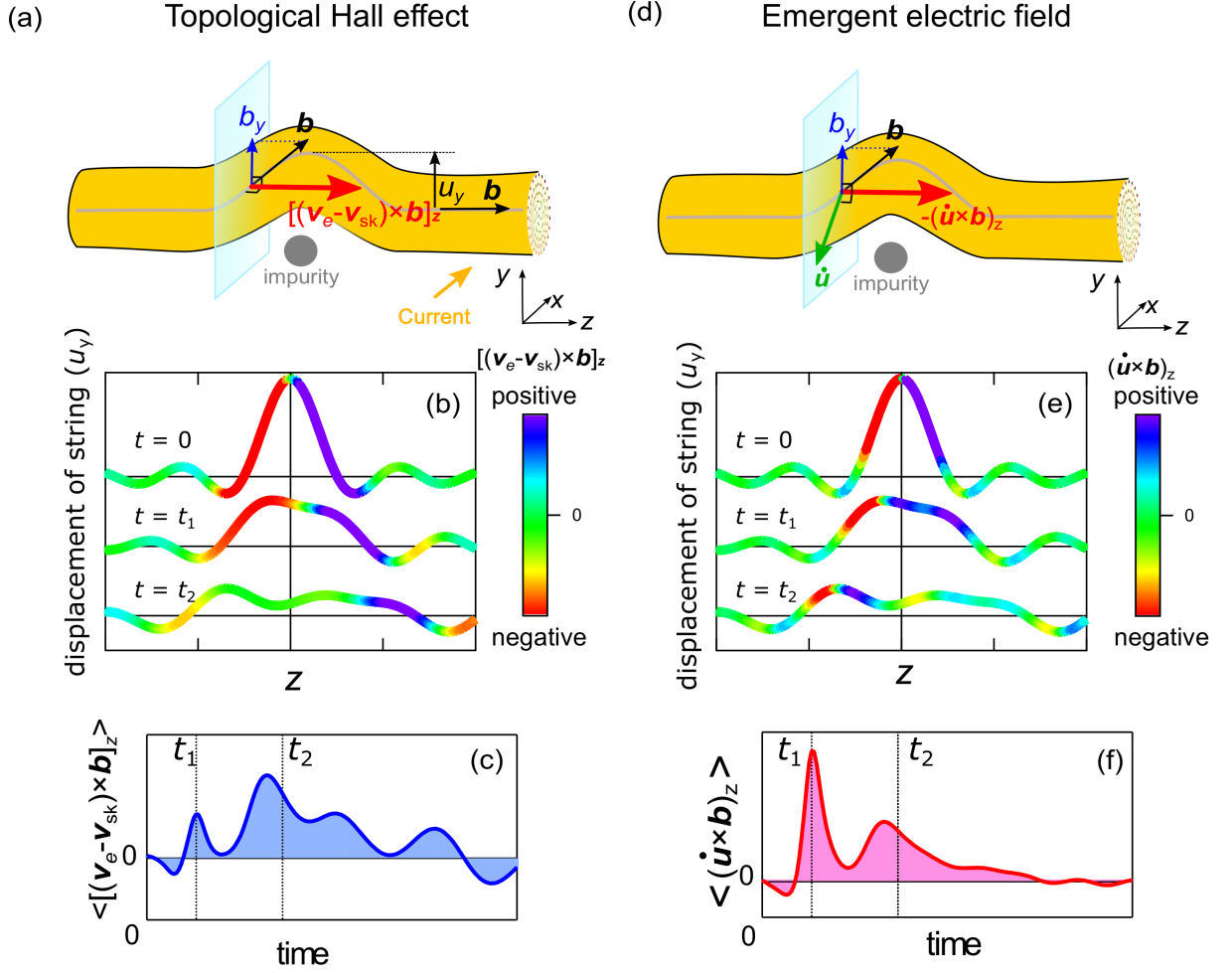
Figure 5.11: Schematic pictures of emergent electromagnetic field for the deformation of a skyrmion string when it collides with point-like impurity. The u represents the displacement vector of skyrmion string. The red arrows demonstrate z-components of topological Hall electric field $[(\boldsymbol{v}_{\mathrm{e}} - \boldsymbol{v}_{\mathrm{Sk}}) \times \boldsymbol{b}]_z$ (a) and emergent electric field $e_z = -[\dot{\boldsymbol{u}} \times \boldsymbol{b}]_z$ (d). The positon (z) dependence of displacement of skyrmion strings shown together with color map of z-components of both $(\boldsymbol{v}_{\mathrm{e}} - \boldsymbol{v}_{\mathrm{Sk}}) \times \boldsymbol{b}$ (b) and $\boldsymbol{e} = -\dot{\boldsymbol{u}} \times \boldsymbol{b}$ (e) at several time points. Time dependence of the averaged z-components of both $[(\boldsymbol{v}_{\mathrm{e}} - \boldsymbol{v}_{\mathrm{Sk}}) \times \boldsymbol{b}]_z$ (c) and $\boldsymbol{e} = -\dot{\boldsymbol{u}} \times \boldsymbol{b}$ (f) over the skyrmion string.

5.4 Summary

In this section, we have demonstrated that the current-induced asymmetric deformation of skyrmion strings arising from both its flexible nature and the Dzyaloshinskii-Moriya interaction results in nonreciprocal transport response related to the real-space Berry phase of skyrmion string. The asymmetric dynamics and consequent nonreciprocal transport response are one of the generic properties of dynamics of string-like objects in non-centrosymmetric systems including vortex lines in non-centrosymmetric superconductors as well as skyrmion string in nonsymmetric mangets investigated here.

Chapter 6

Transport properties ans stability of skyrmions in MnSi thin films

6.1 Introduction

In favor of such applications, thin films of skyrmionic materials offer the stage of stable skyrmions in a wide temperature range below the magnetic transition temperature (T_c),[8, 17, 98] whereas the helical or the conical spin state almost dominates the temperature (T)-magnetic field (B) phase diagram in the bulk sample.[7, 14, 99] Theoretical studies based on a two-dimensional (2D) model well reproduce the experimental T-H phase diagram of the $Fe_{0.5}Co_{0.5}Si$ thinned (< 100 nm) plate [8], in which the helical or conical modulation period (~ 90 nm) is comparable to or longer than the sample thickness. This is perhaps because the quasi-two-dimensional skyrmion state is stabilized relatively to the helical or conical state with the modulation vector normal to the plate, when the magnetic field is applied normal to such a thin plate. In contrast, an effect of uniaxial magnetic anisotropy on stability of skyrmion also has been studied; theoretically, when a magnetic field is applied in the easy-plane or parallel to the easy-axis, skyrmions are stabilized. Since epitaxial thin film of MnSi on Si(111) substrates

has an easy-plane anisotropy arising from a tensile strain due to the lattice mis-match, skyrmions are expected to be stabilized when an in-plane magnetic field is applied, which is an array of skyrmion strings stretching in the plane of the thin films [100] (i.e. in-plane skyrmion) [Fig. 6.1(a)]. However, there have been few comprehensive studies on stability of both the quasi-two-dimensional skyrmions and the in-plane skyrmions in thin films.

To this end, we employ (1) planar Hall effect to detect the formation of in-plane skyrmion and (2) topological Hall effect to detect the quasi-two-dimensional skyrmion. By measurements of planar Hall effect (PHE), which sensitively extracts an anisotropic component of electrical conductance, we identify the emergence of skyrmions. In-plane skyrmions appears at low temperatures, which is distinct from the hitherto known skyrmion phase stretching from T_c. The in-plane skyrmion strings are stabilized by the magnetic anisotropy, which is enhanced at low temperatures. By measurement of topological Hall effect, we also identified the formation of quasi-two dimensional skyrmions in a wide temperature range below T_c when out-of-plane magnetic field is applied. The topological signal is largest in the vicinity of T_c, indicating the number of quasi-two-dimensional skyrmions reaches a maximum near T_c, which differ from the phase diagram for the in-plane skyrmion. These results indicate the dominant mechanism of the stabilization for the in-plane skyrmion and the quasi-two-dimensional skyrmions is different. We also demonstrate a systematic change of skyrmion stability as a function of thickness (t) and helical period (λ), the latter of which can be controlled by Fe content x.

6.2 Formation of in-plane skyrmions in MnSi thin films

To detection of the in-plane skyrmion strings forming in the epitaxial MnSi thin films, we apply the PHE measurement, which is a sensitive probe for skyrmion formation as discussed in Chapter 3. In Fig. 6.1 are presented the magnetic field dependencies of magnetization M, magnetoresistivity normalized by its value at zero field $\rho_{xx}(B)/\rho_{xx}(0)$, and PHE signal normalized by the longitudinal resistivity at zero field $\rho_{yx}^{\mathrm{PHE}}/\rho_{xx}(0)$, at three temperatures (2, 10, 30 K). Magnetoresistivity and PHE are measured with electric current $J \parallel [1\bar{1}0]$ and with magnetic field $B \parallel J$ and $B \parallel (111)$ surface, respectively. It is obvious that PHE signal shows a distinctive anomaly characteristic of the skyrmion formation at low temperatures below 20 K [Figs. 6.1(i) and 6.1(j)]. Given the theoretical prediction [100], the skyrmion strings stretching along the in-plane B in the thin film are likely responsible for the PHE anomalies, as schematically shown in Fig. 6.1(a). Between 20 K and 40 K($\approx T_{\mathrm{c}}$), all the three quantities [M, $\rho_{xx}(B)/\rho_{xx}(0)$, and $\rho_{yx}^{\mathrm{PHE}}/\rho_{xx}(0)$] indicate only one distinct magnetic transition at B_{c} as exemplified in Figs. 6.1(e), (h), and (k). Above T_{c}, no significant signals are observed (not shown). We note that there are observed tiny anomalies in M and $\rho_{yx}^{\mathrm{PHE}}/\rho_{xx}(0)$ at intermediate fields between the zero field and the critical field B_{c} at $T = 25$–35 K [see also Figs. 6.1(e) and 6.1(k)]. These may indicate sparse formation of skyrmion strings.

The magnetic field range of the PHE anomaly ($B_{\mathrm{sk1}} < B < B_{\mathrm{sk2}}$) extends well above B_{c} [Figs. 6.1(i) and (j)] and even reaches zero field in the decreasing field process at 10 K [Fig. 6.1(j)]. Once skyrmions are created, they coexist with other magnetic phase persisting beyond their thermodynamical-stability B-region. This originates from the first-order phase transition nature associated with topological change in the magnetic texture, i.e., unwinding the skyrmions costs a considerable barrier energy. Because of the topologically-stable nature of skyrmions, the
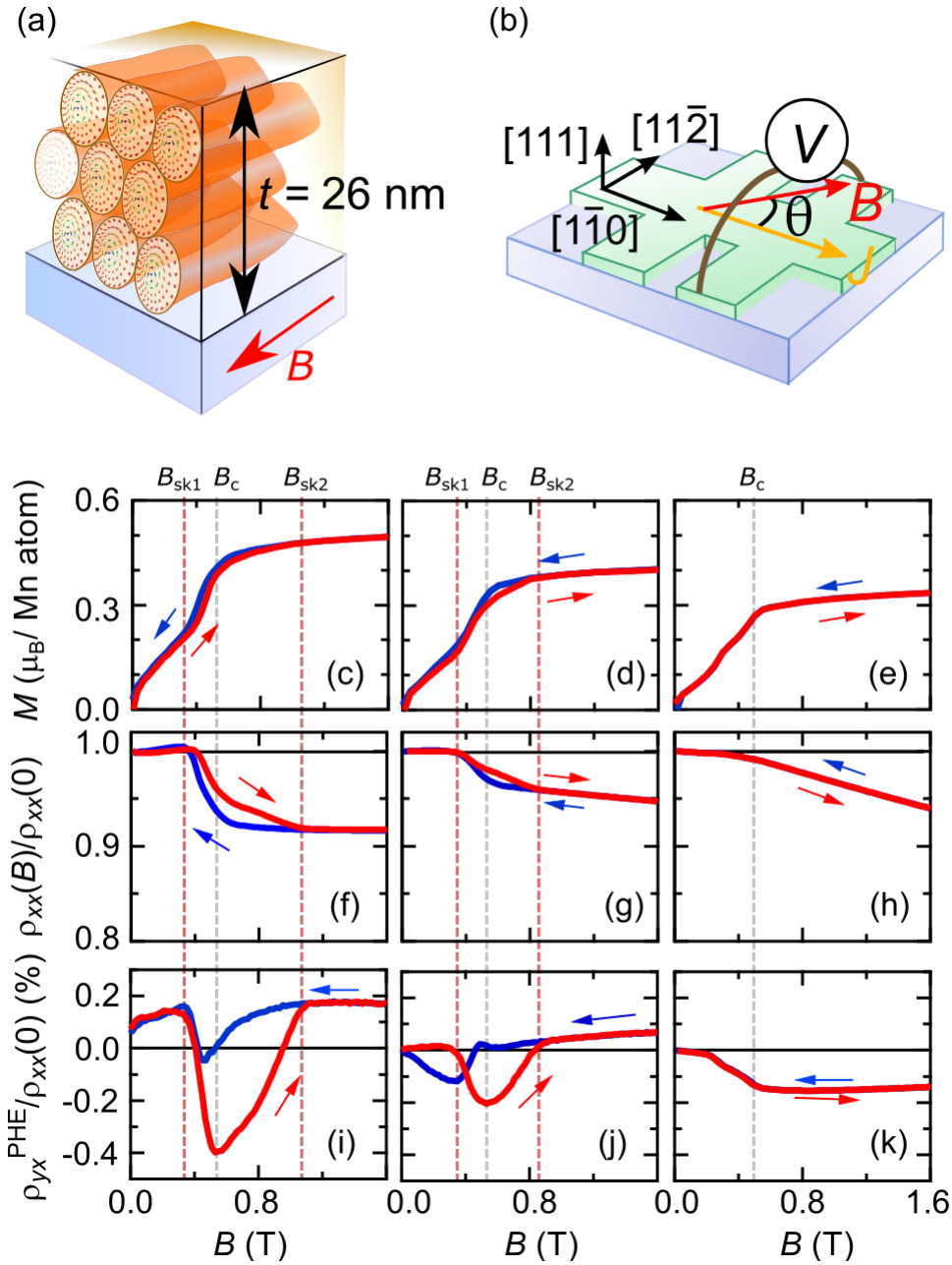
Figure 6.1: (a) A schematic illustration of the skyrmion formation in the presence of in-plane magnetic field. (b) An experimental setup for the measurement of PHE. Magnetic-field dependence of (c)-(e) magnetization, (f)-(h) magnetoresistivity, and (i)-(k) planar Hall resistivity of 26-nm MnSi thin film at 2 K, 10 K, and 30 K. Red lines indicate the data taken with increasing field and blue lines the data with decreasing field. The vertical dashed lines represent B_{sk1}, B_{sk2}, and B_c; B_{sk1} and B_{sk2} correspond to the lower and upper critical fields of the ρ_{yx}^{PHE}-hysteretic regime, where the ρ_{yx}^{PHE} originating from the in-plane skyrmions appears, and B_c stands for the critical field above which the spin collinear ferromagnetic state shows up.
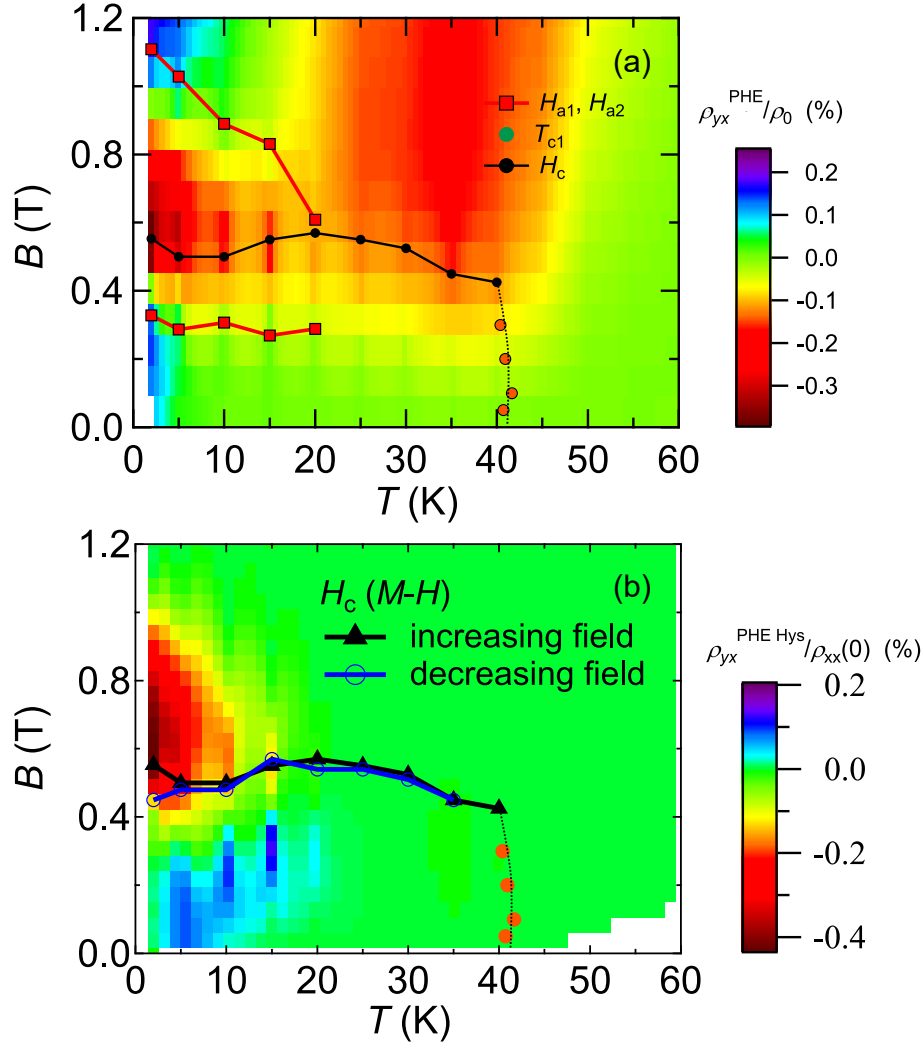
Figure 6.2: Color maps of (a) planar Hall resistivity (ρ_{yx}^{PHE}) normalized by longitudinal resistivity at zero field with increasing field and (b) $\Delta\rho_{yx}^{\mathrm{PHE,Hys}}/\rho_{xx}(0)$ defined by the hysteretic component of ρ_{yx}^{PHE} in the magnetic field scans [see Figs. 6.1(i)-(k)]. Squares represent B_{sk1} and B_{sk2}. Solid triangles and open circles represent B_{c} with increasing field and decreasing field, respectively. Orange circles represent transition temperature T_{c}.

hysteretic skyrmion formation with respect to magnetic field change also shows up as the hysteresis in the PHE signal [Figs. 6.1(i) and (j)]. The PHE anomaly is more prominent in the course of increasing field than decreasing field at 2 K [Fig. 6.1(i)]. Since the magnitude of the PHE anomaly should be associated with the skyrmion density, the large hysteresis in PHE indicates that the density of packed skyrmion strings depends on the precedented magnetic structure determined by the magnetic field history; the helical structure is more prone to the development of the skyrmions than the ferromagnetic state. With a slight elevation of temperature from 2 K, for example at 10 K, skyrmion formation occurs in different B-ranges between the increasing and decreasing field processes [Fig. 6.1(j)]. With increasing field, the transformation of the in-plane skyrmion strings from the helical structure occurs at B_{sk1}, followed by the continued existence of skyrmions well above B_{c}; with decreasing field, skyrmions appear at B_{c}, remaining even near zero field. Here we note that while there are also discerned kinks and/or hysteretic behaviors corresponding to the skyrmion phase in the magnetization and magnetoresistivity curves, the planar Hall signal shows much better sensitivity for the skyrmion formation.

We show contour mapping of $\rho_{yx}^{\mathrm{PHE}}/\rho_{xx}(0)$ for the increasing field process in Fig. 6.2(a), along with phase boundaries determined by measurements of M and PHE. In contrast to the skyrmion phase in the bulk MnSi as stabilized by the large thermal fluctuations near T_{c}, the in-plane skyrmion phase for the thin film appears at low temperatures; this indicates a different driving force is involved in the formation of the in-plane skyrmions. The uniaxial magnetic anisotropy enhanced at low temperatures is perhaps the major contribution as theoretically suggested [100]. To highlight the hysteretic formation of the in-plane skyrmion, we map in Fig. 6.2(b) the $\Delta\rho_{yx}^{\mathrm{PHE,\,Hys}}$ defined as difference calculated by subtracting ρ_{yx}^{PHE} with decreasing field from that with increasing field, which removes the M-induced PHE showing a significant contribution above B_{c} between 20–50 K. As described above, the in-plane skyrmion formation largely depends on the magnetic

field history; namely, skyrmions tend to coexist with the ferromagnetic (helical) state in the increasing (decreasing) field process. That hysteretic behavior is presented as positive [blue part in Fig. 6.2(b)] or negative [red part in Fig.6.2(b)] $\Delta\rho_{yx}^{\mathrm{PHE,\,Hys}}$, while there is no hysteretic signal in the other T-H region. We note that the magnetic phase diagram determined by PHE is different from that of previous study [100] based on the magnetization measurement.

Finally, we discuss the thickness (t) dependence of planar Hall signal (Fig. 6.3). At low temperatures, where we demonstrate the in-plane skyrmion formation, a polarized neutron reflectometry study [101] has proposed a helicoidal state. The helicoidal state proposed in Ref. [101] shows discrete changes in its helix turns with a magnetic field variation. When the sample thickness is $n\lambda \leq t < (n+1)\lambda$, where λ is helical period, the helicoidal state with n-turns is realized. With application of the magnetic field, the turns would be discretely unwound. If we assume the large kink in PHE [e.g. see Fig. 6.1(i)] originates from the helicoidal structure, namely the discrete change in the number of turns, additional kink would appear in a thicker film. Figure 6.3 shows that the PHE signals in 26 and 50-nm thick films. Even if we increase the thickness twice, the overall feature remains unchanged; this is inconsistent with the model of the helical structure formation, but supports the present interpretation, i.e. the in-plane skyrmion formation.

6.3 Stability of two-dimensional skyrmions investigated by topological Hall effect

In this section, we investigate the stability of skyrmions in MnSi thin films with various film thickness and helical period, the latter of which can be controlled by Fe content x, when an out-of-plane magnetic field is applied by using topological Hall effect. The magnetic and transport properties of present films are in good
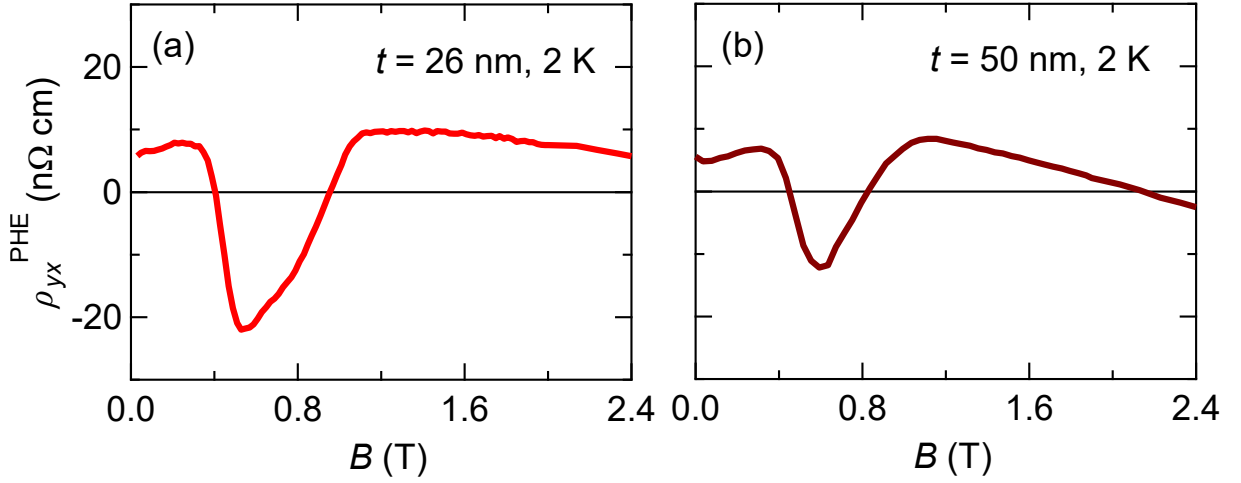
Figure 6.3: Magnetic-field dependence of ρ_{yx}^{PHE} at 2K in (a) 26 nm film and (b) 50 nm film.

agreement with previous reports[102, 103]. Magnetic transition temperatures of the 20-nm films are presented along with those of the bulk for comparison in Fig. 6.5(c). The transition temperatures (T_{c}) were determined from the inflection points in the M-T curves (Figs. 6.4) by adopting the peaks of second T-derivative of magnetization M under an out-of-plane field of 0.05 T. The transition temperatures T_{c} of the $Mn_{1-x}Fe_xSi$ films are higher approximately by 10 K than those of bulk due to the strain from the Si substrate, yet they do not depend on film thickness (not shown), as already recognized in previous studies [102, 103]. Figures 6.5(a) and (b) show the temperature dependence of resistivity ρ_{xx} for all the $Mn_{1-x}Fe_xSi$ films. The resistivity shows an inflection corresponding to the magnetic transition. The residual resistivity decreases with t because of reduction of the surface scatting [Fig. 6.5(a)], while increasing with x due to scattering by Fe dopants [Fig. 6.5(b)].

Shown in Figs. 6.6(a)-(c), Figs. 6.6(d)-(f), and Fig. 6.7 are the magnetic-field dependences of magnetization M, magnetoresistivity $\rho_{xx}(B)/\rho_{xx}(0)$, and Hall resistivity ρ_{yx} of 20-nm $Mn_{1-x}Fe_xSi$ films, respectively, from which we extract the
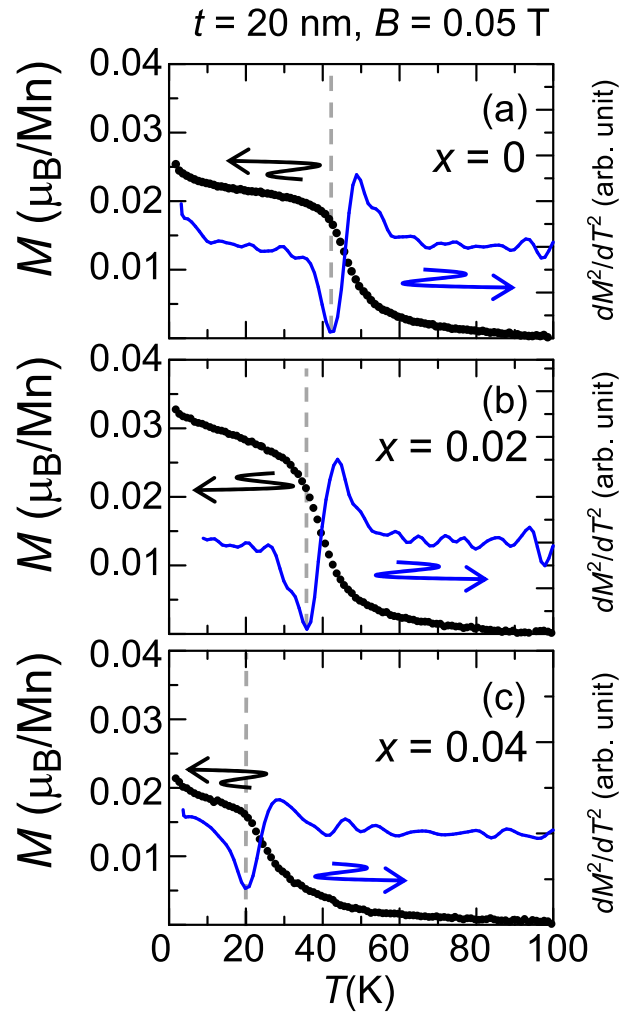
Figure 6.4: (a)-(c) Temperature dependence of magnetization and its second derivative of 20-nm $Mn_{1-x}Fe_xSi$ films ($x = 0$, 0.02, and 0.04) at $B = 0.05$ T.
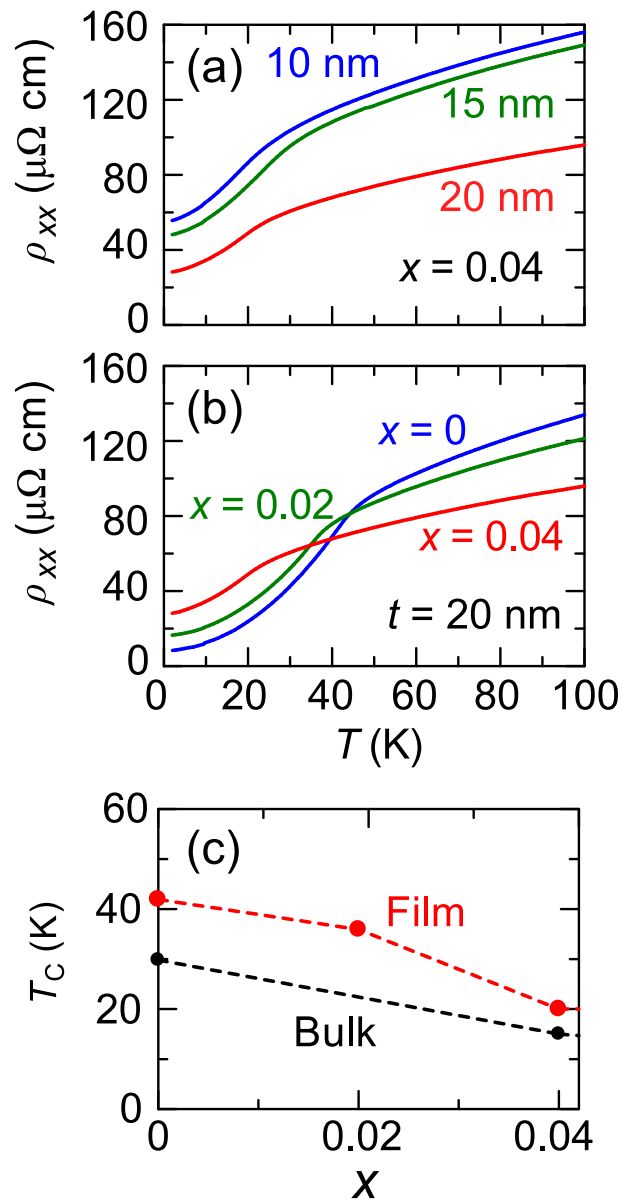
Figure 6.5: Comparison between T-dependences of resistivities of (a) $Mn_{0.96}Fe_{0.04}Si$ films with different thicknesses and (b) 20-nm $Mn_{1-x}Fe_xSi$ films with different Fe contents. (c) The transition temperature T_c of 20-nm $Mn_{1-x}Fe_xSi$ films compared with those of bulk samples.[104]

topological Hall signals as described below. The transition between the wind-ing (helical, conical, skyrmionic, etc.) magnetic structure and the ferromagnetic structure is represented as the inflection in the M-B curve, the magnetic field at which is defined as B_{c} by adopting the peak of first B-derivative of M. The observed profiles of ρ_{yx} indicate additional contributions other than the B-linear and M-linear terms of the respective normal and anomalous Hall effects.
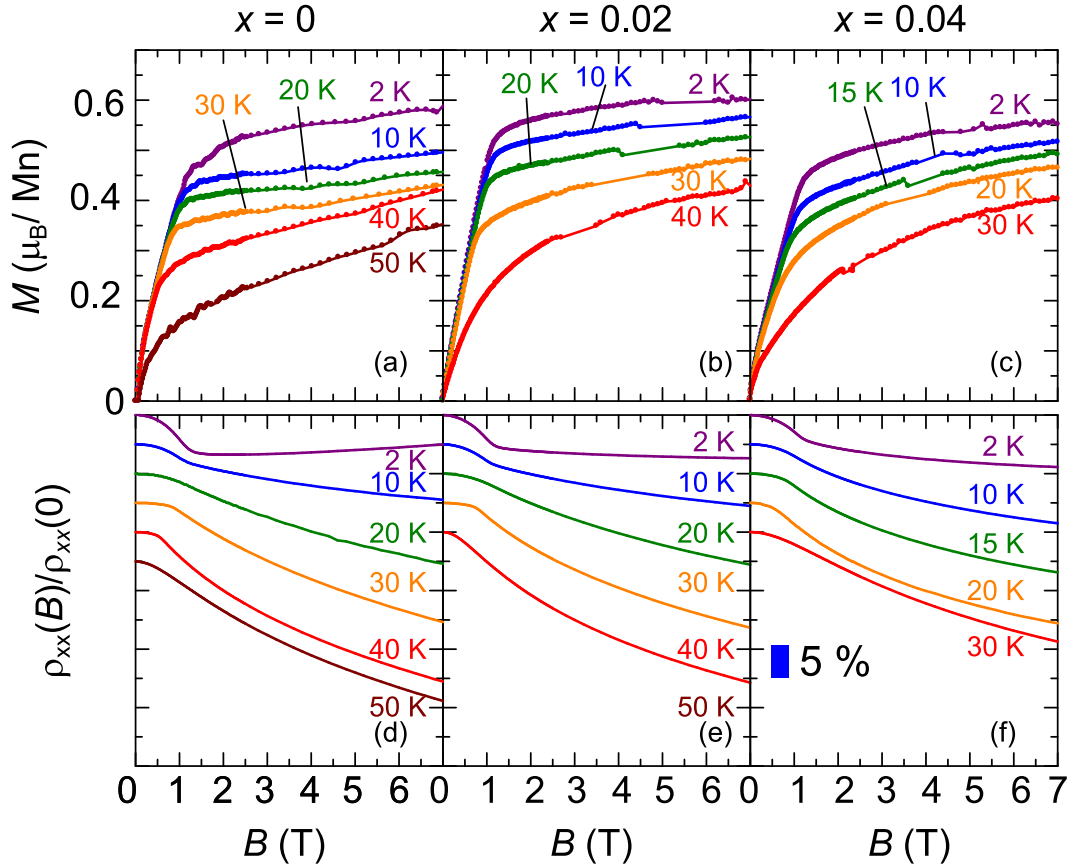
Figure 6.6: (a)-(f) Magnetic-field dependence of magnetization and magnetoresis-tivity of 20-nm $\mathrm{Mn}_{1-x}\mathrm{Fe}_x\mathrm{Si}$ films ($x = 0$, 0.02, and 0.04). In panels (a)-(c), the diamagnetic contribution of Si substrate estimated by the M-B curve at 300 K is subtracted from the raw data.

In general, the topological Hall contribution is less distinguishable when the ρ_{yx}-B curve deviates from the straight line due to other origins such as the mul-
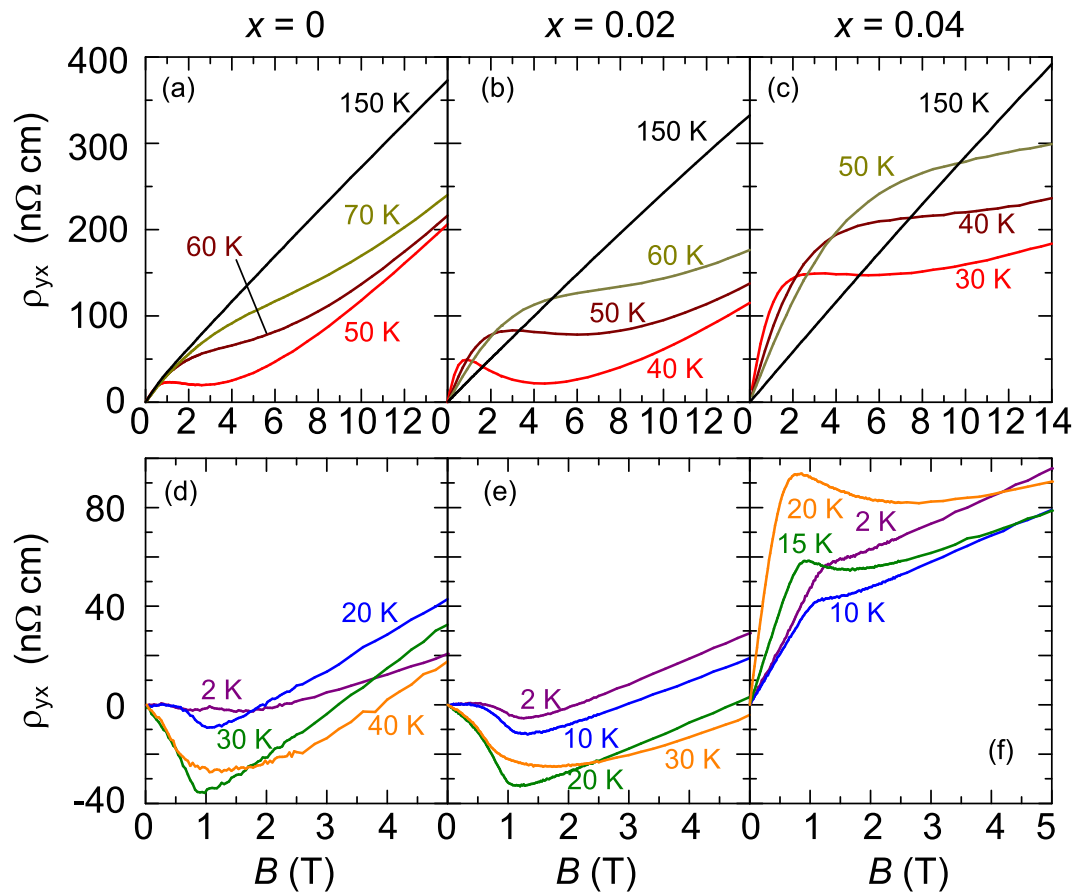
Figure 6.7: (a)-(f) Magnetic-field dependence of Hall resistivity of 20-nm $Mn_{1-x}Fe_xSi$ films ($x = 0$, 0.02, and 0.04).

ticarrier effect on the ordinary Hall response [105]. To distinguish topological Hall signals from possible other contributions, we measured the inclination angle dependence of Hall resistivity. Here we define the inclination angle θ as the angle between the normal vector to the film plane and the magnetic field direction [see inset of Fig. 6.8(a)]. Figures 6.8(a)-(d) present Hall resistivity of the $\mathrm{Mn}_{1-x}\mathrm{Fe}_x\mathrm{Si}$ film ($t = 20$ nm, $x = 0.04$) at various values of θ. We adopt the two-carrier model of normal Hall effect [105] and analyze $\rho_{yx}(\theta)$ by employing the following relations:[34, 106]

$$
\begin{aligned}
\rho_{yx} &= \rho_{yx}^{\mathrm{N}} + \rho_{yx}^{\mathrm{A}} + \rho_{yx}^{\mathrm{T}}, \\
\rho_{yx}^{\mathrm{N}} &= \frac{R_1\rho_2^2 + R_2\rho_1^2 + R_1R_2(R_1 + R_2)(H\cos\theta)^2}{(\rho_1 + \rho_2)^2 + (R_1 + R_2)^2(H\cos\theta)^2}H\cos\theta, \\
\rho_{yx}^{\mathrm{A}} &= S_H\rho_{xx}(\theta)^2 M(\theta)\cos\theta.
\end{aligned}
\tag{6.1}
$$

Here, ρ_{yx}^{N} and ρ_{yx}^{A} are the normal and the anomalous Hall resistivities, respectively. R_1 (R_2) and ρ_1 (ρ_2) are normal Hall coefficient and resistivity of each carrier. S_H is anomalous Hall coefficient. In this model, the normal Hall resistivity ρ_{yx}^{N} does not obey B-linear dependence except for high field regime ($\rho_{yx}^{\mathrm{N}} \to [R_1R_2/(R_1 + R_2)]H\cos\theta$). The measured Hall resistivity converges with the B-linear profile at high fields, where the ferromagnetic (spin-collinear) state is induced and the topological Hall effect disappears. This enables us to reproduce the experimental data in the high field by using a simple relation $\rho_{yx} = \rho_{yx}^{\mathrm{N}} + \rho_{yx}^{\mathrm{A}} = R_\theta H + S_\theta\rho_{xx}(\theta)^2 M(\theta)$, where $R_\theta = \frac{R_1R_2}{R_1+R_2}\cos\theta$ and $S_\theta = S_H\cos\theta$. Magnetoresistivity $\rho_{xx}(\theta)$ and magnetization $M(\theta)$ were measured at every angle (not shown). Sum of the B-nonlinear contributions from the multicarrier effect and the topological Hall effect can be extracted as the difference between the measured Hall resistivity ρ_{yx} and the fitted curve, which we denote by $\Delta\rho_{yx}$ [see Figs. 6.8(a)-6.8(d) for the fitting].

Figures 6.9(a)-(d) show development of $\Delta\rho_{yx}$ at various inclination angles, plotted as a function of the effective magnetic field perpendicular to the film plane ($B\cos\theta$) normalized by B_{c}. Below the transition temperature T_{c} ($T = 10$, 15, and
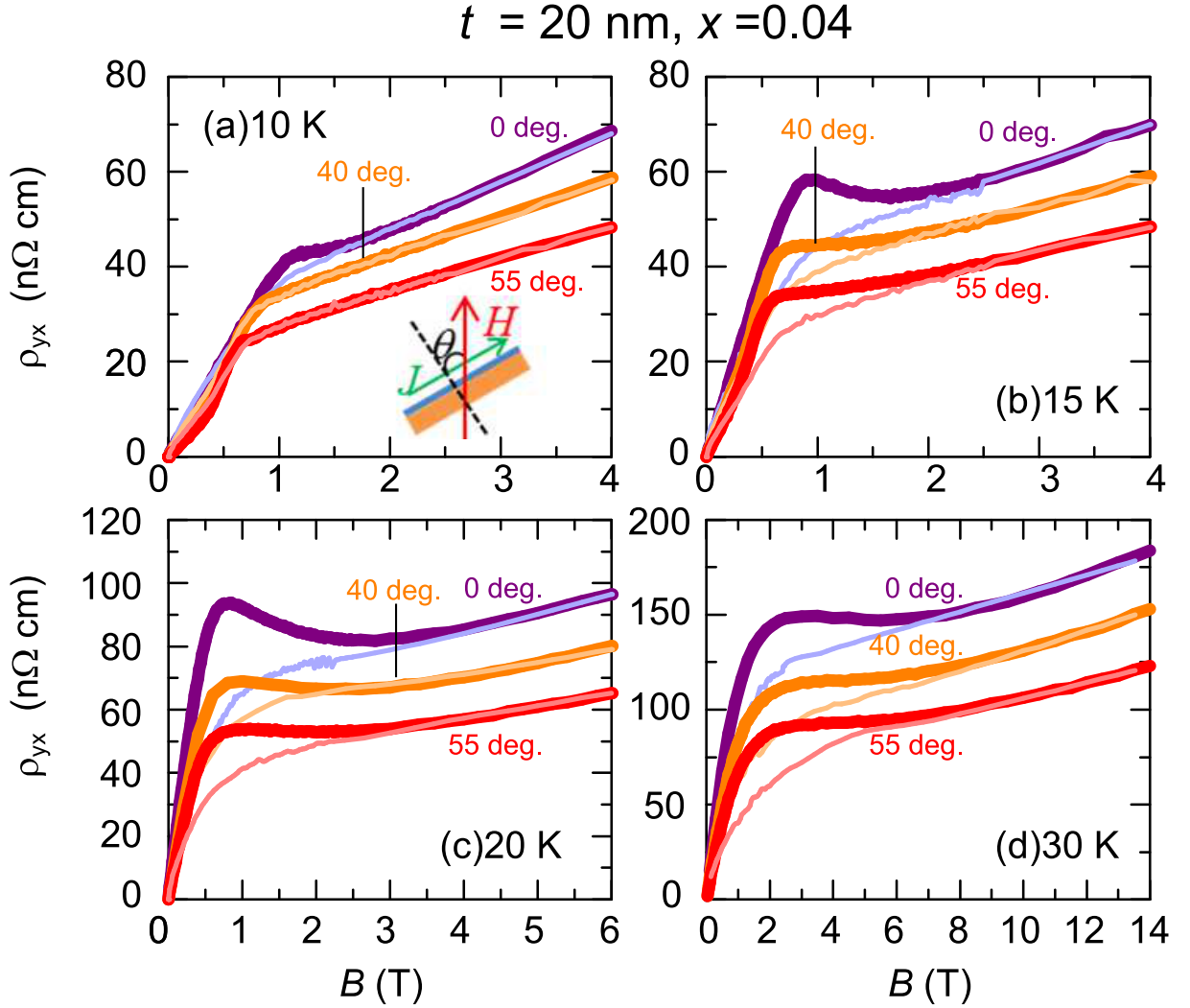
Figure 6.8: Magnetic-field dependence of (a)-(d) Hall resistivity ρ_{yx} of the Mn$_{1-x}$Fe$_x$Si film ($t = 20$ nm, $x = 0.04$) at various inclination angles and temperatures. Thick lines show the measured ρ_{yx}, and thin lines are fitting curves for high magnetic fields ($H \gg B_c$), using the relation that $\rho_{yx} = R_\theta B + S_\theta \rho_{xx}^2 M$ (see text). The inset of panel (a) is a sketch of the experimental setup.

20 K), the $\Delta\rho_{yx}$ shows a sudden decrease around $\theta = 30°$ with increasing θ, and it converges with a dome-shaped profile at the larger angles ($\theta = 40°$ and $55°$), which indicates a sharp change in the magnetic structure around $\theta = 30°$-$40°$ [Figs.
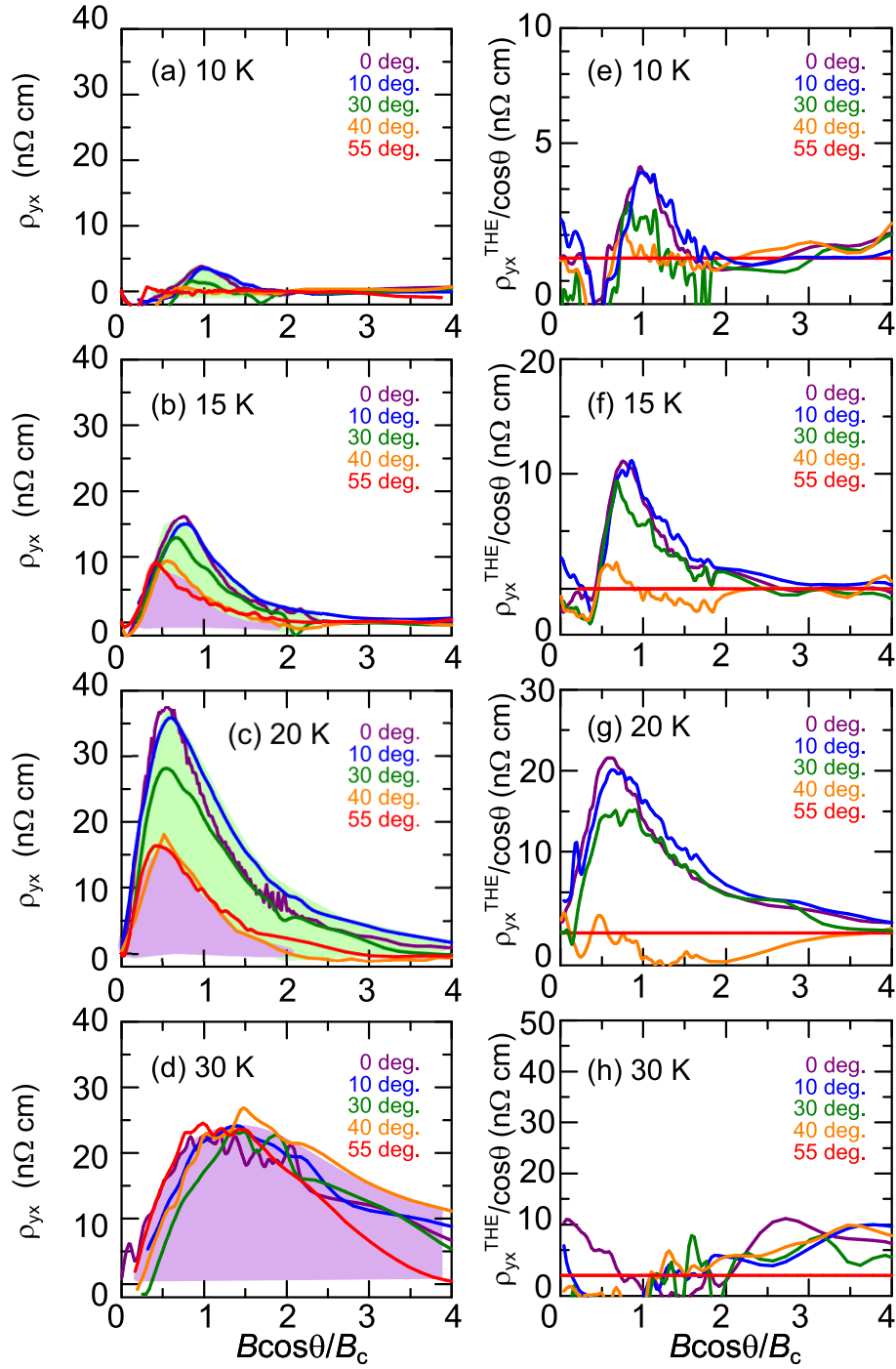
Figure 6.9: Magnetic-field dependence of (a)-(d) $\Delta\rho_{yx}$, and (e)-(h) $\rho_{yx}^{\mathrm{T}}/\cos\theta$ of the $\mathrm{Mn}_{1-x}\mathrm{Fe}_x\mathrm{Si}$ film ($t = 20$ nm, $x = 0.04$) at various inclination angles and temperatures (see text for the definitions of $\Delta\rho_{yx}$ and topological component ρ_{yx}^{T}). The green and the purple shadowed parts in panels (a)-(d) show the contribution from topological Hall effect and multicarrier effect, respectively

6.9(a)-(c)]. Conversely, the $\Delta\rho_{yx}$ remains as the same curve at every inclination angle above T_c [Fig. 6.9(d)]. We assign the drop of $\Delta\rho_{yx}$ observed below T_c to the disappearance of topological Hall contribution ρ_{yx}^T due to the destruction of the skyrmions by tilting the sample with respect to the magnetic field direction. The convergent curves of $\Delta\rho_{yx}$ observed both above and below the transition tempera- ture are the B-nonlinear component arising from the multicarrier effect on ρ_{yx}^N. We show variation of the extracted ρ_{yx}^T at various angles in Figs. 6.9(e)-6.9(h). The ex- tracted ρ_{yx}^T is defined as $\rho_{yx}^T(B\cos\theta,\theta) = \Delta\rho_{yx}(B\cos\theta,\theta) - \Delta\rho_{yx}(B\cos\theta,\theta = 55°)$. Given this assignment of the topological Hall effect, we can know a critical an- gle of the skyrmion formation itself; we normalize the ρ_{yx}^T (proportional to the skyrmion density) by $\cos\theta$ because the spacing between skyrmions is elongated, by a factor of $1/\cos\theta$ along the current path with tilting the sample [also see Fig. 6.11 (b)]. The sharp decline of ρ_{yx}^T, reflecting the annihilation of non-coplanar magnetic structures like skyrmions, is again highlighted at the temperatures be- low T_c [Fig. 6.9(e)-(g)], while no topological Hall contribution is observed above T_c [Fig. 6.9(h)]. The critical angle is revealed to be around $\theta = 30°$ (Fig. 6.10).
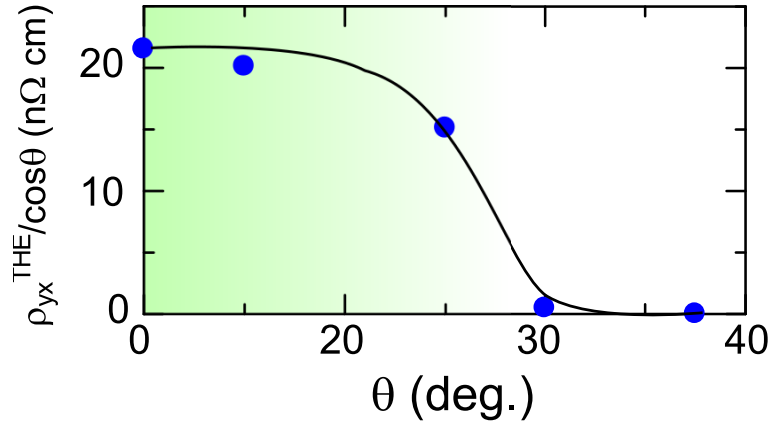
Figure 6.10: Peak values of topological Hall resistivity at 20 K normalized by $\cos\theta$ in the 20-nm $Mn_{0.96}Fe_{0.04}Si$ film as a function of the inclination angle θ.

We map the skyrmion phases for all the $Mn_{1-x}Fe_xSi$ films by projecting the
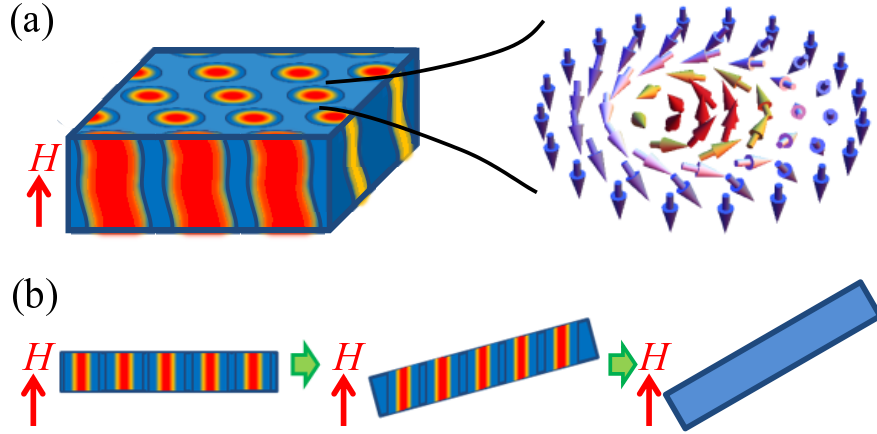
Figure 6.11: Schematic illustrations of (a) a bird's-eye view and (b) side views of a triangular lattice of skyrmions in a thin-plate formed sample. In each pillar structure, a vortex-like spin texture as indicated by hue-colored arrows stretches along a magnetic field. Red (blue) parts correspond to the areas where spins point parallel (anti-parallel) to the magnetic field. When the normal vector to the thin plate is inclined at a certain angle from the magnetic field, the skyrmion lattice is no longer stable and the conical spin structure with a uniform spin component along the field appears instead.

extracted ρ_{yx}^{T} on the T-B plane [Figs. 6.12(a)-(e)]. The topological Hall resistivity, essentially representing the skyrmion density, gradually varies with T and B, and shows a maximum around the transition temperature T_{c}. This feature is common to all the $\mathrm{Mn}_{1-x}\mathrm{Fe}_x\mathrm{Si}$ thin films, which is in good agreement with previous reports of LTEM observation of thinned plate samples of $B20$-type compounds [8, 17, 98].

Among the $\mathrm{Mn}_{0.96}\mathrm{Fe}_{0.04}\mathrm{Si}$ films with different thicknesses ($t = 10$, 15, and 20 nm), the temperature range of the dense-skyrmion phases (ΔT_{sk}), as defined by the regions where $\rho_{yx}^{\mathrm{T}} > 6$ nΩ cm, shrink with increasing thickness (t) [Figs. 6.12(a)-(c)]. By contrast, among the 20-nm films with different Fe contents ($x = 0$, 0.02,

and 0.04), ΔT_{sk} is also reduced with doping Fe [Figs. 6.12(c)-(e)]. The helical period perhaps becomes shorter with doping Fe as observed for the corresponding bulk system [107]. Thus, the helical period as well as the sample thickness are the primary parameters which determine the width of ΔT_{sk}, or the skyrmion stability.

The topological Hall effect was also detected above T_{c} and above B_{c}, which indicates some spin structure endowed with the non-vanishing topological charge (scalar spin chirality) still remains in those regions. As mentioned above, in bulk sample of MnSi, the chiral nature of spin structure still remains above T_{c} (chiral spin fluctuations). However, in general, a spin structure with chiral spin fluctuations does not necessarily possess nonzero scalar spin chirality, and existence of nonzero scalar spin chirality above T_{c} in bulk MnSi is controversial.

6.4   Summary

In this section, we investigate stability of skyrmions in thin films, employing (1) planar Hall effect to detect the formation of in-plane skyrmion and (2) topological Hall effect to detect the quasi-two-dimensional skyrmion.

By measurements of planar Hall effect (PHE), we have revealed the formation of the in-plane skyrmions in the MnSi epitaxial thin films, which can hardly be detected by the conventional detection methods such as Lorentz TEM and topological Hall effect. PHE sensitively detects the 90°-flop of the magnetic modulation associated with the skyrmion formation and destruction, showing the prominent stepwise anomaly in the skyrmion phase. We could determine the development of the respective magnetic texture in the MnSi film under the in-plane magnetic field, including the hysteretic formation of the in-plane skyrmions against the magnetic field change. The uniaxial magnetic anisotropy due to the strain is likely the cause of the in-plane skyrmion formation at low temperatures.

Quasi-two-dimensional skyrmion phases is determined by mapping the magnitude of topological Hall resistivity in the T-B plane. We could identify the
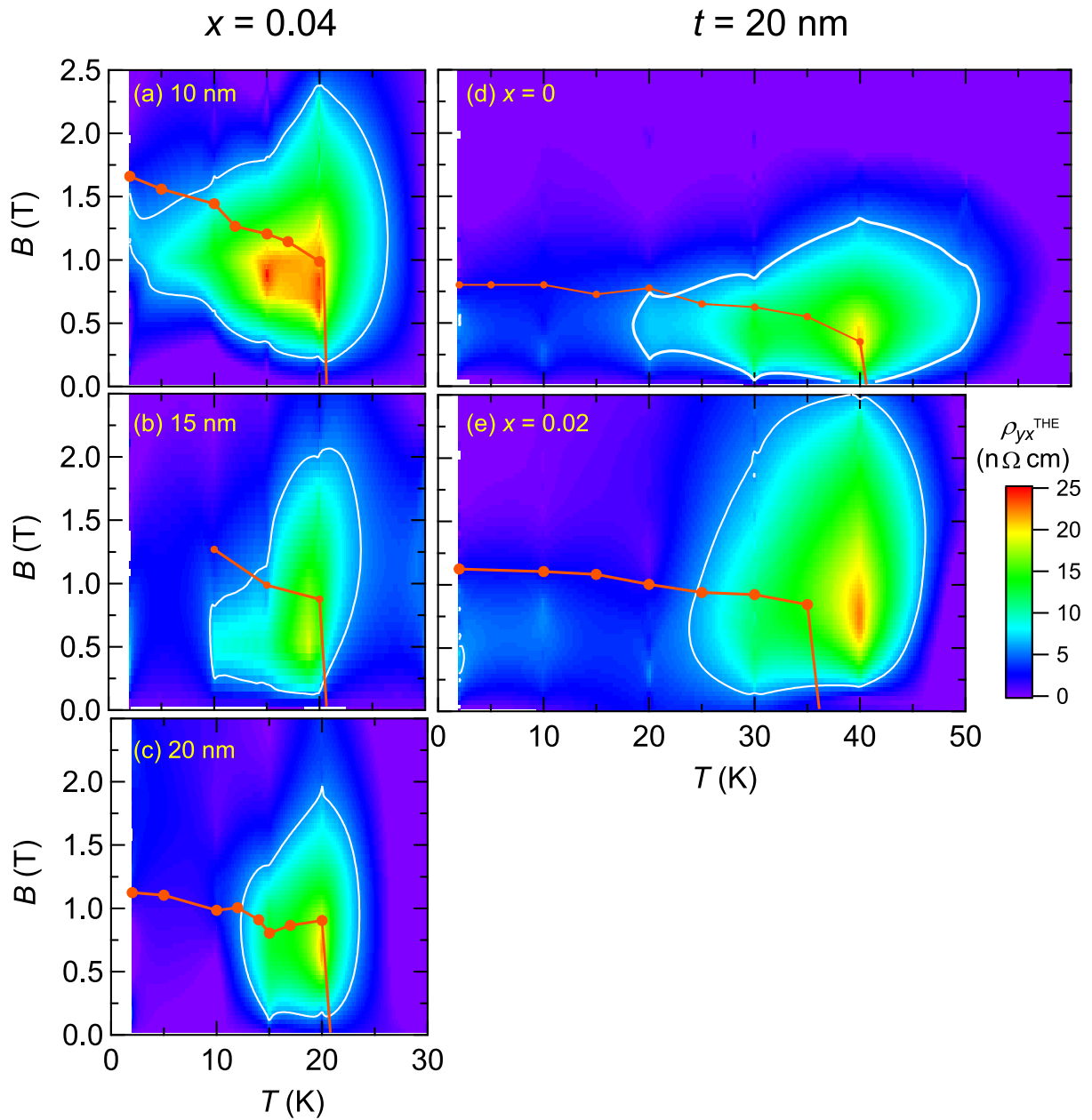
Figure 6.12: (a)-(e) Color maps of topological Hall resistivity in the T-B plane for $Mn_{1-x}Fe_xSi$ films. Compare panels (a)-(c) [panels (c)-(e)] for thickness (helical-period) dependence of skyrmion phase. White lines are contour lines indicating $\rho_{yx}^{T} = 6$ nΩ cm. Orange dots represent B_c.

topological Hall effect from the B-nonlinear normal Hall effect by studying the change of Hall resistivity at various inclination angles of applied magnetic field. The sharp reduction in some part of Hall anomaly, which represents the disappearance of the topological Hall contribution likely associated with the destruction of quasi-two-dimensional skyrmion structures, was observed in the process of inclining the magnetic field. The mapped skyrmion phases show the systematic change in ΔT_{sk} (skyrmion-stable temperature range) against the thickness (t) relative to helical period (λ), ensuring the more robust skyrmion phase in the lower t/λ system [17]. The number of quasi-two-dimensional skyrmions reaches a maximum near T_{c}, which differ from the phase diagram for the in-plane skyrmion. These results indicate the dominant mechanisms of the stabilization for the in-plane skyrmion and the quasi-two-dimensional skyrmions are different; the former is uniaxial strain and the letter is dimensionality.

Chapter 7

Conclusion

In this Chapter, we summarize the results to conclude this thesis and discuss perspectives. In this thesis, we have investigated transport phenomena in which both chiral and topological properties of skyrmion and chiral spin structures play a crucial role.

In Chapter 3, we investigate anisotropic magnetoresistance originating from the modulation of chiral spin structures in bulk samples of MnSi, focusing on planar Hall effect, which is a sensitive probe for anisotropic magnetoresistance. Planar Hall effect sensitively detects the 90°-flop of the magnetic modulation associated with the skyrmion formation and destruction, showing the prominent stepwise anomaly in the skyrmion phase. This finding provides a new underlying principle for the establishment of a method to detect skyrmion formation.

In Chapter 4 and 5, we focused on the nonreciprocal transport phenomena, which are allowed in the non-centrosymmetric system from the viewpoint of symmetry. In Chapter 4, we have investigated the electrical magnetochiral effect (eMChE), which is nonreciprocal magnetotransport effect with the resistance proportional to the inner product of magnetic field and current. Prominent eMChE signals emerge at specific temperature-magnetic field-pressure regions: in the paramagnetic phase just above the helical ordering temperature and in the partially-

ordered topological spin state at low temperatures and high pressures. Electrical magnetochiral effect is also discerned at the phase boundary of the equilibrium skyrmion phase and in the amorphous-like metastable skyrmion phase. These results indicate the close relationship between eMChE and fluctuations and/or disorders of chiral spin structures.

In chapter 5, we have demonstrated that the current-induced asymmetric deformation of skyrmion strings arising from both its flexible nature and the Dzyaloshinskii-Moriya interaction results in nonreciprocal Hall effect related to emergent electric field. The asymmetric dynamics and consequent nonreciprocal transport response are one of the generic properties of dynamics of string-like objects in non-centrosymmetric systems including vortex lines in non-centrosymmetric superconductors as well as skyrmion string in nonsymmetric mangets investigated here.

In Chapter 6, we have investigated stability of skyrmion against both in-plane and out-of-plane magnetic field in thin films by using transport measurements. When in-plane magnetic field is applied, in-plane skyrmions, which is an array of skyrmion strings stretching in the plane of the thin films, are stabilized at low temperatures. In contrast, when out-of-plane magnetic field is applied, the quasi-two-dimensional skyrmion are most stabilized in the vicinity of $T_{\rm c}$. These results indicate the dominant mechanisms of the stabilization for the in-plane skyrmion and the quasi-two-dimensional skyrmions are different; the former is uniaxial strain and the letter is the dimensionality.

Finally, we discuss perspectives. We have revealed that the coupling between conduction electrons and spin structures with nontrivial topology and/or chirality gives birth to nonreciprocal and current-nonlinear transport responses.These phenomena are expected to widely occur in chiral spin systems other than $B20$-type MnSi. In addition, in helimagnets with centrosymmetric structure, although right- and left-handed spin structures are energetically degenerate, the nonreciprocal transport phenomena are allowed in a homochiral domain. Furthermore, the

nonreciprocal transport phenomena and asymmetric skyrmion strings dynamics investigated here also provide insight into those in other non-centrosymmetric systems such as polar magnets or bilayer films, in which nonreciprocal phenomena with the selection rule which differs from that in the chiral system are allowed. Moreover, the coupling between pure spin current, and chirality and topology of spin structures is also of great interest.

To realize skyrmion-based devices, the stabilization of skyrmion in thin films at room temperature is essential. Basic mechanisms for stabilizing skyrmions in thin films of chiral magnets discussed in this thesis provide design guidelines for thin films of chiral magnets hosting skyrmion above room temperature such as Co-Zn-Mn alloys.

Bibliography

[1] L. D. Barron, Chirality **24**, 879 (2012).

[2] Y. Tokura, S. Seki, N. Nagaosa, Rep. Prog. Phys.**77**, 076501 (2014).

[3] Y. Tokura, M. Kawasaki, N. Nagaosa, Nat. Phys. **13**, 1056 (2017).

[4] N. Nagaosa, and Y. Tokura, Nature Nanotech. **8**, 899 (2013).

[5] A. Fert, V. Cros, and J. Sampaio Nature Nanotech. **8**, 152 (2013).

[6] A. N. Bogdanov, and D. A. Yablonskii, Sov. Phys. JETP **68,** 101 (1989).

[7] S. Mühlbauer, B.Binz, F. Jonietz, C.Pleiderer, A. Rosch, A. Neubauer, R. Georgii, and P. Böni, Science **323,** 915 (2009).

[8] X. Z. Yu, Y. Onose, N. Kanazawa, J. H. Park, J. H. Han, Y. Matsui, N. Nagaosa, and Y. Tokura, Nature **465,** 901 (2010).

[9] T. Okubo, S. Chung, and H. Kawamura, Phys. Rev. Lett. **108**, 017206 (2012).

[10] A. O. Leonov and M. Mostovoy, Nat. Commun. **6**, 8275 (2015).

[11] S. Hayami, Shi-Zeng Lin, and C. D. Batista, Phys. Rev. B **93**, 184413 (2016).

[12] S. Heinze, K. von Bergmann, M. Menzel, J. Brede, A. Kubetzka, R. Wiesendanger, G. Bihlmayer and S. Blügel, Nature Phys. **7**, 713－718 (2011).

[13] H. S. Park, X. Z. Yu, S. Aizawa, T. Tanigaki, T. Akashi, Y. Takahashi, T. Matsuda, N. Kanazawa, Y. Onose, D. Shindo, A. Tonomura, and Y. Tokura, Nat. Nanotechnol. **9**, 337 (2014).

[14] W. Münzer, A. Neubauer, T. Adams, S. Mühlbauer, C. Franz, F. Jonietz, R. Georgii, P. Böni, B. Pedersen, M. Schmidt, A. Rosch, and C. Pfleiderer, Phys. Rev. B **81,** 041203 (2010).

[15] S. Seki, X. Z. Yu, S. Ishiwata, and Y. Tokura, Science **336,** 198 (2012).

[16] Y. Tokunaga, X. Z. Yu , J. S. White, H. M. Rnnow, D. Morikawa, Y. Taguchi, and Y. Tokura, Nat. Commun. **6**, 7638 (2015).

[17] X. Z. Yu, N. Kanazawa, Y. Onose, K. Kimoto, W. Z. Zhang, S. Ishiwata, Y. Matsui, and Y. Tokura, Nat. Mater. **10,** 106 (2011).

[18] R. Ritz, M. Halder, C. Franz, A. Bauer, M. Wagner, R. Bamler, A. Rosch, and C. Peiderer, Phys. Rev. B **87**, 134424 (2013).

[19] H. Oike, A. Kikkawa, N. Kanazawa, Y. Taguchi, M. Kawasaki, Y. Tokura and F. Kagawa, Nat. Phys. **12**, 62 (2016).

[20] K. Karube, J. S. White, N. Reynolds, J. L. Gavilano, H. Oike, A. Kikkawa, F. Kagawa, Y. Tokunaga, H. M. Rnnow, Y. Tokura, and Y. Taguchi. Nat. Mat. **15**, 1237 (2016).

[21] T. Nakajima, H. Oike, A. Kikkawa, E. P. Gilbert, N. Booth, K. Kakurai, Y. Taguchi, Y. Tokura, F. Kagawa, and T. Arima, Sci. Adv. **3**, 1602562 (2017).

[22] G. Shirane, R. Cowley, C. Majkrzak, J. B. Sokoloff, B. Pagonis, C. H. Perry, Y. Ishikawa, Phys. Rev. B **28**, 6251 (1983).

[23] S. V. Grigoriev, S. V. Maleyev, A. I. Okorokov, Yu. O. Chetverikov, R. Georgii, P. Bni, D. Lamago, H. Eckerlebe, K. Pranzas, Phys. Rev. B **72**, 134420 (2005).

[24] C. Pappas, E. Lelivre-Berna, P. Falus, P. M. Bentley, E. Moskvin, S. Grigoriev, P. Fouquet, B. Farago, Phys. Rev. Lett. **102**, 197202 (2009).

[25] S. V. Grigoriev, S. V. Maleyev, E. V. Moskvin, V. A. Dyadkin, P. Fouquet, H. Eckerlebe, . Phys. Rev. B **81**, 144413 (2010).

[26] M. Blume, Phys. Rev. **130** 1670, (1963).

[27] C. Pfleiderer, D. Reznik, L. Pintschovius, H. v. Löhneysen, M. Garst, A. Rosch, Nature **427**, 227 (2004).

[28] Y. J. Uemura, T. Goko, I. M. Gat-Malureanu, J. P. Carlo, P. L. Russo, A. T. Savici, A. Aczel, G. J. MacDougall, J. A. Rodriguez, G. M. Luke, S. R. Dunsiger, A. McCollam, J. Arai, Ch. Pfleiderer, P. Böni, K. Yoshimura, E. Baggio-Saitovitch, M. B. Fontes, J. Larrea, Y. V. Sushko, J. Sereni, Nature Phys. **3**, 29 (2007).

[29] R. Ritz, M. Halder, M. Wagner, C. Franz, A. Bauer, C. Pfleiderer, Nature **497**, 231 (2013).

[30] Y. Togawa, T. Koyama, K. Takayanagi, S. Mori, Y. Kousaka, J. Akimitsu, S. Nishihara, K. Inoue, A. S. Ovchinnikov, and J. Kishine, Phys. Rev. Lett. **108**, 107202 (2012).

[31] Y. Togawa, Y. Kousaka, K Inoue, and J. Kishine, J. Phys. Soc. Jap. **85**, 112001 (2016).

[32] M. N. Wilson, E. A. Karhu, D. P. Lake, A. S. Quigley, S. Meynell, A. N. Bogdanov, H. Fritzsche, U. K. Rößler , and T. L. Monchesky, Phys Rev. B. **88**, 214420 (2013).

[33] N. Kanazawa, J. S. White, H. M. Rnnow, C. D. Dewhurst, Y. Fujishiro, A. Tsukazaki, Y. Kozuka, M. Kawasaki, M. Ichikawa, F. Kagawa, and Y. Tokura, Phys. Rev. B **94**, 184432 (2016).

[34] N. Kanazawa, Y. Onose, T. Arima, D. Okuyama, K. Ohoyama, S. Wakimoto, K. Kakurai, S. Ishiwata, and Y. Tokura, Phys. Rev. Lett. **106,** 156603 (2011).

[35] N. Kanazawa, J.-H. Kim, D. S. Inosov, J. S. White, N. Egetenmeyer, J. L. Gavilano, S. Ishiwata, Y. Onose, T. Arima, B. Keimer, and Y. Tokura Phys. Rev. B **86**, 134425 (2012).

[36] N. Kanazawa, Y. Nii, X.-X. Zhang, A.S. Mishchenko, G. De Filippis, F. Kagawa, Y. Iwasa, N. Nagaosa, and Y. Tokura, Nat. Commun. **7**, 11622 (2016).

[37] M. V. Berry, Proc. R. Soc. Lond. A **392,** 45 (1984).

[38] D. Xiao, Ming-Che Chang, and Q. Niu, Rev. Mod. Phys. **82**, 1959 (2010).

[39] E. H. Hall, Phil. Mg. **12,** 157 (1881).

[40] N. Nagaosa, J. Sinova, S. Onoda, A. H. MacDonald, and N. P. Ong, Rev. Mod. Phys. **82,** 1539 (2010).

[41] S. Onoda, N. Sugimoto,and N. Nagaosa, Phys. Rev. B **77,** 165103 (2008).

[42] R. Karplus, and J. M. Luttinger, Phys. Rev. **95,** 1154 (1954).

[43] T. Jungwirth, Qian Niu, and A. H. MacDonald, Phys. Rev. Lett. **88**, 207208 (2002).

[44] M. Onoda and N. Nagaosa, J. Phys. Soc. Jpn. **71,** 19 (2002).

[45] K. Ohgushi, S. Murakami, and N. Nagaosa, Phys. Rev. B **62**, R6065 (2000)

[46] J. Ye, Y. B. Kim, A. J. Millis, B. I. Shraiman, P. Majumdar, and Z. Tesanovic, Phys. Rev. Lett. **83,** 3737 (1999).

[47] M. Onoda, G. Tatara, and N. Nagaosa, J. Phys. Soc. Jpn. **73,** 2624 (2004).

[48] P. Bruno, V. K. Dugaev, and M. Taillefumier, Phys. Rev. Lett. **93,** 096806

[49] A. Neubauer, C. Pfleiderer, B. Binz, A. Rosch, R. Ritz, P. G. Niklowitz, and P. Böni, Phys. Rev. Lett. **102,** 186602 (2009).

[50] C. Franz, F. Freimuth, A. Bauer, R. Ritz, C. Schnarr, C. Duvinage, T. Adams, S. Blgel, A. Rosch, Y. Mokrousov, and C. Pfleiderer Phys. Rev. Lett **112**, 186601 (2014).

[51] F. Jonietz, S. Mühlbauer, C. Pfleiderer, A. Nuebauer, W.Münzer, A. Bauer, T. Adams, R. Georgii, P. Böni, R. A. Duine, K. Evershor, M. Garst, and A. Rosch, Science **330,** 1648 (2010).

[52] T.Schulz, R. Ritz, A. Bauer, M. Halder, M. Wagner, C. Franz, C. Pfleiderer, K. Everschor, M. Garst, and A. Rosch, Nat. Phys. **8,** 301 (2012).

[53] X. Z. Yu, N. Kanazawa, W. Z. Zhang, T. Nagai, T. Hara, K. Kimoto, Y. Matsui, Y. Onose, and Y. Tokura, Nat. Comm. **3,** 988 (2012).

[54] A. Yamaguchi, T. Ono, S. Nasu, K. Miyake, K. Mibu, T. Shinjo, Phys. Rev. Lett. **92**, 077205 (2004).

[55] M. Hayashi, L. Thomas, R. Moriya, C. Rettner, S. S. P. Parkin, Science **320**, 209 (2008).

[56] A. A. Thiele, Phys. Rev. Lett. **30**, 230 (1972).

[57] K. Everschor, M. Garst, R. A. Duine, and A. Rosch, Phys. Rev. B **84**, 064401 (2011).

[58] J. Iwasaki, M. Mochizuki, adn N. Nagaosa, Nat. Commun. **4**, 1463 (2013).

[59] J. Iwasaki, M. Mochizuki, and N. Nagaosa, Nature Nanotech. **8**, 742 (2013).

[60] W. Jiang, X. Zhang, G. Yu, W. Zhang, X. Wang, M. B. Jungeisch, J. E. Pearson, X. Cheng, O. Heinonen, K. L. Wang, Y. Zhou, A. Hoffmann, and S. G. E. te Velthuis, Nat. Phys. **13**, 162 (2017).

[61] Y. Ishikawa, K. Tajima, D. Bloch, M. Roth, Solid State Commun. **19**, 525 (1976).

[62] I. A. Campbell, A. Fert, and O. Jaoul, J. Phys. C **1**, S95 (1970).

[63] T. McGuire and R. Potter, IEEE Trans. Magn. **11**, 1018 (1975).

[64] D. A. Thompson, L. T. Romankiw, and A. F. Mayadas, IEEE Trans. Magn. **11**, 1039 (1975).

[65] H. X. Tang, R. K. Kawakami, D. D. Awschalom, and M. L. Roukes, Phys Rev. Lett. **90**, 107201 (2003).

[66] M. Bowen, K.-J. Friedland, J. Herfort, H.-P. Schnherr, and K. H. Ploog, Phys. Rev. **71**, 172401 (2005).

[67] Xuesong Jin, Rafael Ramos, Y. Zhou, C. McEvoy, and I. V. Shvets, J. Appl. Phys. **99**, 08C509 (2006).

[68] K. M. Seemann, F. Freimuth, H. Zhang, S. Blügel, Y. Mokrousov, E. Bürgler, and C. M. Schneider, Phys Rev. Lett. **107**, 086603 (2011).

[69] K. Kadowaki, K. Okuda, and M. Date, J. Phys. Soc. Jap. **51**, 2433 (1982).

[70] S. V. Demishev, V. V. Glushkov, I. I. Lobanova, M. A. Anisimov, V. Yu. Ivanov, T. V. Ishchenko, M. S. Karasev, N. A. Samarin, N. E. Sluchanko, V. M. Zimin, and A. V. Semeno, Phys. Rev. B **85**, 045131 (2012).

[71] S. X. Huang and C. L. Chien, Phys. Rev. Lett. **108**, 267201 (2012).

[72] T. Moriya and K. Ueda, Adv. Phys. **49**, 555, (2000).

[73] Hilbert v. Löhneysen, Achim Rosch, Matthias Vojta, Peter Wölfle, Rev. Mod. Phys. **79**, 1015 (2007).

[74] Y. Taguchi, Y. Oohara, H. Yoshizawa, N. Nagaosa, Y. Tokura, Science **291**, 2573 (2001).

[75] G. L. J. A. Rikken, J. Fölling, P. Wyder, Phys Rev. Lett. **87**, 236602 (2001).

[76] Flavia Pop, Pascale Auban-Senzier, Enric Canadell, Geert L.J.A. Rikken, and N. Avarvari, Nat. Commun.**5**, 3757 (2014).

[77] C. O. Avci, K. Garello, A. Ghosh, M. Gabureac, S. F. Alvarado and P. Gambardella, Nat. Phys. **11**, 570 (2015).

[78] K.J. Kim, T. Moriyama, T. Koyama, D. Chiba, S.W. Lee, S.J. Lee, K.J. Lee, H.W. Lee, and T. Ono, arXiv:1603.08746 (2016).

[79] K. Yasuda, A. Tsukazaki, R. Yoshimi, K.S. Takahashi, M. Kawasaki, and Y. Tokura, Phys. Rev. Lett. **117**, 127202 (2016).

[80] T. Ideue, K. Hamamoto, S. Koshikawa, M. Ezawa, S. Shimizu, Y. Kaneko, Y. Tokura, N. Nagaosa, and Y. Iwasa, Nat. Phys. **13**, 578 (2017).

[81] H. Kawamura, J. Phys.: Condens. Matter 10, 4707 (1998).

[82] A. Vansteenkiste, J. Leliaert, M. Dvornik, M. Helsen, F. Garcia-Sanchez, and B. Van Waeyenberge, AIP Adv. **4**,107133 (2014).

[83] N. D. Mermin, Rev. Mod. Phys. **51**, 591 (1979).

[84] G. Blatter, M. Y. Feigel'man, Y. B. Geshkenbein, A. I. Larkin, V. M. Vinokur, Rev. Mod. Phys. **66**, 1125 (1994).

[85] Meng-Bo Luo, Xiao Hu, Phys. Rev. Lett. **98**, 267002 (2007).

[86] N. Kanazawa, S. Seki, and Y.Tokura, Adv. Mater. **29**, 1603227 (2017).

[87] S.-Z. Lin, A. Saxena, Phys. Rev. B **93**, 060401(R) (2016).

[88] K. Garello, I. M. Miron, C. O. Avci, F. Freimuth, Y. Mokrousov, S. Blügel, S. Auffret, O. Boulle, G. Gaudin, P. Gambardella, Nature Nanotech. **8**, 587 (2013).

[89] R. M. Fleming, and C. C. Grimes, Phys. Rev. Lett. **42**, 1423 (1979).

[90] G. Grüner, Rev. Mod. Phys. **60**, 1129 (1988).

[91] U. Yaron, P. L. Gammel, D. A. Huse, R. N. Klemiman, C. S. Oglesby, E. Bucher, B. Batlogg, D. J. Bishop, K. Mortensen, and K. N. Clausen, Nature **376**, 753 (1995).

[92] C. J. Olson, C. Reichhardt, and F. Nori, Phys. Rev. Lett. **81**, 3757 (1998).

[93] C. Reichhardt, D. Ray, and C. J. Olson Reichhardt, Phys. Rev. Lett. **114**, 217202 (2015).

[94] K. Yasuda, A. Tsukazaki, R. Yoshimi, K. Kondou, K. S. Takahashi, Y. Otani, M. Kawasaki, and Y. Tokura, Phys. Rev. Lett. **119**, 137204 (2017).

[95] W. Kleemann, J. Rhensius, O. Petracic, J. Ferre, J. P. Jamet, and H. Bernas, Phys. Rev. Lett. **99**, 097203 (2007).

[96] G. Tatara and H. Fukuyama, J. Phys. Soc. Jpn. **83**, 104711 (2014).

[97] P. Bak, and H. Jensen, J. Phys. C **13,** L881 (1980).

[98] A. Tonomura, X. Z. Yu, K. Yanagisawa, T. Matsuda, Y. Onose, N. Kanazawa, H. S. Park, and Y. Tokura, Nano Lett. **12**, 1673 (2012).

[99] E. Moskvin, S. Grigoriev, V. Dyadkin, H. Eckerlebe, M. Baenitz, M. Schmidt, and H. Wilhelm, Phys. Rev. Lett. **110**, 077207 (2013).

[100] M. N. Wilson, E. A. Karhu, A. S. Quigley, U. K. Rößler, A. B. Butenko, A. N. Bogdanov, M. D. Robertson, and T. L. Monchesky, Phys. Rev. B **86**, 144420 (2012).

[101] M. N. Wilson, E. A. Karhu, D. P. Lake, A. S. Quigley, S. Meynell, A. N. Bogdanov, H. Fritzsche, U. K. Rößler , and T. L. Monchesky, Phys Rev. B. **88**, 214420 (2013).

[102] Yufan Li, N. Kanazawa, X. Z. Yu, A. Tsukazaki, M. Kawasaki, M. Ichikawa, X. F. Jin, F. Kagawa and Y. Tokura, Phys. Rev. Lett. **110**, 117202 (2013).

[103] E. Karhu, S. Kahwaji, T. L. Monchesky, C. Parsons, M. D. Robertson, and C. Maunders, Phys Rev. B **82**, 184417 (2010).

[104] A. Bauer, A. Neubauer, C. Franz, W. Münzer, M. Garst, and C. Pfleiderer, Phys. Rev. B **82**, 064404 (2010).

[105] J. M. Ziman, *Principle of the Theory of Solids* (Cambridge University Press, Cambridge, England, 1964).

[106] Minhyea Lee, Y. Onose, Y. Tokura, and N. P. Ong, Phys. Rev. B **75**, 172403 (2007).

[107] S. V. Grigoriev, V. A. Dyadkin, E. V. Moskvin, D. Lamago, Th. Wolf, H. Eckerlebe, and S. V. Maleyev, Phys. Rev. B **79**, 144417 (2009).

Publication list

1. T. Yokouchi, N. Kanazawa, A. Tsukazaki, Y. Kozuka, M. Kawasaki, M. Ichikawa, F. Kagawa, and Y. Tokura, "Stability of two-dimensional skyrmion in thin films of $Mn_{1-x}Fe_xSi$ investigated by the topological Hall effect" Physics Review B **89**, 064416 (2014).

2. T. Yokouchi, N. kanazawa, A. Tsukazaki, Y. Kozuka, A. Kikkawa, Y. Taguchi, M. Kawasaki, M. Ichikawa, F. Kagawa, Y. Tokura, "Formation of In-plane Skyrmions in Epitaxial MnSi Thin Films as Revealed by Planar Hall Effect" Journal of the Physical Society of Japan **84**, 104708 (2015).

3. T. Yokouchi, N. Kanazawa, A. Kikkawa, D. Morikawa, K. Shibata, T. Arima, Y. Taguchi, F. Kagawa, Y. Tokura, "Electrical magnetochiral effect induced by chiral spin fluctuations" Nature Communication **8**, 866 (2017).

Acknowledgement